



Deposited via The University of Leeds.

White Rose Research Online URL for this paper:

<https://eprints.whiterose.ac.uk/id/eprint/116175/>

Version: Accepted Version

Article:

Kahl, M, Viccaro, M, Ubide, T et al. (2017) A branched magma feeder system during the 1669 eruption of Mt. Etna: evidence from a time-integrated study of zoned olivine phenocryst populations. *Journal of Petrology*, 58 (3). pp. 443-472. ISSN: 0022-3530

<https://doi.org/10.1093/petrology/egx022>

(c) 2017, The Author. Published by Oxford University Press. All rights reserved. For Permissions, please e-mail: journals.permissions@oup.com. This is a pre-copyedited, author-produced PDF of an article accepted for publication in the *Journal of Petrology* following peer review. The version of record, 'Kahl, M, Viccaro, M, Ubide, T et al (2017) A branched magma feeder system during the 1669 eruption of Mt. Etna: evidence from a time-integrated study of zoned olivine phenocryst populations. *Journal of Petrology*, 58 (3). pp. 443-472,' is available online at: <https://doi.org/10.1093/petrology/egx022>

Reuse

Items deposited in White Rose Research Online are protected by copyright, with all rights reserved unless indicated otherwise. They may be downloaded and/or printed for private study, or other acts as permitted by national copyright laws. The publisher or other rights holders may allow further reproduction and re-use of the full text version. This is indicated by the licence information on the White Rose Research Online record for the item.

Takedown

If you consider content in White Rose Research Online to be in breach of UK law, please notify us by emailing eprints@whiterose.ac.uk including the URL of the record and the reason for the withdrawal request.

1
2
3
4 1 **A branched magma feeder system during the 1669 eruption of Mt.**
5
6
7 2 **Etna: evidence from a time-integrated study of zoned olivine**
8
9
10 3 **phenocryst populations**
11
12
13

14 4 Maren Kahl^{1, 2, 3*}, Marco Viccaro^{4, 5}, Teresa Ubide^{6, 7}, Daniel J. Morgan³, & Donald B. Dingwell²
15

16 5 ¹ Institute of Earth Sciences, University of Iceland, Sturlugata 7, IS-101 Reykjavík, Iceland
17

18 6 ² Department of Earth & Environmental Sciences, LMU Munich, Theresienstrasse 41, 80333 München, Germany
19

20 7 ³ School of Earth & Environment, University of Leeds, LS2 9JT Leeds, United Kingdom
21

22 8 ⁴ Università di Catania, Dipartimento di Scienze Biologiche Geologiche e Ambientali - Sezione di Scienze della
23
24 9 Terra, Corso Italia 57, I-95129, Catania, Italy

25
26 10 ⁵ Istituto Nazionale di Geofisica e Vulcanologia, Osservatorio Etneo, Piazza Roma 2, I-95125 Catania, Italy
27

28 11 ⁶ Department of Geology, Trinity College Dublin, Dublin 2, Ireland
29

30 12 ⁷ School of Earth and Environmental Sciences, The University of Queensland, Brisbane, QLD 4072, Australia
31

32
33 14 *Corresponding author. Present address: Institute of Earth Sciences, University of Iceland, Sturlugata 7, IS-101
34
35 15 Reykjavík, Iceland. Telephone: +354 525 4481. E-mail: marenk@hi.is
36
37

38
39 16 **ABSTRACT**
40

41 17 The 1669 eruption of Mt Etna was one of the most voluminous and devastating of its flank
42
43 18 eruptions in historical times. Despite a large body of relevant research, knowledge of the timing
44
45 19 and duration of magma transfer and magma recharge through the internal plumbing system
46
47 20 preceding and during the eruption is still limited. To address that lack of knowledge, we apply a
48
49 21 three-way integrated method, linking Systems Analysis of crystals, a time-integrated study of
50
51 22 zoned olivine populations, and a forward-modelling approach using thermodynamic calculations.
52
53 23 Analysis of 202 olivine crystals erupted during the initial (pre-March 20, i.e. *SET1*) and the final
54
55 24 (post-March 20; i.e. *SET2* and *MtRs*) stages of the eruption reveals the existence of three different
56
57
58
59
60

1
2
3 25 Magmatic Environments (MEs) in which the majority of the olivine cores [M_1 ($=Fo_{75-78}$)] and
4
5 26 rims [i.e. M_5 ($=Fo_{51-59}$) and M_3 ($=Fo_{65-69}$)] formed.

7
8
9 27 Application of the *rhyolite-MELTS* software enabled us to constrain the key intensive variables
10
11 28 associated with these MEs. We find that temperature, water content and oxidation state vary
12
13 29 between these MEs. Application of diffusion modelling to the zoned olivine crystals enabled us
14
15 30 to reconstruct the timing and chronology of melt and crystal transfer prior to and during the 1669
16
17 31 flank eruption. We find, that following the formation of the olivine cores [M_1 ($=Fo_{75-78}$)], the
18
19 32 reservoir M_1 was intruded by batches of more evolved, degassed and possibly aphyric M_5 -type
20
21 33 magma, commencing 1.5 years prior to eruptive activity. This is the origin of the *SET1* olivine
22
23 34 rims (i.e. Fo_{51-59}). In the months prior to eruption, timescale data show that recharge activity
24
25 35 along the newly established pathway M_1 - M_5 increased notably. Starting in November 1668, only
26
27 36 a few weeks after the first intrusive episode into the M_1 reservoir, a second pulse of magma
28
29 37 injections (M_3 -type magma) occurred and a new pathway M_1 - M_3 opened; this is how the *SET2*
30
31 38 olivine rims (i.e. Fo_{65-69}) formed. For several weeks a bifurcated transport system with two
32
33 39 dominant magma pathways developed along M_1 - M_5 and M_1 - M_3 dyke injections. Accompanied
34
35 40 by vigorous seismicity, in the immediate days prior to eruption the local magma transfer
36
37 41 dynamics changed and the M_1 - M_5 recharge activity slowed down, as shown by a relative lack of
38
39 42 crystals recording shorter timescales. M_1 - M_3 recharge, however, remained high and persisted
40
41 43 following the eruption onset on March 11, during which the *SET1* lavas were drained. We
42
43 44 propose that the change of the local magma transfer dynamics might be linked to changes in the
44
45 45 local stress field brought on during eruption. This may potentially have been due to repeated dyke
46
47 46 injections into Etna's shallow plumbing system disrupting the early M_1 - M_5 pathway and at the
48
49 47 same time stabilizing the M_1 - M_3 route as a dominant feeder. This transfer of system feeding
50
51
52
53
54
55
56
57
58
59
60

1
2
3 48 would reproduce the observed syn-eruptive recharge and mixing in the weeks following eruption
4
5 49 onset, culminating in the eruption of the later *SET2* lavas.
6
7

8
9 **KEYWORDS:**

10
11 Olivine zoning; Plumbing system; Mt. Etna; Timescales; Magma mixing
12
13

14 **INTRODUCTION**

15
16
17
18 **Geological setting**

19
20
21 54 Mount Etna is a 3340-m-high (asl), composite stratovolcano located on the eastern coast of Sicily
22
23 55 (Fig. 1) and covering a basal area of ~ 1250 km². It is located at the intersection of three tectonic
24
25 56 domains, bounded by the transform Malta escarpment to the east, the Hyblean Plateau to the
26
27 57 south and the subduction-related Aeolian arc to the north. To the west, subduction is blocked by
28
29 58 compressive continental collision between the European and the African plate. Numerous
30
31 59 models, including the southward migration of the Ionian slab (e.g. Schiano *et al.*, 2001) and the
32
33 60 opening of a slab window (Gvirtzman & Nur, 1999; Doglioni *et al.*, 2001) have been proposed to
34
35 61 explain the anomalous location of the volcano close to the suture zone of the African and
36
37 62 European plates and its high magmatic flux. Geologically, the volcano rests on the southern edge
38
39 63 of the over-thrust units of the Apennine-Maghrebian chain to the south (Fig. 1), and the
40
41 64 undeformed remnants of the African margin to the southeast (e.g. Branca *et al.*, 2011). Volcanism
42
43 65 is constrained to have started in the Etna region about ~ 500 ka ago (Gillot *et al.*, 1994; Branca *et*
44
45 66 *al.*, 2011).
46
47
48
49
50
51

52
53 **Types of eruptions at Mt. Etna: summit vs. flank activity**

54
55
56 68 Like other basaltic stratovolcanoes, Etna is characterized by summit and flank eruptions. Summit
57
58 69 eruptions are usually constrained to one of six central craters (Voragine, Bocca Nuova 1, Bocca
59
60

1
2
3 70 Nuova 2, Northeast Crater, Southeast Crater and New Southeast Crater) and the sub-terminal area
4
5 71 (e.g. Corsaro *et al.*, 2009; Allard *et al.*, 2006; Branca and Del Carlo, 2004). Flank eruptions
6
7 72 usually affect the intermediate and lower flanks of the volcano and can produce lava flow fields
8
9 73 of considerable extent (e.g. the 1991-93 flank eruption produced a compound lava flow field of
10
11 74 $240 \pm 29 \times 10^6 \text{ m}^3$, Calvari *et al.*, 1994; Stevens *et al.*, 1997). Two different types of flank eruptions
12
13 75 have been defined: 1. Central-lateral (Rittmann, 1965) or Central Conduit-Fed (CCF; Corsaro *et*
14
15 76 *al.*, 2009) and 2. Eccentric (Rittmann, 1965), peripheral (Acocella and Neri, 2003) or Deep Dyke-
16
17 77 Fed (DDF; Corsaro *et al.*, 2009) eruptions. Central-lateral flank eruptions originate by fracturing
18
19 78 and lateral draining of the central conduits with the formation of eruptive vents at high altitudes.
20
21 79 The eruption products resemble closely those erupted from the summit craters in being highly
22
23 80 porphyritic (~30-40 % crystals) and plagioclase-rich due to significant water degassing in the
24
25 81 central conduit system (e.g. Métrich *et al.*, 2004). Eccentric or deep dyke-fed (DDF) flank
26
27 82 eruptions occur rarely [1763 (Corsaro *et al.*, 2009), 1974 (Corsaro *et al.*, 2009), 2001 (Lanzafame
28
29 83 *et al.*, 2003; Behncke and Neri, 2003; Métrich *et al.*, 2004; Corsaro *et al.*, 2007; Ferlito *et al.*,
30
31 84 2012) and 2002-03 (Andronico *et al.*, 2005; Spilliaert *et al.*, 2006)]. Eccentric eruptions are
32
33 85 highly explosive with high tephra/lava ratios (e.g. Andronico *et al.*, 2005), and have low to
34
35 86 medium phenocryst contents (<20% Andronico *et al.*, 2005), with dominantly mafic mineral
36
37 87 phases (Armienti *et al.*, 1988; Corsaro *et al.*, 2009; Ferlito *et al.*, 2012). As these eruption
38
39 88 products differ from those of summit and central conduit-fed (CCF) flank eruptions, previous
40
41 89 studies concluded that eccentric eruptions must have been driven by rapid ascent of deeply rooted
42
43 90 intrusions - below the volcanic pile - that bypassed the shallow, central conduit system and
44
45 91 therefore are undegassed (e.g. Corsaro *et al.*, 2009; Ferlito *et al.*, 2012). Hence, this type of flank
46
47 92 eruptions is also referred to as Deep Dyke-Fed (DDF; Corsaro *et al.*, 2009), as opposed to the
48
49 93 more common central-lateral or Central Conduit-Fed (CCF; Corsaro *et al.*, 2009) flank eruptions.
50
51
52
53
54
55
56
57
58
59
60

94 **The 1669 eruption: Characteristics and historical context**

95 In this paper, we focus on the 1669 eruption, which is a central-lateral or Central Conduit-Fed
96 flank eruption. The 1669 eruption was ranked as one of the most destructive and voluminous
97 ($607\pm 105\times 10^6\text{m}^3$, Branca *et al.*, 2013) flank eruptions of Mt. Etna in historical times (e.g.
98 Corsaro *et al.*, 1996; Branca *et al.*, 2013). Between 1607 and 1669, 8 flank eruptions occurred on
99 different sectors of the volcano; a brief summary of the duration, location of eruption vents and
100 erupted volume is provided in Table 1. Preceded by a period of summit eruptions between 1654-
101 1656 (<http://www.ct.ingv.it/en/11-notizie/news/561-etna-eruptions-pre1900.html>) and more than
102 two weeks of increasing seismic activity (e.g. Corsaro *et al.*, 1996 and references therein), the
103 1669 eruption commenced in the early morning of March 11 through a system of NNW-SSE
104 trending eruptive fissures that opened between 950 and 700 m a.s.l. (indicated as 1 in Fig. 1;
105 Branca *et al.*, 2013). This first segment of the eruptive fracture system was characterized by weak
106 and short-lived explosive activity. A second segment (2) opened shortly afterwards between 850
107 and 825 m a.s.l. and built a spatter rampart (Fig. 1). That same day (March 11) a third segment
108 (3) opened between 850 and 775 m a.s.l. This became the main vent - Mt. Rossi - of the eruption
109 (Fig. 1) and initially produced extended, explosive activity with ash fall followed by lava
110 emission. The fourth segment (4) formed between 750 and 700 m a.s.l. close to the cone of Mt.
111 Mompilieri (Fig. 1; Branca *et al.*, 2013); it was characterized by mild explosive activity and a
112 minor lava flow. On March 12 a fifth segment (5) formed at the eastern base of Mt. Mompilieri
113 between 700 and 640 m a.s.l. (Branca *et al.*, 2013). The eruptive activity continued for 122 days
114 and destroyed several towns and settlements along the S-flank of Etna volcano until it ceased on
115 July 11, 1669. Activity at the summit craters remained quiet during the flank eruption until March
116 25, when a violent explosive event occurred followed by the partial collapse of the summit cone
117 (Corsaro *et al.*, 1996; Nicotra and Viccaro, 2012). A detailed report of the sequence of events and

1
2
3 118 the evolution of the lava flow field during the 4 months of eruptive activity can be found in
4
5 119 *Branca et al.* (2013).
6
7

8
9 120 In comparison to some of the historic and recent flank eruptions (e.g. 1991-1993), the 1669
10
11 121 eruption was relatively short-lived, with only four months of eruptive activity. During this brief
12
13 122 interval of persistent eruptive activity, a compound lava flow field covered a total area of ~ 40
14
15 123 $\times 10^6$ m², with a total length of 17 km (*Branca et al.*, 2013). The relatively low altitude (800-850
16
17 124 m a.s.l.) of the erupting vents and high effusion rates (58 ± 10 m³/s, *Branca et al.*, 2013) enabled
18
19 125 the lava flows to run over long distances. As a result, settlements located on the lower southern
20
21 126 flank of the volcano, including the western districts of Catania were destroyed (e.g. *Branca et al.*,
22
23 127 2013). The 1669 flank eruption marks a major transition in terms of eruption intensity and
24
25 128 petrography amongst the historic lavas (*Corsaro et al.*, 1996; *Condomines et al.*, 1995; *Hughes et*
26
27 129 *al.*, 1990; *Clocchiatti et al.*, 1988; *Guest and Duncan*, 1981; *Tanguy*, 1980). Pre-1669 eruptions
28
29 130 (1600-1669) were long-lasting, porphyritic and plagioclase-rich with high mean effusion rates
30
31 131 (1.19 m³/s; e.g. *Hughes et al.*, 1990; *Branca et al.*, 2013; *Nicotra and Viccaro*, 2012). In contrast,
32
33 132 the post-1669 eruptions (1670-1755) were more sporadic and short-lived and had low output rates
34
35 133 (0.02 m³/s; *Branca et al.*, 2013). Post-1669 eruption products also contain predominantly mafic
36
37 134 phase assemblages (*Corsaro et al.*, 1996).
38
39
40
41
42
43
44

45 135 It is possible that the steady increase in effusion rates during the first half of the 17th century
46
47 136 culminated in the devastating March-July 1669 flank eruption. It has been argued that lateral
48
49 137 draining of the central conduit system during the eruption caused not only the partial collapse of
50
51 138 the summit cone (e.g. *Corsaro et al.*, 1996) but also had long lasting consequences for the
52
53 139 evolution of Etna's shallow plumbing system (e.g. *Condomines et al.*, 1995). The impact of
54
55 140 Etna's modified shallow plumbing configuration could be observed in the century following the
56
57
58
59
60

1
2
3 141 1669 eruption, with the 1670-1755 period displaying significantly lowered output rates (0.02
4
5 142 m³/s; Branca *et al.*, 2013) and sparse flank activity (only 3 flank eruptions). It was only
6
7
8 143 afterwards, in the period 1755 to 1970, that the mean effusion rate increased steadily up to 0.51
9
10 144 m³/s (e.g. Branca *et al.*, 2013 and references therein).

11
12
13 145 Detailed geochemical and petrological studies of products of the 1669 eruption (Corsaro *et al.*,
14
15 146 1996) revealed that the erupted lavas are porphyritic hawaiites containing variable amounts of
16
17
18 147 phenocrysts (porphyritic index; PI = 37-52 vol% phenocrysts) and mafic mineral phases (mafic
19
20 148 mineral phenocrysts/total phenocrysts; CI_{phx} = 10-53 vol%). Corsaro *et al.* (1996) found that the
21
22 149 lavas erupted during the initial stages of the 1669 eruption (i.e. between March 11 and 20) differ
23
24 150 considerably in their petrography (i.e. average PI=33 and CI_{phx}=36 vol%) from lavas erupted
25
26 151 after March 20 (average PI=44 and CI_{phx}=18 vol%). Petrographic differences are also reflected in
27
28 152 the major and trace element bulk geochemistry (Barbieri *et al.*, 1993; Corsaro *et al.*, 1996).
29
30 153 Consequently, Corsaro *et al.* (1996) classified the 1669 lavas into two groups: *SET1* and *SET2*.

31
32
33
34
35 154 *SET1* products were emplaced during the initial phase of the eruption, from March 11 to March
36
37 155 20, 1669. These samples have been described as being more 'basic' and 'magnesian', with
38
39 156 similarities to later 18th and 20th century eruption products. *SET1* bulk rock compositions from
40
41 157 Corsaro *et al.* (1996) are characterized by higher MgO (mean 6.65 ± 0.38 wt%) contents and
42
43 158 higher compatible (i.e. Cr, Ni, Co, Sc) and incompatible (e.g. Th, La) trace element
44
45 159 concentrations than the later erupted *SET2* lavas (Corsaro *et al.*, 1996). The *SET2* samples were
46
47 160 emplaced after March 20, 1669 and are described by Corsaro *et al.* (1996) as plagioclase-phyric
48
49 161 and more evolved in composition (e.g. mean MgO 5.07 ± 0.19 wt%) than the *SET1* eruption
50
51 162 products. *SET2* lavas strongly resemble the plagioclase-phyric rocks of the early 17th century
52
53 163 (Corsaro *et al.*, 1996).
54
55
56
57
58
59
60

1
2
3 164 Both sets of eruption products (*SET1* and *SET2*) were interpreted by Corsaro *et al.* (1996) as the
4
5 165 result of fractional crystallization of two, compositionally-distinct primary magmas under distinct
6
7
8 166 storage conditions, which fractionated different volumetric proportions of phenocrysts.
9
10 167 Segregation was explained by the authors utilizing a ‘laminar plume model’, where mafic, gas-
11
12 168 rich and therefore buoyant *SET1* magma rises through a pre-existing reservoir filled with *SET2*
13
14 169 melt, without significantly (physically or chemically) interacting with it; this enables uprising
15
16 170 *SET1* magma to retain its chemical and petrological signature, as mixing with *SET2* melt is
17
18 171 inhibited.
19
20
21
22

23 172 The possibility of fresh magma inputs being able to bypass resident, more viscous magma is not
24
25 173 new; such a model was invoked by Landi *et al.* (2006) to explain the segregation of volatile-poor
26
27 174 degassed magmas and volatile-rich ‘golden pumices’ during the April 5, 2003 paroxysm of
28
29 175 Stromboli volcano. In this case, bubble-driven ascent of deep volatile-rich magma through
30
31 176 shallower resident magma enabled rapid ascent to the vent, with subsequent mixing only after the
32
33 177 paroxysm. Despite a possibly shared characteristic of magma injections not mixing in the first
34
35 178 instance, the Stromboli and Etna systems are quite different. A worrying implication of bypass
36
37 179 behaviour is that intrusion and eruption can occur nearly simultaneously, and do not require a
38
39 180 significant residence time of mafic magma in an evolved reservoir. This has considerable
40
41 181 implications for the assessment of hazards posed by future 1669-type events, as it implies that
42
43 182 similar, voluminous, low-elevation eruptions could commence with little warning. In fact,
44
45 183 contemporary records indicate that signals of volcanic unrest in the form of vigorous seismic
46
47 184 events, with epicenters located close to the town of Nicolosi on the southern flank of the volcano,
48
49 185 preceded the 1669 eruption by approximately two weeks (e.g. Mulas *et al.*, 2016 and references
50
51 186 therein); seismic activity increased on March 08, 1669, culminating in the eruption onset on
52
53 187 March 11, 1669 (Mulas *et al.*, 2016 and references therein; Tanguy and Patané, 1996). The
54
55
56
57
58
59
60

1
2
3 188 purpose of this paper is to obtain new insights into the plumbing system feeding the 1669 flank
4
5 189 eruption and test viability (and hence hazard implications) of quick melt bypass.
6
7

8
9 190 **Etna's modern (1991-2008) plumbing system: Insights from a crystal chemistry**
10
11 **perspective**
12

13
14 192 In previous studies, Kahl *et al.* (2011, 2013 & 2015) developed a novel petrological methodology
15
16 193 linking a *Systems Analysis* approach to compositionally-zoned olivine populations with a time-
17
18 194 integrated study (i.e. diffusion modelling in olivine). This approach was successfully applied to
19
20 195 samples from recent summit and flank (i.e. 1991-2008) eruptions at Etna volcano to reconstruct
21
22 196 the residence and migration history of magma through Etna's modern plumbing system (Kahl *et*
23
24 197 *al.*, 2015). The present study uses and builds upon existing techniques and results developed by
25
26 198 Kahl *et al.* (2011, 2013 & 2015). Therefore, in this section, we review some of the main methods
27
28 199 and concepts and briefly summarize what we know so far about Etna's modern plumbing system
29
30
31
32
33 200 from a combined crystal chemistry and kinetic modelling approach.
34
35

36
37 201 Studying the compositional and zoning record of 180 olivine crystals that were erupted between
38
39 202 1991 and 2008 at Mt. Etna, Kahl *et al.* (2011, 2013 and 2015) recognized that zoning profiles of
40
41 203 Fe-Mg and selected trace elements (e.g. Ni, Mn, Ca) in olivine contain core and/or rim
42
43 204 compositional plateaux with diffuse boundaries separating them. The occurrence of such
44
45 205 compositional plateaux was interpreted as sequential growth of olivine under a constant set of
46
47 206 intensive thermodynamic variables (pressure, temperature, composition, fugacities of volatile
48
49 207 species) defining a certain Magmatic Environment (ME). This is opposed to progressive changes,
50
51 208 such as cooling or differentiation that would result in continuous variations of composition rather
52
53 209 than plateaux separated by sudden jumps or diffuse boundaries (Kahl *et al.*, 2015). A Magmatic
54
55 210 Environment (ME) may represent a physically distinct entity (e.g. a sill, dyke), or a virtual entity
56
57
58
59
60

1
2
3 211 (e.g. a set of P, T, X, fO₂, fH₂O conditions within a zoned larger magma reservoir). Kahl *et al.*
4
5 212 (2011, 2013 and 2015) used the terms “magmatic reservoir” and “magmatic environment” to
6
7 213 distinguish the physical entity from the virtual entity defined by a set of intensive variables; the
8
9 214 two may be the same (e.g. in an unzoned magma reservoir of small enough size) but do not have
10
11 215 to be. Kahl *et al.* (2011) assumed that the compositional variation from core to rim in a crystal
12
13 216 represents a chemical stratigraphy and that the compositional record can be used to identify and
14
15 217 effectively track different MEs crystals passed through on the way to eruption. Consequently, the
16
17 218 change in zoning pattern from one plateau to another is equivalent to the transfer of the crystal
18
19 219 from one ME to another. This can be accomplished either by the crystal physically moving (with
20
21 220 some melt) from one environment to another, or by the environment itself changing around the
22
23 221 crystal (e.g. by cooling or degassing). To be able to track effectively the sequence of magmatic
24
25 222 events preserved in the chemical stratigraphy of populations of zoned olivine crystals, Kahl *et al.*
26
27 223 (2011) developed the tool of *Systems Analysis*. This allows to decipher the record of different
28
29 224 pathways (sequences of changes in MEs) stored in the crystal cargo of a given rock by using
30
31 225 connectivity diagrams to organize the compositional information. The frequency of connections
32
33 226 found in the connectivity diagrams (diagrams where successive compositional plateaux are
34
35 227 connected by directed line segments; the direction pointing from core toward rim) are taken to
36
37 228 provide a measure of the relative frequency with which pathways between different environments
38
39 229 were used. For example, Kahl *et al.* (2011) discovered that a single thin section of a lava flow
40
41 230 from the 1991-93 SE flank eruption of Etna, contained olivine phenocrysts with three different
42
43 231 types of zoning patterns (normal, reverse and complex) and compositions ranging from Fo₈₃ to
44
45 232 Fo₇₀. Compositional plateaux in the olivine crystals were consistent with four MEs that, when
46
47 233 considered with the relevant diffusive modifications, could be used to describe the total diversity
48
49 234 of compositional variation in the olivine phenocrysts that were erupted between December 1991
50
51
52
53
54
55
56
57
58
59
60

1
2
3 235 and March 1992 (Kahl *et al.*, 2011). The width of the diffusion zone between two compositional
4
5 236 plateaux and the shape of the concentration profiles record the duration and residence time a
6
7
8 237 crystal spent within a given ME. Hence, Kahl *et al.* (2011) developed the tool of *sequential*
9
10 238 *kinetic modelling* that allows working backward - from the rim to the core - the durations a
11
12 239 crystal spent in different MEs prior to eruption. Finally, Kahl *et al.* (2015) developed a forward
13
14 240 modelling approach using thermodynamic calculations with the MELTS software (Ghiorso and
15
16 241 Sack, 1995; Asimow and Ghiorso, 1998) to identify the key intensive variables associated with
17
18 242 the different Magmatic Environments identified. In this approach the observed populations of
19
20 243 mineral compositions (e.g. Fo₇₉₋₈₃) defining a certain ME (e.g. M₀), rather than single
21
22 244 compositions, are associated with thermodynamic parameters (P, T, water content, oxygen
23
24 245 fugacity and bulk composition of melt) to identify the most plausible set corresponding to each
25
26 246 ME.

27
28
29
30
31
32 247 Application of this combined and novel methodology that links the crystal chemistry with a time-
33
34 248 integrated study and forward thermodynamic modelling enabled Kahl *et al.* (2011, 2013 and
35
36 249 2015) to investigate the temporal evolution of Etna's modern plumbing system across multiple
37
38 250 eruptive episodes of different styles, and at different locations. Considering the comprehensive
39
40 251 compositional and zoning record preserved in 180 olivine crystals that erupted between 1991 and
41
42 252 2008, five MEs were identified: M₀ (Fo₇₉₋₈₃), M₁ (Fo₇₅₋₇₈), M₂ (Fo₇₀₋₇₂), M₃ (Fo₆₅₋₆₉) and mm₁
43
44 253 (Fo₇₃₋₇₅). Kahl *et al.* (2015) found that the same MEs as those deduced by Kahl *et al.* (2011,
45
46 254 2013) to describe the observed variability of olivine compositions erupted during the 1991-93
47
48 255 flank and the 2006 summit eruptions, could be used to describe the compositional variations
49
50 256 recorded in all 1991-2008 olivine crystals. The combined Systems Analysis record of all eruption
51
52 257 products revealed that although the MEs remained the same during 17 years, the interconnectivity
53
54
55
56
57
58
59
60

1
2
3 258 between them and hence the dominant magma pathways changed with time. Main changes were
4
5 259 found either between large eruptions (1991-93 and 2001) or between eruptive episodes.
6
7

8
9 260 For example, Kahl *et al.* (2013) studied the compositional and zoning record of olivines that were
10
11 261 erupted during two different events (July 20 and October 28) of the 2006 summit eruptions at Mt.
12
13 262 Etna. The authors discovered that olivines of the July 20 and the October 28, 2006 eruptions were
14
15 263 not only characterized by different zoning patterns but also by different core and rim plateau
16
17 264 compositions. The July 20 olivines were reversely zoned with low forsterite core (=F₀₇₀₋₇₂)
18
19 265 plateaux and higher forsterite rims (=F₀₇₃₋₇₅). 3 months later, during the October 28 event,
20
21 266 olivines showed dominantly normal zoning with high forsterite core plateaux (=F₀₇₉₋₈₂) and
22
23 267 decreasing forsterite contents at the rims (=F₀₇₀₋₇₂). Based on the different core and rim plateau
24
25 268 compositions and the different zoning types (normal vs. reverse) three different MEs [M₀ (=F₀₇₉₋
26
27 269 82), M₂ (=F₀₇₀₋₇₂) and mm₁ (=F₀₇₃₋₇₅)] with diverging connectivity patterns were observed.
28
29 270 Olivines erupted in July showed a dominant population of crystals connecting the environments
30
31 271 M₂-mm₁, whereas olivines erupted in October tracked a different history between M₀-M₂. Kahl *et*
32
33 272 *al.* (2013) argued that these different connectivity patterns revealed by the *Systems Analysis* of
34
35 273 the 2006 olivine zoning and compositional record may be attributed to a small but significant
36
37 274 change in the magma transport regime in the course of the 2006 eruption. They also concluded
38
39 275 that such a change - that occurred only within months - may be explained best by a short-term
40
41 276 change of the plumbing system sometime between July and October 2006. This agreed well with
42
43 277 the observation that the July and October 2006 events occurred from different eruption centres.
44
45
46
47
48
49
50
51

52
53 278 By means of the *Systems Analysis* approach, Kahl *et al.* (2015) found that three dominant magma
54
55 279 transfer routes connecting the environments M₀-M₁, M₂-mm₁ and M₁-M₂ have been active
56
57 280 during the entire period (1991-2008). These MEs therefore represent robust and long-term
58
59
60

1
2
3 281 features of Mt. Etna's plumbing system that may have facilitated the transfer of magma to the
4
5 282 surface for nearly two decades. In parallel, they also identified some sparsely frequented routes
6
7
8 283 connected to more evolved MEs such as M₃ (F₀₆₅₋₆₉). Migration routes connected to this
9
10 284 environment could be identified only in some eruption products and were therefore inferred to
11
12 285 represent temporary pathways of magma transfer that were activated only occasionally or were
13
14 286 traversed too quickly to be recorded in all olivine zoning profiles. The significance of such highly
15
16 287 evolved but rarely tapped environments and their role in Etna's historic plumbing system will be
17
18 288 evaluated further in this study. An important observation of Kahl *et al.* (2011, 2013 and 2015) is
19
20 289 the discovery of pre- and/or syn-eruptive pulses of mafic magma recharge into different MEs of
21
22 290 the plumbing system, indicated by olivine populations with forsterite M₀ (F₀₇₉₋₈₂) core and/or rim
23
24 291 compositions.
25
26
27
28
29

30 292 The application of sequential kinetic modelling revealed that the transfer of magma along the
31
32 293 three most dominant routes in Etna's modern plumbing system M₀-M₁, M₂-mm₁ and M₁-M₂
33
34 294 occurred over heterogeneous timescales ranging from days to 2 years. Although some of the
35
36 295 passageways have been sporadically active in the months and sometimes years before an
37
38 296 eruption, the magma migration activity increased in the weeks and days prior to an eruptive
39
40 297 event. For example, recharge of the environments M₁ and M₂ began years before an eruption, but
41
42 298 became more frequent in the last few days prior to its onset (Kahl *et al.*, 2015). On the other
43
44 299 hand, other environments such as mm₁ were found to represent transient features of Etna's
45
46 300 modern plumbing system and formed within the last 40 days before eruptive activity commenced
47
48 301 (Kahl *et al.*, 2015).
49
50
51
52
53
54

55 302 Kahl *et al.* (2015) conclude that temperature, water content and possibly oxidation state are the
56
57 303 main distinguishing features of the different magmatic environments. They found that: M₀ (F₀₇₉₋
58
59
60

1
2
3 304 83), the most primitive olivine population may have grown with some clinopyroxene at high water
4
5 305 contents (3.5–5.2wt %) and fO_2 conditions buffered at QFM or NNO at pressures ranging
6
7 306 between 1.5 and 3.0kbar (or even higher). Temperatures of $>1110^\circ\text{C}$ are required. The
8
9
10 307 intermediate olivine population M_1 (FO_{75-78}) could have formed over a broad spectrum of
11
12 308 conditions, but all require lower water contents (0.1–1.4wt %) at similar temperatures. The most
13
14 309 evolved, Fe-rich olivines of M_2 and M_3 (FO_{70-72} and FO_{65-69}) are the products of extremely
15
16 310 dehydrated magmas (0.2–1.1wt % H_2O for M_2 ; $<0.5\text{wt } \% H_2O$ for M_3), and probably somewhat
17
18 311 more reducing (QFM) conditions that were most probably obtained at even shallower depths and
19
20
21 312 at somewhat lower temperatures ($\sim 1080^\circ\text{C}$).

22
23
24
25 313 The findings of multi-level magma transfer between different MEs within Etna's modern
26
27 314 plumbing system derived by Kahl *et al.* (2011, 2013 and 2015) agrees with evidence from
28
29 315 geophysical (e.g. Aloisi *et al.*, 2002; Lundgren *et al.*, 2003; Murru *et al.*, 1999; Bonaccorso *et al.*,
30
31 316 2011; Patanè *et al.*, 2003, 2006 and 2013; Viccaro *et al.*, 2016a) and thermobarometric (e.g.
32
33 317 Armienti *et al.*, 2013; Giacomoni *et al.*, 2014 and 2016) studies. Thermobarometry calculations
34
35 318 indicate that clinopyroxene starts crystallising at depth $>20\text{km}$ (e.g. Armienti *et al.*, 2013;
36
37 319 Giacomoni *et al.*, 2016) and continues until eruption. The deep to intermediate crystallisation
38
39 320 range of clinopyroxene coincides with the detection of deep VT seismicity in the intermediate
40
41 321 and lower crust (10–30km, Patanè *et al.*, 2013) interpreted as periodic ascent of magma batches
42
43 322 from the mantle (Patanè *et al.*, 2013). Plagioclase was found to start crystallising at shallower
44
45 323 depths in the upper crust ($>12\text{km}$ depths), with the majority nucleating around 5–6km and
46
47 324 continue (like clinopyroxene) to crystallise until eruption (Viccaro *et al.*, 2010 and 2016b;
48
49 325 Giacomoni *et al.*, 2014 and 2016). These crystallisation levels coincide with the detection of low-
50
51 326 velocity zones using seismic tomography (e.g. Murru *et al.*, 1999). The crystallization of both,
52
53 327 plagioclase and clinopyroxene seems to be continuous in a polybaric vertical feeding system, in
54
55
56
57
58
59
60

1
2
3 328 which at least two different magma crystallisation levels have been identified (Armienti *et al.*,
4
5 329 2013; Giacomoni *et al.*, 2014 and 2016).
6
7
8

9 **This study**

10 330
11 331 Here we apply the combined methodology developed by Kahl *et al.* (2011, 2013 and 2015) to the
12
13 332 1669 eruption products, and investigate olivine zoning using novel imaging of crystallographic
14
15
16 333 orientation and trace element distribution. Our aim is to (i) test the existence and duration of pre-
17
18 334 and syn-eruptive mixing of *SET1* and *SET2* magmas, (ii) obtain the residence times of *SET1* and
19
20 335 *SET2* magmas within the plumbing system prior to eruption and (iii) reconstruct the pre- and syn-
21
22 336 eruptive history of magmatic events leading to the 1669 flank eruption.
23
24

25
26 337 We first present a brief chronology of the eruption sequence, followed by descriptions of the
27
28 338 relevant aspects of petrography and mineral chemistry, the types of zoning found in olivine and
29
30 339 their major, minor and trace element compositional characteristics. We use these data to construct
31
32 340 connectivity diagrams and carry out Systems Analysis, in order to determine the nature of magma
33
34 341 transfer throughout the plumbing system. Then we undertake a forward-modelling approach of
35
36 342 thermodynamic calculations using the *rhyolite-MELTS* software (Gualda *et al.*, 2012; Ghiorso &
37
38 343 Gualda, 2015) to constrain the physical conditions of the identified Magmatic Environments
39
40 344 (MEs). Subsequently, we perform diffusion modelling to determine the timing and duration of
41
42 345 magma mixing and magma migration between the different MEs. Finally, we synthesize our
43
44 346 findings and results to develop a conceptual model of the late stage magmatic history before and
45
46 347 during the 1669 eruption.
47
48
49
50
51

52
53
54 348 **SAMPLES**
55
56
57
58
59
60

1
2
3 349 A total of 10 lava samples and 1 **bomb** sample were studied, representing different episodes of
4
5 350 the 1669 flank eruption. **The locations of all samples studied are highlighted in Figure 1 and the**
6
7 **sampling locations and GPS coordinates are listed in Table 2.** We collected 5 lava samples from a
8
9 351 flow unit that was emplaced on March 19, 1669. These samples **erupted before March 29 and**
10
11 352 **therefore belong to the SET1 lavas as defined by Corsaro *et al.* (1996) (Fig. 1).** Another 5
12
13 353 samples were collected from a lava flow that reached the outskirts of Catania (Fig. 1). This flow
14
15 354 was emplaced after March 29 (possibly on April 4, 1669) and **therefore falls into the SET2 lavas**
16
17 355 **of Corsaro *et al.* (1996).** The bomb sample was collected at the top of the Mt. Rossi (*MtRs*) scoria
18
19 356 cone (Fig. 1). An exact eruption date for this sample is not available, but **given its location at the**
20
21 357 **top of the cone that fed most of the eruption, we infer that it erupted towards the end of the**
22
23 358 **volcanic activity and therefore belongs also to the SET2 category (erupted after March 20, 1669;**
24
25 359 **Corsaro *et al.*, 1996).**
26
27 360

361 **ANALYTICAL METHODS**

362 **X-ray fluorescence (XRF)**

363 Whole rock compositions were determined by WD-XRF analysis (*MagiX PRO XRF, Philips*) at
364 the Department for Earth & Environmental Sciences (DEES) at LMU. Major and minor elements
365 were analyzed using glass beads prepared by fusion of 1 g sample and 9 g *SPECTROMELT A12*
366 (66 % di-lithium tetraborate, 34 % lithium metaborate) in a *Panalytical Eagon 2* furnace fusion
367 system at 1150°C. Analytical precision was checked against a basalt standard and reproducibility
368 was found to be better than 0.15%.

369 **Electron microprobe (EMP)**

370 *Olivine*

1
2
3 371 Backscattered electron (BSE) images and detailed, quantitative concentration profiles (spacing
4
5 372 ~4-5 μm) of major and minor elements (Si, Fe, Mg, Mn, Ca, Ni and Cr) along different directions
6
7
8 373 in a total of 202 olivine crystals were obtained using a Cameca SX-100 electron microprobe
9
10 374 (EMP) at the Ludwig-Maximilians Universitaet (LMU) Muenchen. Run conditions were: 15kV
11
12 375 accelerating voltage, 20-30nA beam current and a focused electron beam (1 μm) for the analysis
13
14
15 376 of olivine. Peak and background counting times of 10s were used for each element. Well-
16
17 377 characterized synthetic oxides and minerals were used as analytical standards including (Si, Mg)
18
19 378 olivine, (Ca) wollastonite, (Fe) almandine and andradite, (Mn) MnTiO₃, (Cr) Cr₂O₃ and (Ni)
20
21 379 NiO.

22 23 24 25 380 *Clinopyroxene*

26
27
28 381 Major and minor element concentrations (Si, Fe, Mg, Mn, Ca, Ni, Na, Al, Ti, Cr and K) of 62
29
30 382 olivine-clinopyroxene pairs and single clinopyroxene crystals (spacing 3-6 μm) were obtained
31
32 383 using a Cameca SX-100 electron microprobe (EMP) at the Ludwig-Maximilians Universitaet
33
34 384 (LMU) Muenchen. A total of 829 single spot analyses were made at 15kV and 30nA, using a
35
36 385 focused beam (1 μm). The counting times at peak and background for each element were set to
37
38
39 386 10-20s.

40 41 42 387 *Fe-Ti oxides*

43
44
45 388 74 single-point analyses across the contact zone between adjacent olivine and Ti-magnetite were
46
47 389 made (Si, Fe, Mg, Mn, Ca, Ni, Na, Al, Ti, Cr and K) using a Cameca SX-100 at the Ludwig-
48
49 390 Maximilians Universitaet (LMU) Muenchen. Run conditions were the same as for olivine.

50
51
52
53 391 Analytical quality was ensured by analysing the reference materials as unknowns and by mineral
54
55 392 stoichiometry calculations (Deer *et al.* 2013).

56 57 58 59 393 **Electron backscatter diffraction (EBSD)**

1
2
3 394 Crystallographic orientations of olivine crystals were determined using electron backscatter
4
5 395 diffraction (EBSD, Prior *et al.*, 1999; Costa & Chakraborty, 2004) on the FEI Quanta 650
6
7 396 FEGSEM at the University of Leeds Electron Microscopy and Spectroscopy Centre (LEMAS).
8
9
10 397 Constraint of crystallographic directions in olivine with respect to the micro-analytical traverses
11
12 398 is essential for accurate diffusion modelling, as the diffusivity of different elements (e.g. Fe-Mg
13
14 399 or Ni) in olivine is strongly anisotropic, with diffusion along the c-axis six times faster than along
15
16 400 the a- and b-axes (e.g. Dohmen *et al.*, 2007a; Clark & Long, 1971).

17
18
19
20 401 To minimize uncertainty in the determination of the orientation data, orientation maps (Fig. 2c, d)
21
22 402 consisting of hundreds of EBSD point determinations were conducted for each grain. Using the
23
24 403 *HKL CHANNEL5* EBSD post-processing software, orientation-maps are generated over an entire
25
26 404 crystal, extracting hundreds to thousands of individual orientation measurements. This
27
28 405 comprehensive approach is enabled by rapid acquisition, and improves on earlier methods in
29
30 406 which only a few points per olivine grain were measured. Due to the improved coverage and
31
32 407 resolution, features such as internal lattice misorientations, sub-grain boundaries, twins and
33
34 408 pseudo-symmetries can be easily identified. EBSD mapping of this type is novel and has not been
35
36 409 routinely used by the diffusion community so far. Operating conditions are available as
37
38 410 Supplementary Data (SD) Electronic Appendix 1 (supplementary data are available for
39
40 411 downloading at <http://www.petrology.oxfordjournals.org>).

412 **Laser Ablation Inductively Coupled Plasma Mass Spectrometry (LA-ICP-MS)** 413 **mapping**

414 The elemental distribution of 7 olivine crystals was determined by LA-ICP-MS mapping at the
415 Geochemistry Laboratories of Trinity College Dublin, according to the method developed in

1
2
3 416 Ubide *et al.* (2015). The analyses were made on typical 30 μm -thick polished sections of rocks
4
5
6 417 from *SET1*, *SET2* and the *MtRs* samples.
7

8
9 418 LA-ICP-MS mapping experiments were carried out using a Photon Machines G2 193 nm excimer
10
11 419 Ar-F laser system with a Helex 2-volume ablation cell, coupled to a quadrupole Thermo iCapQc
12
13 420 mass spectrometer. The carrier gas was a mixture of He and Ar (and minor N_2 introduced via an
14
15
16 421 in-house developed variable volume smoothing device). The laser was operated with a fluence of
17
18 422 2.5 J/cm^2 . The mapping area was built by overlapping individual ablation lines to form a
19
20
21 423 rectangular grid. The laser spot size was determined by the size of olivine crystals and set at 10
22
23 424 μm . Ablation lines were built using a square laser mask, 15 $\mu\text{m/s}$ scanning speed, 10 Hz
24
25 425 repetition rate and 1 μm overlap between lines, following Ubide *et al.* (2015). A baseline
26
27 426 measurement of 30 to 40 s was allowed between ablation lines. Given the typical bright colour of
28
29 427 olivine grains in thin section, it was found that pre-ablation of the crystals using large, quick
30
31 428 rasters (e.g., 85 μm circle laser beam, 160 $\mu\text{m/s}$ scan speed, 20 Hz repetition rate, 1 μm overlap
32
33 429 between lines) improved the ablation of olivine in the subsequent mapping experiment, producing
34
35 430 sharper element maps. The analytes were ^{25}Mg , ^{27}Al , ^{29}Si , ^{31}P , ^{43}Ca , ^{45}Sc , ^{49}Ti , ^{51}V , ^{52}Cr , ^{55}Mn ,
36
37 431 ^{57}Fe and ^{60}Ni . **Seven to ten analytes were measured in each individual mapping experiment**, with
38
39 432 a total dwell cycle of 100 to 110 ms.
40
41
42
43
44

45 433 NIST612 glass reference material (Jochum *et al.*, 2011) was used at the beginning of each
46
47 434 analytical session to tune the instrument. NIST610 glass reference material (Jochum *et al.*, 2011)
48
49 435 was used as calibration standard for all mapping experiments. Data reduction and production of
50
51 436 element distribution maps was undertaken with Iolite v2.5 free software (Paton *et al.*, 2011) using
52
53 437 the 'Trace_Elements_Image' data reduction scheme (Ubide *et al.*, 2015). Following Chew *et al.*
54
55
56
57
58
59
60

1
2
3 438 (2016), maps were initially built in ‘Semi quantitative’ mode and the scales were subsequently
4
5 439 normalized to the Si content measured independently (38.5 wt.% SiO₂ from olivine EMP data).
6
7

8 9 440 **PETROLOGY**

10
11 441 The 1669 eruption products are strongly porphyritic. The rocks contain the typical Etnean
12
13 442 phenocryst assemblage of plagioclase (~12-15 vol.%), clinopyroxene (~8-11 vol.%), olivine (~3–
14
15 443 5 vol.%), and accessory Fe–Ti oxides (~<3 vol.%) embedded in a fine-grained, hypo-crystalline
16
17 444 groundmass. The groundmass consists of micro-laths of plagioclase, Fe–Ti oxides, clinopyroxene
18
19 445 and variable amounts of interstitial glass. The abundances and relative proportions of phenocrysts
20
21 446 (porphyritic index PI) can vary significantly (PI ranging between 37 and 52%) between
22
23 447 individual eruption products (cf. Corsaro *et al.*, 1996).
24
25
26
27

28
29 448 Plagioclase (An_{56–85}) forms mostly euhedral phenocrysts of variable size (0.2 - 4 mm).
30
31 449 Plagioclase phenocrysts contain multiple sequences of oscillatory zoning as well as strong
32
33 450 dissolution (sieve) textures (see also Corsaro *et al.*, 1996).
34
35

36
37 451 Clinopyroxene (Wo_{46–48}, En_{36–41}, Fs_{13–16} and Mg#73-93; see SD Electronic Appendix 2) forms
38
39 452 euhedral to subhedral phenocrysts with sizes ranging between 0.8 and 4.8 mm. Pronounced sector
40
41 453 and oscillatory zoning and inclusions of Fe–Ti oxides are common; rare inclusions of plagioclase
42
43 454 and olivine are also found.
44

45
46 455 Olivine (Fo_{51–83}; see SD Electronic Appendix 3) is mostly subhedral or anhedral with slight
47
48 456 dissolution features (e.g. rounded edges) and core–rim zonation. The size of olivine phenocrysts
49
50 457 ranges between 0.2 and 1.5 mm.
51

52
53
54 458 Opaque Fe–Ti oxides (Uvsp₃₃₋₆₀, Spn₁₃₋₂₆, Mt₃₅₋₅₃; see SD Electronic Appendix 4) form euhedral
55
56 459 to anhedral phenocrysts or occur as inclusions in clinopyroxene and olivine crystals and in melt
57
58 460 embayments.
59
60

1
2
3 461 Whole rock compositions of *SET1* and *SET2* lava and the MtRs bomb sample (Table 3) are
4
5
6 462 plotted in a TAS diagram in Fig. 3a. For comparison, bulk rock data of *SET1* and *SET2* samples
7
8 463 analysed by Corsaro *et al.* (1996) and Mulas *et al.* (2016) were added. The 1669 volcanic
9
10 464 products are hawaiitic in composition. We observe that there is a compositional offset between
11
12 465 our samples and some of the samples analysed by Corsaro *et al.* (1996). Mulas *et al.* (2016) have
13
14 466 also reported a similar offset. Our *SET1* and *SET2* samples are relatively similar in composition
15
16 467 to *SET1* samples from Corsaro *et al.* (1996) and to the pyroclast samples studied by Mulas *et al.*
17
18 468 (2016). By contrast, *SET2* lavas from Corsaro *et al.* (1996) have higher SiO₂, Al₂O₃ and total
19
20 469 alkalis (Fig. 3a, 3b, 3c) and lower TiO₂ and FeO contents (Fig. 3d-e). Our *SET1* and *SET2*
21
22 470 samples have similar MgO contents (Fig. 3h-l) to the *SET2* samples of Corsaro *et al.* (1996).
23
24 471 According to the petrological descriptions in Corsaro *et al.* (1996), their *SET2* samples contain
25
26 472 abundant plagioclase phenocrysts and as a result, a generally lower phenocryst colour index
27
28 473 ($CI_{\text{phx}} = \text{mafic mineral phenocrysts/total phenocrysts, vol.}\%$; $CI_{\text{phx}}=18$) than their *SET1* samples
29
30 474 ($CI_{\text{phx}}=36$; see their Fig. 2). Such plagioclase-rich rocks are common at Mt. Etna and, when
31
32 475 characterized by megacrystic plagioclase, are locally known as cicirara (see also Nicotra &
33
34 476 Viccaro, 2012). Given that recent studies on porphyritic mafic systems have highlighted that
35
36 477 accumulation of early mineral phases plays a major role on whole rock compositional variations
37
38 478 (e.g. Sakyi *et al.*, 2012; Larrea *et al.*, 2013; Ubide *et al.*, 2012, 2014), such variations need to be
39
40 479 evaluated in terms of differential accumulation of phenocryst phases.
41
42
43
44
45
46
47
48

49 480 To investigate this possibility, we present selected variation diagrams of bulk rock data together
50
51 481 with representative phenocryst compositions as Supplementary Data (SD) in Electronic Appendix
52
53 482 5, following the approach of Ubide *et al.* (2014). The anomalous composition of *SET2* samples
54
55 483 from Corsaro *et al.* (1996) (i.e., higher concentrations in SiO₂, Al₂O₃ and total alkalis and lower
56
57 484 concentrations in FeO and TiO₂ than the other bulk rock samples; Fig. 3) would agree with
58
59
60

1
2
3 485 preferential accumulation of plagioclase phenocrysts over olivine/clinopyroxene phenocrysts. In
4
5 486 addition, we find that our samples have higher contents of CaO (mean 10.51 wt% *SET1* and
6
7 487 10.36 wt% *SET2*) and lower concentrations of MgO (mean 5.15 wt% *SET1* and 5.02 wt% *SET2*)
8
9 488 than the *SET1* samples (Fig. 3f, g) studied by Corsaro *et al.* (1996). This could be related to
10
11 489 preferential accumulation of clinopyroxene over olivine in our samples. Therefore, we interpret
12
13 490 that the small geochemical variations observed between bulk samples could be related to
14
15 491 preferential accumulation of varied phenocryst phases. In other words, *SET1* and *SET2* lavas are
16
17 492 likely composed of similar melts accumulating slightly varied phenocryst cargoes (SD Electronic
18
19 493 Appendix 6).

24 494 **OLIVINE ZONING & COMPOSITIONAL RECORD**

25 495 **Olivine zoning patterns**

26
27
28 496 We studied a total of 202 olivine crystals ($n=117$ *SET1*; $n=68$ *SET2*; $n=17$ *MtRs*) across the 11
29
30 497 samples studied. 198 (98%) of the studied olivine crystals were characterized by systematic
31
32 498 *normal* (decreasing forsterite contents towards the rims) and to a minor extent (2%, i.e. 4
33
34 499 crystals) also *reverse* (increasing forsterite contents towards the rims) zoning patterns. These are
35
36 500 classified by zoning type into the same classification scheme employed by Kahl *et al.* (2015),
37
38 501 who studied a total of 180 olivine crystals from recent (1991-2008) eruption products of Etna.
39
40 502 The 1991-2008 olivines were characterized by multiple zoning patterns ranging from *normal* to
41
42 503 *reverse*, or more *complex* zoning, with reversely zoned cores and normally zoned rims. Based on
43
44 504 this large range of zoning patterns, Kahl *et al.* (2015) established 8 different zoning types (*Type I*
45
46 505 – *Type VIII*). Extending that classification scheme to the 1669 olivines, we observe that the
47
48 506 zoning patterns preserved in the 1669 olivines consist predominantly of simple *single-step*
49
50 507 normal or reverse zonations. This finding contrasts with the diversity of olivine zoning patterns
51
52
53
54
55
56
57
58
59
60

1
2
3 508 identified in the recent 1991-2008 eruption products. From the 8 zoning types (*Type I – Type*
4
5 509 *VIII*) described in Kahl *et al.* (2015), 6 could be recognized in the 1669 olivines. Of those, *Types*
6
7
8 510 *IV* and *VII* (Fig. 4) are the most abundant (186 crystals out of 202):
9

- 10
11 511 • *Type IV* represents normally-zoned crystals with intermediate core compositions of Fo75-
12
13 512 78 followed by low forsterite rims (\sim Fo₅₅ for *SET1*; \sim Fo₇₀ for *SET2* and *MtRs*; Fig. 4a).
14
15 513 This zoning type is by far the most abundant observed in the 1669 samples. It is identified
16
17
18 514 in 71% (i.e. 144 crystals) of the studied olivines and can be found in all samples.
19
20
21 515 • *Type VII* describes normally zoned crystals (21%, i.e. 42 crystals) with cores at Fo73-75
22
23 516 and variable rim compositions (\sim Fo₅₅ *SET1* and \sim Fo₇₀ *SET2*; Fig. 4b). Together with *type*
24
25 517 *IV* this zoning type occurs frequently in the *SET1* and *SET2* olivines. In the *MtRs* bomb
26
27 518 sample, *type VII* could not be identified.
28
29
30
31

32 519 Besides these two dominant groups, minor zoning types (16 out of 202 crystals) have been
33
34 520 identified (see SD Electronic Appendix 7):
35
36

- 37 521 • *Type I*: Reversely zoned crystals with low forsterite (Fo₇₀₋₇₂) cores and rim compositions
38
39 522 at Fo₇₅.
40
41
42
43 523 • *Type II*: Normally zoned olivines with high forsterite cores (Fo₇₉₋₈₃) and rims of variable
44
45 524 composition (Fo₇₀₋₇₁ for *SET2*).
46
47
48
49 525 • *Type VI*: Crystals consisting of weak reverse zoning with intermediate core compositions
50
51 526 (Fo₇₃₋₇₅) followed by subtle increase of the forsterite content towards the rims (\sim Fo₇₅) and
52
53 527 reverse zoning with decreasing forsterite values at the outermost rims (Fo₇₂). The
54
55 528 occurrence of this zoning type is limited to the Monte Rossi bomb sample.
56
57
58
59
60

- 1
2
3 529 • *Type VIII*: Normally zoned crystals with low forsterite core composition at Fo₇₀₋₇₂ and
4
5
6 530 rim compositions as low as Fo₅₅. This type is limited to *SET1* eruption products.
7
8

9 531 **Olivine compositional record**

10
11 532 Besides variable zonation sense and pattern, the 1669 olivine crystals differ in terms of their
12
13 533 specific core and rim compositions; the observed olivine compositions vary over a considerable
14
15
16 534 range from Fo₅₁ up to Fo₈₃. In Fig. 5a, b frequency histograms illustrate the distribution of core
17
18 535 and rim compositions of the 202 olivine crystals studied. All olivine data are provided in SD
19
20
21 536 Electronic Appendix 8.
22
23

24 537 The observed core compositions display a narrow compositional spectrum ranging from Fo₇₁ to
25
26 538 Fo₈₃ with a dominant peak at Fo₇₅ (Fig. 5a). The rim compositions, however, show a much
27
28 539 broader compositional range from Fo₅₁ up to Fo₇₈ (Fig. 5b). **Overlap between the *SET1* and**
29
30 540 ***SET2-MtRs* does occur but is minor, affecting ~6 % of the crystals (i.e. 13 crystals), which have**
31
32 541 **definably different compositional modes.** We observe different modes in the rim compositional
33
34 542 record of the *SET1*, *SET2* and *MtRs* olivines. *SET1* olivine rims display compositions ranging
35
36 543 between Fo₅₁ and Fo₆₅, whereas the *SET2* and *MtRs* rims vary between Fo₆₄ and Fo₇₇, with a peak
37
38 544 at Fo₆₉ (Fig. 5b). **This will be discussed in more detail in the following section.**
39
40
41
42
43

44 545 In Figures 5c-h minor element (MnO and CaO) plots of olivine core and rim compositions are
45
46 546 shown. The olivine cores and rims show a negative correlation between forsterite and MnO
47
48 547 content (Fig. 5c, d). The MnO contents of the olivine cores range between ~0.3 wt% for Fo₈₀₋₈₃
49
50 548 and 0.7 wt% for Fo₇₁. The rims have MnO contents ranging from 0.4 wt% for Fo₇₅ (*SET2* and
51
52 549 *MtRs* samples) up to ~1.35 wt% for Fo₅₁ (*SET1* samples).
53
54
55
56
57
58
59
60

1
2
3 550 The CaO contents of the olivine cores and rims are less variable, and range between 0.2 and 0.4
4
5 551 wt% for the cores (Fig. 5e) and between 0.3 and ~0.6 wt% (Fig. 5f) for the rims. Combining the
6
7
8 552 CaO and MnO data, we find that the *SET1* and *SET2-MtRs* olivines not only differ in their
9
10 553 forsterite contents but also in their minor element chemistry (Fig. 5g, h), defining distinct fields.
11
12 554 *SET1* olivine rims are characterized by higher MnO and CaO contents than *SET2* and *MtRs* rims.
13
14
15 555 We take this as evidence that the olivine rims of *SET1* and *SET2* formed within compositionally
16
17 556 different Magmatic Environments (MEs) that controlled both the major and minor element
18
19 557 chemistries. By contrast, *SET1* and *SET2* olivine cores formed within the same ME.
20
21
22

23 558 **Comparison with olivine compositions from recent (1991-2008) eruptions of Mt.**
24
25 559 **Etna**
26

27
28 560 For comparison, we have added in Figure 5 a-f the compositional range of the 5 different MEs
29
30 561 identified in populations of zoned olivines erupted between 1991 and 2008 from Etna volcano
31
32 562 (Kahl *et al.*, 2015).
33
34

35
36 563 We find that the core compositional record of the 1669 olivines plots within the range of known
37
38 564 olivine compositions (i.e. Fo₆₅₋₈₃) from recent and historical Etna eruptions (e.g. Clocchiatti &
39
40 565 Métrich, 1984; Tanguy & Clocchiatti 1984; Chester *et al.*, 1985; Métrich & Clocchiatti, 1989;
41
42 566 Corsaro *et al.*, 1996; Spilliaert *et al.*, 2006; Corsaro *et al.*, 2009; Kahl *et al.*, 2015). The most
43
44 567 dominant core population - that can be tracked throughout all 1669 eruption products - is Fo₇₅₋₇₈
45
46 568 (144 crystals) followed by minor populations at Fo₇₃₋₇₅ (45 crystals), Fo₇₀₋₇₂ (10 crystals) and
47
48 569 Fo₇₉₋₈₃ (3 crystals). We observe that the two prominent olivine core populations in the 1669
49
50 570 products fall within the compositional range of the known Magmatic Environments (MEs) M₁
51
52 571 (=Fo₇₅₋₇₈) and mm₁ (=Fo₇₃₋₇₅; Fig. 5).
53
54
55
56

57
58 572 Regarding rim compositions, we observe two clearly distinct groups in the 1669 olivine dataset:
59
60

- 1
2
3 573 • *SET2 and MtRs*: The rim compositional record of the *SET2* and *MtRs* olivines displays
4
5
6 574 two dominant populations at Fo₆₅₋₆₉ (49 crystals) and Fo₇₀₋₇₂ (30 crystals) and fall within
7
8 575 the range of known Magmatic Environments M₃ (=Fo₆₅₋₆₉) and M₂ (=Fo₇₀₋₇₂) described in
9
10 576 Kahl *et al.* (2015). Minor populations can be observed at Fo₇₃₋₇₅ (4 crystals) and Fo₇₅₋₇₈ (2
11
12 577 crystals) and resemble the MEs defined by the olivine cores [i.e. M₁ (=Fo₇₅₋₇₈) and mm₁
13
14 578 (=Fo₇₃₋₇₅)].
15
16
17
18 579 • *SET1*: The *SET1* olivine rim compositions define a new compositional trend undetected in
19
20 580 the recent eruption products. *SET1* rim compositions can be roughly subdivided into two
21
22 581 populations, one at Fo₆₀₋₆₅ (17 crystals) and a second, bimodal population between Fo₅₁
23
24 582 and Fo₅₉ (99 crystals) with subtle peaks at Fo₅₄ and Fo₅₇, respectively (Fig. 5b). From the
25
26 583 minor element plots we can observe that both populations clearly differ from others by
27
28 584 higher MnO and CaO contents (Fig. 5d, f). We infer therefore that *SET1* olivine rims
29
30 585 formed in a Magmatic Environment distinct from those seen in recent products, which we
31
32 586 define here as M₅.
33
34
35
36
37

38 587 **Olivine trace element mapping**

39
40 588 LA-ICP-MS element maps were obtained for selected olivine crystals Ol-5 (*Type IV*), Ol-12
41
42 589 (*Type IV*) and Ol-21 (*Type IV*) from sample 1-6 (*SET1* lavas), Ol-1 (*Type IV*) and Ol-4 (*Type IV*)
43
44 590 from sample 2-4 (*SET2* lavas), and Ol-4 (*Type IV*) and Ol-6 (*Type VI*) from the *MtRs* bomb.
45
46 591 Representative maps for minor and trace elements are presented in Fig. 6.
47
48
49
50

51 592 Olivine crystals show homogeneous cores and normally-zoned rims. Concentrations in Mg and
52
53 593 Ni decrease from the core to the rim of the crystals, and concentrations in Fe, Mn and Ca increase
54
55 594 accordingly. Such compositional change is observed in all analysed crystals, supporting EMP
56
57 595 results. In addition, LA-ICP-MS maps show that core-rim zoning is sharper in *SET1* olivines,
58
59
60

1
2
3 596 which show thicker, better developed rims than *SET2-MtRs* olivines (Fig. 6). Concentrations in
4
5 597 V, Cr, Al, P, Sc and Ti are largely homogeneous across all olivine crystals and no zoning has
6
7
8 598 been detected for these elements.
9

10
11 599 In summary, the detailed investigation of major, minor and trace element zoning profiles in 202
12
13 600 olivines reveals the existence of distinct compositional zonation (typically normal zonation)
14
15 601 throughout all eruption products studied (*SET1*, *SET2* and *MtRs*). This observation contrasts with
16
17 602 the finding of Corsaro *et al.* (1996), in which the lack of compositional zoning in olivine
18
19 603 phenocrysts (cores: Fo₇₃₋₇₇; rims: Fo₇₃₋₇₄) was reported suggesting a sub-solidus homogenization,
20
21 604 due to diffusive relaxation. An interesting observation arising from this study that has not been
22
23 605 reported so far is the compositional variability and difference between the *SET1* and *SET2-MtRs*
24
25 606 olivine rims indicating that the olivine crystals (and their melts) experienced distinct and different
26
27 607 late-stage magmatic histories following the formation of the cores. Although the *SET1* and *SET2*
28
29 608 samples investigated in this study are rather similar in whole rock composition, we find that in-
30
31 609 situ compositional information locked in the chemical stratigraphy of zoned olivine crystals
32
33 610 reveals significant differences between the *SET1* and *SET2-MtRs* samples.
34
35
36
37
38
39

40 611 **UNRAVELLING THE ZONING RECORD**

41
42
43 612 As outlined in Kahl *et al.* (2011 & 2015) a characteristic that all identified olivine populations
44
45 613 have in common, is the existence of so-called compositional plateaux: zones or regions within a
46
47 614 crystal characterized by constant forsterite values (Fig. 4; SD Electronic Appendix 7). The
48
49 615 occurrence of these plateaux was attributed to the stepwise growth of the crystals within different
50
51 616 MEs, which in turn may be characterized by a different set of thermodynamic parameters (e.g.
52
53 617 temperature, pressure, oxygen fugacity, water content and melt composition). In order to produce
54
55 618 extended plateaux of constant forsterite contents the ambient parameters must have been kept
56
57
58
59
60

1
2
3 619 constant during growth, otherwise continuous variations in the compositional profiles (as
4
5 620 observed during cooling or fractionation) rather than plateaux with sudden jumps, would be
6
7
8 621 expected (Kahl *et al.*, 2015).
9

10
11 622 We make use of the method outlined in Kahl *et al.* (2011) to illustrate the comprehensive zoning
12
13 623 record preserved in the studied olivine crystals in Systems Analysis diagrams (Fig. 7). To
14
15 624 improve the visibility of these diagrams we discarded connection lines that are recorded by fewer
16
17
18 625 than 2 crystals from the individual Systems Analysis plots (Fig. 7). A total of 6 crystals (1 from
19
20 626 *SET1*; 2 from *SET2* and 3 from *MtRs*) were affected by these reductions. We found 8 crystals that
21
22 627 are homogeneous (Fo₇₅₋₇₈) without compositional zoning and are therefore also not displayed in
23
24 628 the Systems Analysis plots. This explains why the number of connection lines (and therefore
25
26
27 629 crystals) shown in Figure 7 (i.e. 188) is less than the total number of crystals (i.e. 202) analysed.
28
29

30
31 630 We could identify 6 different MEs that account for the compositional diversity observed in the
32
33 631 1669 olivines. Of these, two are so called ‘core environments’ because the majority of the olivine
34
35 632 cores have formed in them, i.e. M₁ (=Fo₇₅₋₇₈) and mm₁ (=Fo₇₃₋₇₅). The other four are ‘rim
36
37 633 environments’ in which the *SET1* and *SET2-MtRs* olivine rims crystallized, i.e. M₂ (=Fo₇₀₋₇₂), M₃
38
39 634 (=Fo₆₅₋₆₉), M₄ (=Fo₆₀₋₆₅) and M₅ (=Fo₅₀₋₅₉). Of these, M₃ and M₅ are dominant.
40
41
42

43 635 The thickness of the connections lines shown in Fig. 7a-c is directly linked to the number of
44
45 636 crystals tracking a certain connectivity path (i.e. connection between two MEs). The majority of
46
47 637 the MEs such as M₁ (=Fo₇₅₋₇₈), M₂ (=Fo₇₀₋₇₂) and mm₁ (=Fo₇₃₋₇₅) were already identified in the
48
49 638 1991-2008 olivines **where** it was found that these MEs are well-connected in the ‘modern’
50
51 639 plumbing system of **Etna (Kahl *et al.*, 2015)**. On the other hand, more evolved environments such
52
53 640 as M₃ (=Fo₆₅₋₆₉) were only occasionally identified in the 1991-2008 samples. **In fact, the only**
54
55 641 **recent samples possessing a dominant population of olivines recording a highly-evolved**
56
57
58
59
60

1
2
3 642 environment M_3 ($=Fo_{65-69}$) were those related to paroxysms (e.g. April 11, May 7 and September
4
5 643 9) of the 2007 summit activity. Given the scarcity of examples, the M_3 environment was
6
7 644 previously believed to represent a transient, rarely sampled feature of the plumbing system (Kahl
8
9 645 *et al.*, 2015). The 1669 products, by contrast, present abundant evidence (i.e. rim compositions of
10
11 646 olivines; Fig. 5) that MEs containing highly-evolved magmas such as M_3 ($=Fo_{65-69}$), M_4 ($=Fo_{60-65}$)
12
13 647 and M_5 ($=Fo_{50-59}$) could have played a major role in historical eruptions at Mt. Etna and are likely
14
15 648 to represent long-term features of Etna's historic plumbing system. Highly-evolved environments
16
17 649 environment such as M_4 ($=Fo_{60-65}$) and M_5 ($=Fo_{50-59}$) have not been shown to be involved in
18
19 650 modern activity (Viccaro *et al.*, 2015; M. Pompilio pers. com.), implying that significant changes
20
21 651 have occurred over historical time.
22
23
24
25
26
27

28 652 In the following paragraphs, we describe the connection history observed through the Systems
29
30 653 Analysis of the 1669 eruption products and we discuss how connectivities change over time.
31
32

33 654 **1669 SET1.** In the *SET1* olivines we observe mainly two dominant connection patterns (Fig. 7a),
34
35 655 interlinking the 'core environments' M_1 ($=Fo_{75-78}$) and mm_1 ($=Fo_{73-75}$) with the highly evolved
36
37 656 'rim environment' M_5 ($=Fo_{51-59}$). Besides the main connection routes M_1 - M_5 (65 crystals) and
38
39 657 mm_1 - M_5 (23 crystals), there are minor routes connecting the environments M_1 - M_4 (14
40
41 658 connections) and M_2 - M_5 (7 connections).
42
43
44
45

46 659 **1669 SET2.** The *SET2* olivines also display two dominant populations (Fig. 7b) tracking the
47
48 660 connections M_1 - M_3 (33 crystals) and M_1 - M_2 (17 crystals). Few crystals record the histories mm_1 -
49
50 661 M_2 (8 crystals) and mm_1 - M_3 (6 crystals).
51
52
53

54 662 **1669 MtRs.** In this sample we find olivines that record fewer connections. We observe one
55
56 663 population (8 crystals) that tracks the connection M_1 - M_3 (Fig. 7c). Minor connections are related
57
58 664 to the environments mm_1 - M_2 (2 crystals) and M_1 - mm_1 (2 crystals). The connection patterns in the
59
60

1
2
3 665 *MtRs* olivines show a close resemblance to those found in the *SET2* olivines (Fig. 7c), suggesting
4
5
6 666 that the crystals contained in the *MtRs* and the *SET2* magmas experienced the same late-stage
7
8 667 magmatic history.
9

10
11 668 In summary, from the combined Systems Analysis record of the 1669 samples, we find that the
12
13 669 vast majority (96%) of the olivine cores record a common early stage magmatic history related to
14
15 670 crystal growth or residence in the Magmatic Environments M_1 ($=Fo_{75-78}$; i.e. 139 crystals) and
16
17 671 mm_1 ($=_{73-75}$; i.e. 42 crystals). The identification of four different ‘*rim environments*’ [i.e. M_5
18
19 672 ($=Fo_{50-59}$; 98 crystals), M_4 ($=Fo_{60-65}$; 14 crystals), M_3 ($=Fo_{65-69}$; 47 crystals) and M_2 ($=Fo_{70-72}$; 27
20
21 673 crystals)] suggests diverging late stage magmatic histories in *SET1* vs. *SET2-MtRs* samples,
22
23 674 following the formation of the olivine cores in the dominant environment M_1 .
24
25
26
27

28 29 675 **CHEMICAL & PHYSICAL CHARACTERISTICS OF MAGMA STORAGE**

30
31
32 676 We applied thermodynamic calculations using the *rhyolite-MELTS* software (Gualda *et al.*, 2012;
33
34 677 Ghiorso & Gualda, 2015) to characterize the MEs in which the cores and the different rims of the
35
36 678 *SET1* and *SET2-MtRs* olivines formed.
37

38
39
40 679 Following the modelling procedure outlined in Kahl *et al.* (2015), we started with the
41
42 680 identification of appropriate starting compositions (glass or whole rock) from which the most
43
44 681 primitive olivine composition observed [i.e. M_1 ($=Fo_{75-78}$)] could have crystallized. The bulk
45
46 682 composition of magma provides the largest source for variability. Therefore, we checked
47
48 683 carefully the given range of bulk compositions (Table 3) for the *SET1*, *SET2* and *MtRs* samples.
49
50 684 We find that each of these compositions could be in equilibrium with the most primitive olivine
51
52
53 685 population (Fo_{75-78}) identified in the 1669 Etna eruption products.
54
55
56
57
58
59
60

1
2
3 686 In addition to major element chemistry, water contents and the prevalent oxygen fugacity
4
5 687 conditions (fO_2) can have a significant impact on crystallization paths (e.g. Kahl *et al.*, 2015).
6
7
8 688 Micro-analytical studies of olivine hosted melt inclusions (MIs) in the 1669 eruption products
9
10 689 reveal variable, but low, total water contents (1.0 - 0.3 wt.%, e.g. Clocchiatti & Métrich, 1984;
11
12 690 Métrich & Rutherford, 1998). The oxidation state of Etna lavas has been constrained by the type
13
14
15 691 of Fe–Ti oxides present (e.g. Métrich & Clocchiatti, 1996; Kahl *et al.*, 2011), as well as through
16
17 692 experimental studies (e.g. Pompilio & Rutherford, 2002), to lie in the vicinity of the Ni–NiO
18
19
20 693 reaction (NNO) oxygen fugacity buffer.

21
22
23 694 The forward modelling strategy using the *rhyolite-MELTS* software (Gualda *et al.*, 2012; Ghiorso
24
25 695 & Gualda, 2015) was defined as follows. We started with the melt compositions provided in
26
27
28 696 Table 3 simulating fractional crystallization, following the demonstration by Kahl *et al.* (2015),
29
30 697 that equilibrium crystallization cannot explain observed compositional diversity in modern Etna
31
32 698 samples. Fractional crystallization was modelled along different fO_2 paths (QFM or NNO) for
33
34
35 699 different initial water contents (1.5 wt% to dry). Finally, the P-T space was scanned along
36
37 700 isobaric lines (3.0-0.5kbar) at a temperature range starting from liquidus down to 1050°C, in
38
39 701 agreement with the lowest temperatures obtained by geothermometry (1070 ±20°C; 1081 ± 17°C,
40
41
42 702 Kahl *et al.*, 2015) applying the geothermometer of Loucks (1996), at intervals of 5°C. The sets of
43
44 703 conditions at which olivines corresponding to the different MEs could have formed are shown in
45
46
47 704 figure 8 and the results of the MELTS simulations are summarized in SD Electronic Appendix 9.
48
49 705 The applied conditions were considered plausible for a given ME only when the full
50
51 706 compositional range of olivine corresponding to that ME (e.g. Fo₇₅₋₇₈ for M₁) could be obtained.

52
53
54 707 At melt water contents ranging from dry to 1.1 wt.%, olivine compositions corresponding to the
55
56
57 708 Magmatic Environment M₁ can be obtained at QFM or NNO, temperatures between 1060-

1
2
3 709 1170°C and pressures \leq 1kbar (Fig. 8a-d). M_1 olivines typically coexist with clinopyroxene,
4
5
6 710 plagioclase and Fe-Ti oxides with compositions that lie within the observed range of natural
7
8 711 compositions (An_{56-85} , Corsaro *et al.*, 1996; $Mg\#_{73-93}$ and Mt_{35-52} , this study). At QFM, the
9
10 712 obtained clinopyroxene compositions (i.e. $Mg\#_{81-83}$) match the mafic end of the observed natural
11
12 713 compositions whereas the modelled plagioclase compositions (i.e. An_{66-75}) fall within the
13
14 714 intermediate range of observed natural compositions. The simulated Fe-Ti oxide compositions
15
16 715 (i.e. Mt_{35-38}) match the lower end of natural compositions. At NNO, the results are similar, with
17
18 716 the distinction that the obtained Fe-Ti oxide compositions (i.e. Mt_{50-57}) fall outside the
19
20 717 compositional range of observed Fe-Ti oxides.
21
22
23

24
25 718 These observations are in agreement with the results presented in Kahl *et al.* (2015). These
26
27 719 authors found that M_1 olivines form at QFM or NNO, temperatures $\geq 1110^\circ\text{C}$ and melt water
28
29 720 contents between 0.1 and 1.4 wt.% coexisting with clinopyroxene ($Mg\#_{80-85}$), plagioclase (An_{50-}
30
31 721 83) and Fe-Ti oxide (Mt_{45-58}), using a bulk rock composition of the 2002-2003 S-flank eruption of
32
33 722 Mt. Etna (MgO content 8.17wt%) as the starting composition. M_1 -type olivines coexisting with
34
35 723 An-rich (An_{80-83}) plagioclase at QFM or NNO and low melt water contents could only be
36
37 724 reproduced at low pressures between 0.25 and 0.75kbar. The only distinction to the results
38
39 725 obtained in the present study is that M_1 olivines and Fe-Ti oxides could only coexist at oxygen
40
41 726 fugacity conditions buffered at NNO (Kahl *et al.*, 2015).
42
43
44
45
46

47 727 Evolved olivine compositions corresponding to M_3 ($=Fo_{65-69}$) can be reproduced primarily under
48
49 728 QFM conditions and lower temperatures (below 1140°C). M_3 olivines form at melt water
50
51 729 contents ranging from dry up to 1.3wt% at all pressures considered (0.5- 3.0kbar) (Fig. 8a, c)
52
53 730 together with clinopyroxene ($Mg\#_{74.5-78.4}$), plagioclase (An_{53-64}) and Fe-Ti oxide (Mt_{43-52}). At
54
55 731 NNO, M_3 olivines form at high pressures (i.e. 2.0-3.0kbar; Fig. 8b) and dry conditions only,
56
57
58
59
60

1
2
3 732 together with clinopyroxene (Mg#₇₄₋₇₉). Kahl *et al.* (2015) were able to reproduce M₃ olivines at
4
5 733 QFM, low melt water contents (0.2-0.4 wt. %), temperatures below 1100°C and all pressures
6
7 734 considered (0.5-3.0kbar) together with clinopyroxene, plagioclase and Fe-Ti oxides with the
8
9
10 735 observed compositions.

11
12
13 736 The most evolved olivine compositions M₅ (=Fo₅₁₋₅₉) identified in the 1669 samples form at
14
15 737 QFM only, under dry conditions, temperatures below 1100°C and pressures between 1.0 to
16
17 738 3.0kbar (Fig. 8a). At these conditions only clinopyroxene (Mg#74) forms with the observed
18
19 739 compositions. Olivines of this composition could not be reproduced in the study of Kahl *et al.*
20
21 740 (2015).

22
23
24
25
26 741 From our MELTS simulations we find that plagioclase is the liquidus phase of 1669 magmas at
27
28 742 all pressures and water contents considered. We observe that An-rich plagioclase compositions
29
30 743 (i.e. An₈₀₋₈₅) are not in equilibrium with any of the observed olivine populations and can form at
31
32 744 pressures from 0.5 to 3.0kbar, melt water contents of 1.5 and 2.5 wt% (the latter for An₈₅) and
33
34 745 temperatures between 1090-1144°C, irrespective of the oxygen fugacity conditions. The bulk of
35
36 746 the more evolved plagioclase compositions (i.e. An₅₃₋₇₅), however, form in equilibrium with the
37
38 747 observed olivine populations (An₅₃₋₆₄ with M₃; An₆₆₋₇₅ with M₁) but at lower melt water contents
39
40 748 (dry to 1.3 wt.%). The most evolved olivine population M₅ does not coexist with plagioclase
41
42 749 compositions in the observed range. We believe that the lower water contents, at which the bulk
43
44 750 of the evolved plagioclase crystals form in equilibrium with the majority of the observed olivine
45
46 751 and evolved clinopyroxene compositions, could be related to shallower depths reached by *SET1*
47
48 752 and *SET2* magmas (P <800bars; e.g. Métrich & Rutherford, 1998). In summary, the observed
49
50 753 differences in the MEs the olivines and their melts passed through are mainly related to changes
51
52 754 in the melt water content, oxygen fugacity and temperature.
53
54
55
56
57
58
59
60

755 TIME-INTEGRATED APPROACH - DIFFUSION MODELLING

756 Following the approach outlined in Kahl *et al.* (2011 & 2013) we have modelled the diffusive
757 relaxation of compositional zoning profiles in 150 olivines from *SET1* and *SET2* samples. The
758 criteria for the choice of concentration profiles for modelling and tests for robustness have been
759 reported in full detail in, e.g. Kahl *et al.* (2011 & 2013) and Costa *et al.* (2008). We note that the
760 compositional zoning profiles preserved in olivines from the Monte Rossi (MtRs) bomb sample
761 were not robust enough (i.e. weak zoning) for diffusion modelling and these crystals were
762 therefore discarded. The application of diffusion modelling to the identified olivine populations
763 allows us to (i) assess the timing and duration over which the crystals (plus their associated
764 melts) have been transferred between the different MEs identified and (ii) reconstruct the
765 residence times of the *SET1* and *SET2* magmas within different sections of the plumbing system
766 prior to eruption.

767 Modelling approach

768 For our modelling approach, we made use of the following 1-D expression of the diffusion
769 equation (i.e. Fick's 2nd law)

$$770 \quad \frac{\partial C_i(x,t)}{\partial t} = \frac{\partial}{\partial x} \left(D_i \frac{\partial C_i(x,t)}{\partial x} \right) \quad (1)$$

771 where C_i is the concentration of element i , x denotes the distance, D_i is the diffusion coefficient of
772 element i , and t is time. The evolution of the concentration with time (t) at different spatial
773 coordinates (x), $C_i(x, t)$, is obtained numerically using a one-dimensional finite difference
774 scheme. An example diffusion *Mathematica* code is provided as Supplementary Data (Electronic
775 Appendix 9) of Kahl *et al.* (2015) but can be obtained from the authors. In this study, we focused
776 predominantly on Fe-Mg zoning in olivine, using Fe-Mg diffusion coefficients obtained by

1
2
3 777 Dohmen *et al.* (2007a, b). Minor (Mn, Ca, Ni) and trace element (Al, P, Ti, Cr) profiles were
4
5 778 obtained and carefully checked using EMP analysis and high-resolution LA-ICP-MS mapping
6
7
8 779 (Ubide *et al.*, 2015; Fig. 6), but did not yield characteristic zoning patterns that could be used for
9
10 780 diffusion modelling.

11
12
13 781 As diffusion of most elements in olivine is strongly orientation-dependent with respect to the
14
15 782 crystal lattice, we have taken into account the effects of diffusion anisotropy. For this purpose,
16
17 783 the orientation and the angular relation of the crystallographic a-, b- and c-axis in the analysed
18
19 784 olivine crystals was determined using electron backscatter diffraction techniques EBSD (see
20
21 785 Analytical methods for more details).

22 23 24 25 26 786 **Input parameters - temperature & oxygen fugacity (f_{O_2})**

27
28
29 787 Magmatic temperatures were determined using the Fe–Mg exchange geothermometer between
30
31 788 coexisting clinopyroxene and olivine rims (Loucks, 1996) and were $1070 \pm 20^\circ\text{C}$. The oxygen
32
33 789 fugacity (f_{O_2}) conditions were set to QFM, given that at this temperature range, thermodynamic
34
35 790 calculations using *rhyolite-MELTS* (Gualda *et al.*, 2012; Ghiorso & Gualda, 2015) indicate that
36
37 791 M_3 - and M_5 -type olivine cannot be formed at NNO (Kahl *et al.*, 2015).

38
39
40
41 792 Examples of calculated diffusion models that fit the concentration profiles are shown in Figure 9.
42
43 793 Propagation of errors and uncertainties of the obtained timescales were performed following the
44
45 794 procedure described in Kahl *et al.* (2015). A frequency distribution of all calculated timescales is
46
47 795 shown in Figure 10a.

48 49 50 51 52 796 **Timescale results**

53
54
55 797 Applying the procedures outlined above we obtained 150 time estimates ($SET1=109$; $SET2=41$)
56
57 798 from modelling the diffusive relaxation of Fe-Mg zoning profiles in 150 olivine crystals (Fig.
58
59
60

1
2
3 799 10a). A summary with all modelled timescales and the sequence of MEs as recorded in the
4
5 800 chemical stratigraphy of the crystals is provided in Table 4. The observed **distribution** of
6
7 801 timescales is fairly large ranging from a minimum of a few days up to a maximum of 1.5 years,
8
9 802 with the majority (76%) to the obtained time estimates being shorter than 3 months (Fig. 10a).
10
11 803 The observed array of timescales is in good agreement with results from recent Etna eruptions
12
13 804 (e.g. Kahl *et al.*, 2011, 2013 & 2015) and other basaltic volcanoes (e.g. Albert *et al.*, 2015;
14
15 805 Viccaro *et al.*, 2016c; Rae *et al.*, 2016; Hartley *et al.*, 2016). Corresponding timescales of *SET1*
16
17 806 (red circles) and *SET2* (green squares) olivines are shown in Figure 10b. The horizontal bars
18
19 807 represent the associated 1σ errors related to uncertainties from geothermometry (see Kahl *et al.*,
20
21 808 2015 for details on error propagation procedures).

22
23
24
25
26
27 809 **1669 SET1.** Time estimates related to the initial stages of the eruption (i.e. March 11 – 20, 1669)
28
29 810 range from 16 days up to 1.5 years with the majority (61%) being shorter than 3 months (Fig.
30
31 811 10b).

32
33
34
35 812 **1669 SET2.** Time estimates related to the second half (i.e. post-March 29, 1669) of the eruptive
36
37 813 activity are shifted towards slightly shorter timescales (10 days up to ~5 months) with the
38
39 814 majority (71%) being shorter than 2 months (Fig. 10b).

40 41 42 43 815 **Timing of magma transfer**

44
45
46 816 Kahl *et al.* (2011, 2013 & 2015) demonstrated that that the application of Systems Analysis to
47
48 817 populations of zoned olivine crystals can be used to uniquely link the compositional information
49
50 818 preserved in the chemical stratigraphy of olivines with the transport dynamics of their associated
51
52 819 melts. Extending this approach to the 1669 olivines enables us to decipher diverging magmatic
53
54 820 histories in the *SET1* and *SET2-MtRs* olivines related to different magma transfer pathways
55
56 821 connecting the ‘core’ and the ‘rim’ MEs. To get an idea of the timing and duration of magma
57
58
59
60

1
2
3 822 transfer between these environments we have plotted the frequency of intrusive events as
4
5 823 functions of the different migration routes identified in the Systems Analysis in Figure 11. The
6
7
8 824 intrusion times have been re-calculated by successively subtracting the modelled olivine
9
10 825 timescales from the assumed eruption dates of the *SET1* (i.e. March 19, 1669) and *SET2* (i.e.
11
12
13 826 April 04, 1669) samples.

14
15
16 827 We observe that magma migration activity along the most prominent connection route M_1 - M_5 (65
17
18 828 crystals; Fig. 7a), as recorded in the *SET1* olivines, occurs over a range of timescales from 16
19
20 829 days up to 1.5 years (Fig. 10b). The communication between the environments M_1 and M_5 started
21
22
23 830 1.5 years (October 1667) prior to eruption onset on March 11, 1669. Starting in October and
24
25 831 becoming more frequent since November 1668, intrusion activity along this route re-kindled and
26
27 832 continued until shortly before the onset of eruptive activity (Fig. 11). Magma transfer along other,
28
29
30 833 minor routes such as mm_1 - M_5 (26 crystals; Fig. 7a), M_1 - M_4 (14 crystals; Fig. 7a) and M_2 - M_5 (7
31
32 834 crystals; Fig. 7a) occurred over shorter timescales (22 days up to 8 months; Fig. 10b) starting
33
34 835 between mid-October and early-November 1668, and becoming more frequent towards the
35
36
37 836 eruption onset (Fig. 11). We also find that the magma migration activity along M_1 - M_5 decreased
38
39
40 837 in the short term (i.e. days) before the onset of the eruption, as indicated by a decreasing number
41
42 838 of crystals recording this event (Fig. 11).

43
44
45 839 The *SET2* olivines record a different late stage magmatic history, with the pathway M_1 - M_3 (33
46
47 840 crystals; Fig. 7b) as the main transport route. Communication between the environments M_1 and
48
49
50 841 M_3 commenced between mid- to late-November 1668 and was soon followed by mixing activities
51
52 842 along other, minor routes such as M_1 - M_2 (17 crystals; Fig. 7b), mm_1 - M_2 (8 crystals; Fig. 7b) and
53
54 843 mm_1 - M_3 (6 crystals; Fig. 7b). Timescales related to these minor connection routes are shorter (13
55
56 844 days up to 3 months; Fig. 10b) and mixing occurred from mid-December 1668 (Fig. 11). Taking
57
58
59
60

1
2
3 845 the number of crystals as evidence of intensity, we observe that the intrusive and mixing activity
4
5 846 along all routes *increased* in the short-term (i.e. February 1669) both prior to and following the
6
7
8 847 eruption onset (Fig. 11).
9

10
11 848 Occasionally, we also find rare olivine crystals (n=2) that record entrainment of ‘older’ olivine
12
13 849 cores of more mafic composition, i.e. M_0 (=Fo₇₉₋₈₂, see Kahl *et al.*, 2015 for more details) from
14
15 850 the surrounding crystal mush. These olivines are overgrown by more evolved rims of
16
17
18 851 composition M_5 (=Fo₅₁₋₅₉) or M_2 (=Fo₇₀₋₇₂) and the corresponding timescales suggest that the
19
20 852 crystals were entrained in their respective host melts sometime between late-December 1668 and
21
22 853 mid-January 1669. This coincides with the observed trend of increasing magma *migration and/or*
23
24 854 *mixing activity and the development of a branched shallow magma transport system commencing*
25
26 855 *in November 1668 and continuing until the eruption onset (Fig. 11), with two dominant but*
27
28 856 *diverging magma pathways (M_1 - M_5 and M_1 - M_3) as recorded by the *SET1* and *SET2-MtRs**
29
30 857 *olivines.*
31
32
33
34
35

36 858 **PUTTING OBSERVATIONS INTO A MODEL: THE CHRONOLOGY OF**

37 859 **MAGMATIC EVENTS**

38
39
40 860 Combination of the information obtained from the Systems Analysis of the olivine zoning record
41
42 861 and temporal information from modelling the diffusive relaxation of such zoning allows
43
44 862 reconstruction of the sequence of magmatic events in the internal plumbing system of Etna
45
46 863 volcano before and during the 1669 eruption. *By considering the chemical stratigraphy preserved*
47
48 864 *in 188 olivine crystals we can infer that olivine crystals resided in or interacted with six different*
49
50 865 *Magmatic Environments (MEs) prior to eruption (Fig. 7).*
51
52
53
54

55
56 866 We observe that the vast majority (74%) of the olivine cores are connected to *the dominant*
57
58 867 *Magmatic Environment M_1 (=Fo₇₅₋₇₈) whose existence can be tracked throughout all studied*
59
60

1
2
3 868 eruption products (i.e. *SET1*, *SET2-MtRs*). The occurrence of large olivine cores with
4
5 869 compositional plateaux predominantly at Fo₇₅₋₇₈ suggests, that the crystals have resided in M₁ for
6
7
8 870 a significant period of time before moving on to other MEs. Furthermore, we find that these core
9
10 871 compositional plateaux form groups or clusters in variation diagrams (Fig. 5e, g). Taking the
11
12 872 extent of the observed compositional plateaux as evidence we infer that the instantaneous
13
14 873 ambient conditions within M₁ were held constant during the crystallisation of olivine cores. Such
15
16 874 constant conditions can exist for example within a large reservoir (e.g. sill or dyke) without large-
17
18 875 scale convection. We suggest that a reservoir M₁ existed at shallow levels ($P \leq 1$ kbar) within
19
20 876 Etna's plumbing system containing a partially degassed melt (up to 1.1 wt %; ~5.1 wt% MgO) in
21
22 877 equilibrium with olivine (Fo₇₅₋₇₈), clinopyroxene (Mg_{#81-83}), plagioclase (An₆₆₋₇₅) and Fe-Ti oxide
23
24 878 (Mt₃₅₋₅₂ depending on the fO₂: QFM or NNO buffer) at temperatures $\leq 1170^\circ\text{C}$. The depth range
25
26 879 (≤ 1 kbar; ≤ 3 km) at which M₁ olivine cores can be formed correlates with the top part of a main
27
28 880 magma storage volume (Fig. 12a) that was identified between ~2km bsl down to 8-9km bsl (e.g.
29
30 881 Patanè *et al.*, 2013; Bonaccorso *et al.*, 2011). This body lies along the western border of the high
31
32 882 Vp velocity body (HVB) (Aloisi *et al.*, 2002; Patanè *et al.*, 2003, 2006) and is interpreted as the
33
34 883 consensus main pathway for magma transport and magma accumulation at Mt. Etna (e.g. Patanè
35
36 884 *et al.*, 2013).

37
38
39
40
41
42
43
44 885 The 1669 (*SET1* and *SET2-MtRs*) olivine rims are more diverse in composition, ranging from
45
46 886 Fo₅₁ to Fo₇₈, and form distinct trends in variation diagrams (Fig. 5d, f) indicating that the
47
48 887 conditions under which the olivine rims formed were more variable. Our MELTS modelling
49
50 888 results suggest that the *SET1* (M₅=Fo₅₁₋₅₉) and *SET2* (M₃=Fo₆₅₋₆₉) rim populations can be
51
52 889 obtained over a much broader pressure range (0.5-3.0kbar) and variable water conditions (dry up
53
54 890 to 1.3wt%). Taking these observations as evidence, we think that the *SET1* and *SET2-MtRs*
55
56 891 olivine rims could reflect crystallization under polybaric conditions within two different
57
58
59
60

1
2
3 892 environments M_5 and M_3 , which are characterized by variable temperatures, water contents and
4
5 893 oxygen fugacity conditions. Polybaric crystallisation of *SET1* and *SET2-MtRs* olivine rims agrees
6
7
8 894 with findings from textural, compositional and thermobarometric studies of Etna plagioclase and
9
10 895 clinopyroxene (Giacomoni *et al.*, 2014 & 2016; Armienti *et al.*, 2013). These studies suggest that
11
12 896 clinopyroxene and plagioclase crystallization - although starting at different depths (Fig. 12b) -
13
14
15 897 occurs continuously under polybaric conditions through a vertically-extended feeding system
16
17 898 containing different magma crystallization levels (Giacomoni *et al.*, 2014 & 2016; Armienti *et*
18
19 899 *al.*, 2013). The stability field of plagioclase and clinopyroxene further indicates a large variability
20
21 900 of the water content within Etna's plumbing system (Giacomoni *et al.*, 2014 & 2016). This
22
23 901 observation agrees with the variable water contents under which the different olivine rim and
24
25 902 core populations identified in this and previous studies (Kahl *et al.*, 2015) could be obtained via
26
27 903 thermodynamic modelling.

28
29
30
31
32 904 Combining the above observations with the temporal record, obtained from diffusion modelling
33
34 905 of 150 olivine crystals, we can derive the following schematic scenario of magmatic events in the
35
36 906 plumbing system of Mt. Etna that could have lead to the 1669 flank eruption:

37
38
39
40 907 We believe that after the formation of the olivine cores under relatively constant conditions,
41
42 908 possibly within a larger reservoir M_1 located at relatively shallow levels ($P \leq 1\text{kbar}$; $\leq 3\text{km}$)
43
44 909 within Etna's plumbing system, the reservoir was intruded by a batch of more evolved, degassed
45
46 910 and possibly aphyric M_5 -type magma (Fig. 12c). From the comprehensive timescale record
47
48 911 ($n=109$) of the *SET1* olivines, we observe that intrusions into M_1 occurred as early as 1.5 years
49
50 912 (October 1667) prior to the eruption onset. From October 1668, these injections became more
51
52 913 frequent, and the *SET1* olivine rims began crystallizing. Due to the fact, that M_5 olivines only
53
54 914 form rims, and never occur as cores in the *SET1* samples, plus considering the broad pressure
55
56
57
58
59
60

1
2
3 915 range under which they can be formed, we suggest that the M_5 environment could represent a
4
5 916 feeder dyke or conduit. *SET1* olivine rims grow in this conduit as it transects the M_1 reservoir and
6
7 917 propagates further to the surface (Fig. 12c). This scenario would agree with the lack of M_5 -type
8
9
10 918 olivine cores and would also explain why the rims can be obtained over a broader pressure
11
12
13 919 interval.

14
15
16 920 The steady replenishment of M_1 that initiated in October 1668 and continued until shortly before
17
18 921 the eruption onset has probably fluidized and eroded the surrounding magma mush, resulting in
19
20 922 the formation of a local “mixing bowl” (Bergantz *et al.*, 2015; Schleicher *et al.*, 2016) within the
21
22
23 923 reservoir M_1 . The formation of such a mixing bowl is evidenced by the core and rim
24
25 924 compositions of a minor subset of olivines from the *SET1* samples, which refer to the MEs M_4
26
27 925 (=Fo60-65), M_2 (=Fo70-72) and mm_1 (=Fo73-75). The existence of such a local mixing bowl is
28
29
30 926 further underpinned by the corresponding timescale determinations (Fig. 11). We observe, for
31
32 927 example, that a major intrusive event (i.e. M_1 - M_5) is followed by a delay of only a few days or
33
34 928 weeks by a mixing (e.g. M_1 - M_4) or entrainment (e.g. M_2 - M_5 and mm_1 - M_5), event involving a
35
36
37 929 subset of crystal cores or rims that formed in these minor magmatic environments (Fig. 11). In
38
39 930 this sense, we think that these minor ME connections identified in Systems analysis of the *SET1*
40
41 931 olivines (Fig. 7a), refer to local mixing trajectories reflecting fluidization and/or mixing within
42
43
44 932 the M_1 reservoir as time proceeds. Starting in November 1668, only a few weeks after the first
45
46 933 intrusive episode into the M_1 reservoir, a second pulse of magma injections (M_3 -type magma) is
47
48
49 934 observed. However, this time the intrusive event is recorded by the *SET2* olivines, and marks the
50
51 935 onset of simultaneous magma injections, along two different pathways (M_1 - M_5 and M_1 - M_3), into
52
53
54 936 the mutual reservoir M_1 (Fig. 12d). The intrusion frequency of M_3 -type magma into M_1 increased
55
56 937 notably from December 1668, and is again followed by mixing activities along minor connection
57
58
59 938 routes (Fig. 11). As mentioned before, the steady injections of M_3 have probably caused the
60

1
2
3 939 formation of another, localised “mixing bowl” within M_1 , in which the surrounding magma mush
4
5 940 will be fluidized and eroded. This again is evidenced by a minor subset of core and rim
6
7
8 941 populations recognized in the *SET2* (and *MtRs*) olivines [i.e. $mm_1(=Fo_{73-75})$, $M_2(=Fo_{70-72})$] and a
9
10 942 short delay in the corresponding timescale record (Fig. 11). Similar to the M_5 -type olivine rims
11
12
13 943 observed in the *SET1* samples, we find that the M_3 -type rims can form under variable conditions
14
15 944 (i.e. temperature $\leq 1140^\circ$, dry-1.3wt% water contents, pressure 0.5-3.0kbar). We assume therefore
16
17 945 that the environment M_3 could represent a second feeder dyke in which the M_3 -type olivine rims
18
19 946 started to crystallize [possibly together with clinopyroxene ($Mg\#_{74-79}$), plagioclase (An_{53-64}) and
20
21 947 Fe-Ti oxide (Mt_{43-52})] when the dyke hit the major reservoir M_1 , where the previously formed
22
23 948 olivine cores have been picked up (Fig. 12d).

24
25
26
27
28 949 The simultaneous recharge of the reservoir M_1 , along the two different routes $M_1 - M_5$ and $M_1 -$
29
30 950 M_3 , increased steadily from November 1668 (evidenced by the large number of crystals tracking
31
32 951 these events) and remained high in the weeks and days prior to the eruption onset on March 11,
33
34 952 1669 (Fig. 11). We observe, however, that in the immediate days before the eruption, the number
35
36 953 of crystals recording the recharge of M_5 into M_1 decreased (Fig. 11). We speculate that the steady
37
38 954 replenishment of M_1 , in the months and weeks prior to the eruption, could have enhanced the
39
40 955 build-up of overpressure inside the reservoir. This may have resulted in the opening of a new
41
42 956 fracture system that gave rise to the development of a branched shallow feeder system with two
43
44 957 dominant, but diverging, magma pathways ($M_1 - M_5$ and $M_1 - M_3$) facilitating the sequential transfer
45
46 958 of magma into the main conduit system (Fig. 12d, e). We note that seismicity increased ca. 2
47
48 959 weeks (e.g. Mulas et al., 2016 and references therein; Tanguy and Patanè, 1996) before the
49
50 960 eruption onset, and we suggest that this could be related to *SET1* magma intruding the main
51
52 961 conduit system. Then, in the early hours of March 11, a dry fracture system opened on the south
53
54 962 flank of Etna, between Mt. Frumento (2800m a.s.l.) and Piano San Leo (1200 m a.s.l.), enabling
55
56
57
58
59
60

1
2
3 963 lateral draining of the *SET1* magma and starting the eruption (Mulas et al., 2016 and references
4
5 964 therein) (Fig. 12e).
6
7

8
9 965 Following the eruption of the *SET1* samples, the injection frequency of M_3 into M_1 remained high
10
11 966 and persisted throughout the eruption onset as recorded by the *SET2* olivines (Fig. 11). It appears
12
13 967 that shortly after the eruption onset, the local magma transfer dynamics changed resulting in the
14
15 968 disruption of the dominant pathway M_1 - M_5 , as indicated by a decreasing number of *SET1*
16
17 969 olivines tracking this history. Instead, the pathway M_1 - M_3 became a dominant feeder that
18
19 970 promoted syn-eruptive recharge and mixing in the weeks following the eruption onset (Fig. 12e),
20
21 971 resulting in the eruption of the *SET2* (and MtRs) magma.
22
23

24
25
26 972 We can only speculate about the causes for the change in transfer dynamics. One possible
27
28 973 explanation could be a pressure-induced change of the local stress field caused by the system
29
30 974 inflating with magma and repeated dyke injections (e.g. Bonafede & Danesi, 1997; Acocella &
31
32 975 Neri, 2003) of M_3 into M_1 . Alternatively, it could be that the supply of M_5 magma simply
33
34 976 decreased, resulting in the interruption of the M_1 - M_5 pathway.
35
36
37

38
39 977 We want to stress here that whilst the development of a branched feeder system is only one
40
41 978 possible scenario that can account for the events recorded in the chemical stratigraphy of the
42
43 979 1669 olivines, it is not without precedent. Kahl *et al.* (2013) observed for the 2006 summit
44
45 980 eruptions that differences in the connectivity patterns of zoned olivine populations existed for the
46
47 981 July and October episodes. They proposed that these could have been due to fluctuations in the
48
49 982 prevalent magma transport regime. They concluded that such short-term fluctuations - occurring
50
51 983 within months from each other - could be associated with modifications of the shallow plumbing
52
53 984 system; this would be an analogous event to that proposed for 1669. As further evidence, the
54
55
56
57
58
59
60

1
2
3 985 olivine rims of *SET1* and *SET2* track divergent late-stage magmatic histories (M_1 - M_5 and M_1 - M_3)
4
5 986 that are inconsistent with the progressive emptying of a mixed or hybrid reservoir.
6
7

8 987 **CONCLUSIONS**

9
10
11 988 We have applied a three-way integrated methodology linking a Systems Analysis with a time-
12
13 989 integrated study of zoned olivine populations and a forward modelling approach using
14
15 990 thermodynamic calculations with *rhyolite-MELTS* to constrain the nature and dynamics of
16
17 991 magma transfer and magma mixing before and during the 1669 flank eruption of Etna volcano.
18
19 992 System Analysis of the compositional zoning record preserved in 202 olivine crystals revealed
20
21 993 the existence of three distinct Magmatic Environments (MEs) in which the majority of the olivine
22
23 994 cores [M_1 (=Fo₇₅₋₇₈)] and rims [i.e. M_5 (=Fo₅₁₋₅₉) and M_3 (=Fo₆₅₋₆₉)] formed. Application of
24
25 995 thermodynamic calculations with the *rhyolite-MELTS* software enabled constraint of the key
26
27 996 intensive variables associated with these MEs. We found that temperature, water content and
28
29 997 oxidation state are the main distinguishing features of the different MEs.
30
31
32
33
34
35

36
37 998 Olivine cores (~Fo₇₅₋₇₈) formed in a partially degassed environment M_1 together with
38
39 999 clinopyroxene (Mg#₈₁₋₈₃), plagioclase (An₆₆₋₇₅) and, depending on the fO_2 (QFM or NNO), Fe-Ti
40
41 1000 oxide (Mt₃₅₋₅₂), at temperatures $\leq 1170^\circ\text{C}$ and pressures $< 1\text{kbar}$. The different rim populations
42
43 1001 identified in the *SET1* and *SET2-MtRs* olivines indicate diverging magmatic histories following
44
45 1002 the core formation, suggesting a bifurcated magma feeder system for the 1669 eruption. We find
46
47 1003 that *SET1* rims (i.e. Fo₅₁₋₅₉) can form under dehydrated and QFM oxygen fugacity conditions at
48
49 1004 temperatures $< 1100^\circ\text{C}$, in equilibrium with evolved clinopyroxenes (Mg#₇₂₋₇₄). The less evolved
50
51 1005 *SET2* olivine rims (=Fo₆₅₋₆₉) can be obtained at QFM or NNO oxygen fugacity conditions, at
52
53 1006 temperatures $\leq 1140^\circ\text{C}$, under variable water contents (dry up to 1.3 wt.%), and together with
54
55 1007 clinopyroxene (Mg#₇₄₋₇₉), plagioclase (An₅₃₋₆₄) and Fe-Ti oxide (Mt₄₃₋₅₂).
56
57
58
59
60

1
2
3 1008 Importantly, olivine cores define compositional plateaux formed under relatively uniform
4
5 1009 conditions, whereas olivine rims define broad compositional ranges that can form over a broad
6
7
8 1010 pressure range (0.5-3.0kbar). This suggests that olivine cores formed under relatively constant
9
10 1011 conditions, possibly within a larger reservoir M_1 that was located at shallow levels (≤ 1 kbar)
11
12 1012 within Etna's plumbing system, and olivine rims formed in dykes (M_3 and M_5) transecting the
13
14 1013 large M_1 reservoir. These results reinforce the idea of a multi-level, vertically zoned feeding
15
16 1014 system at Mount Etna, where magma can continuously experience variable chemical-physical
17
18 1015 conditions.
19
20

21
22
23 1016 Application of diffusion modelling to the zoned olivine crystals enabled us to reconstruct the
24
25 1017 timing and chronology of melt and crystal transfer prior to and during the 1669 flank eruption.
26
27 1018 We find that the pathway M_1 - M_5 was established 1.5 years prior to eruptive activity. In addition,
28
29 1019 the parallel M_1 - M_5 recharge increased notably in the months prior to eruption onset. For several
30
31 1020 weeks a bifurcated transport system with two dominant magma pathways developed along M_1 -
32
33 1021 M_5 and M_1 - M_3 dyke injections. Accompanied by vigorous seismicity, in the immediate days prior
34
35 1022 to eruption the local magma transfer dynamics changed and the M_1 - M_5 recharge activity slowed
36
37 1023 down. M_1 - M_3 recharge remained high and persisted throughout the eruption onset on March 11,
38
39 1024 which drained *SET1* lavas. In the weeks following the eruption onset, the pathway M_1 - M_3
40
41 1025 became the dominant feeder dyke promoting syn-eruptive recharge and mixing in the shallow
42
43 1026 plumbing system culminating in the eruption of the later *SET2* lavas.
44
45
46
47
48

49
50 1027 In conclusion, the three-way integrated approach used in this study allows the reconstruction of
51
52 1028 the evolutionary history of a temporally remote and hazardous flank eruption not been accessible
53
54 1029 by means of conventional volcano monitoring techniques. Combination of pre-existing and state-
55
56 1030 of-the-art petrological tools enabled us to track the magmatic events that led to the 1669 eruption
57
58
59
60

1
2
3 1031 and to decipher changes in the local magma transfer dynamics that immediately preceded the
4
5 1032 eruption onset. Forward thermodynamic modelling linked with a time-integrated study, allowed
6
7
8 1033 us to recover pre- and syn-eruptive magma storage conditions and timescales within different
9
10 1034 magma reservoirs located in the shallow plumbing system of Mt. Etna. Most importantly, we
11
12 1035 demonstrate that the time elapsed between magma injections into the shallow plumbing system
13
14 1036 and accumulation and remobilization of eruptible magma is on the order of months to weeks
15
16
17 1037 only.

1038 **FUNDING**

1039 This work was supported by an ERC Advanced Grant EVOKEs (247076) to DBD. M.K.
1040 acknowledges two postdoctoral research fellowship grants of the Deutsche
1041 Forschungsgemeinschaft (DFG) (KA 3532/1-1) and the Icelandic Centre for Research (Rannís)
1042 (152726-051). TU acknowledges funding from Science Foundation Ireland grant
1043 SFI/12/ERC/E2499.

1044 **ACKNOWLEDGMENTS**

1045 *This paper has benefited greatly from comments by G. Bergantz, N. Métrich and an anonymous*
1046 *reviewer. We thank A. Lumsden and M. Wilson for the editorial handling of the manuscript and*
1047 *for helpful comments.* We are grateful to D. Müller (LMU Munich), D. Aßbichler (LMU
1048 Munich), R. Walshaw and G. Lloyd (University of Leeds) for assistance with EMP, XRF and
1049 EBSD analysis. We wish to thank S. Chakraborty for useful suggestions and discussions of the
1050 manuscript.

1051

1052

1
2
3 1053 **REFERENCES CITED**
4

5
6
7 1054 Acocella, V. & Neri, M. (2003). What makes flank eruptions? The 2001 Etna eruption and its
8
9 1055 possible triggering mechanisms. *Bulletin of Volcanology* **65**, 517-529.

10
11
12 1056 Albert, H., Costa, F. & Marti, J. (2015). Timing of Magmatic Processes and Unrest Associated
13
14 1057 with Mafic Historical Monogenetic Eruptions in Tenerife Island. *Journal of Petrology* **56**,
15
16 1058 1945-1966.

17
18
19
20 1059 Allard, P., Behncke, B., D'Amico, S., Neri, S. & Gambino, S. (2006). Mount Etna 1993-2005:
21
22 1060 Anatomy of an evolving eruptive cycle. *Earth Science Reviews* **78**, 85-114.

23
24
25
26 1061 Aloisi, M., Cocina, O., Neri, G., Orecchio, B. & Privitera, E. (2002). Seismic tomography of the
27
28 1062 crust underneath the Etna volcano, Sicily. *Physics of the Earth and Planetary Interiors* **134**,
29
30 1063 139-155.

31
32
33
34 1064 Andronico, D., Branca, S., Calvari, S., Burton, M., Caltabiano, T., Corsaro, R.A., Del Carlo, P.,
35
36 1065 Garfi, G., Lodato, L., Miraglia, L., Murè, F., Neri, M., Pecora, E., Pompilio, M., Salerno,
37
38 1066 G. & Spampinato, L. (2005). A multi-disciplinary study of the 2002-03 Etna eruption
39
40 1067 insights into a complex plumbing system. *Bulletin of Volcanology* **67**, 314-330.

41
42
43
44 1068 Armienti, P., Innocenti, F., Petrini, R., Pompilio, M., Villari, L. (1988). Sub-aphyric alkali basalt
45
46 1069 from Mt. Etna: inferences on the depth and composition of the source magma. *Rend Soc It*
47
48 1070 *Mineralogy and Petrology* **43**, 877-891.

49
50
51
52 1071 Armienti, P., Perinelli, C. & Putirka, K.D. (2013). A new model to estimate deep-level magma
53
54 1072 ascent rates with application to Mt. Etna (Sicily, Italy). *Journal of Petrology* **54**, 795-813.

- 1
2
3 1073 Asimow, P. D. & Ghiorso, M.S. (1998). Algorithmic modifications extending MELTS to
4
5 1074 calculate sub-solidus phase relations. *American Mineralogist* **83**, 1127–1131.
6
7
8
9 1075 Barbieri, M., Cristofolini, R., Delitala, M.C., Fornaseri, M., Romano, R., Taddeucci, A. &
10
11 1076 Tolomeo, L. (1993). Geochemical and Sr-isotope data on historical lavas of Mount Etna.
12
13 1077 *Journal of Volcanology and Geothermal Research* **56**, 57-69.
14
15
16
17 1078 Behncke, B. & Neri, M. (2003). The July-August 2001 eruption of Mt. Etna (Sicily). *Bulletin of*
18
19 1079 *Volcanology* **65**, 461-476.
20
21 1080 Bergantz, G.W., Schleicher, J.M. & Burgisser, A. (2015). Open-system dynamics and mixing in
22
23 1081 magma mushes. *Nature Geoscience* **8**, 793–796
24
25
26
27 1082 Bonaccorso, A., Bonforte, A., Currenti, G., Del Negro, C., Di Stefano, A., Greco, F. (2011).
28
29 1083 Magma storage, eruptive activity and flank instability: Inferences from ground deformation
30
31 1084 and gravity changes during the 1993-2000 recharging of Mt. Etna volcano. *Journal of*
32
33 1085 *Volcanology and Geothermal Research* **200**, 245-254.
34
35
36
37 1086 Bonafede, M. & Danesi, S. (1997). Near-field modifications of stress induced by dyke injection
38
39 1087 at shallow depth. *Geophysical Journal International* **130**,435-448.
40
41
42
43 1088 Borelli, G.A. (1670). Historia et meteorologia incendii aetnaei anni 1669. In *Officina Dominici*
44
45 1089 *Ferri*, Reggio Calabria, 162 pp.
46
47
48
49 1090 Branca, S. & Del Carlo, P. (2004). Eruptions of Mt. Etna during the past 3200 years: A revised
50
51 1091 compilation integrating the historical and stratigraphic records. In: Bonaccorso, A., Calvari,
52
53 1092 S., Coltelli, M., Del Negro, C. & Falsaperla, S. (eds.) *Mt. Etna: Volcano Laboratory*.
54
55 1093 *American Geophysical Union, Geophysical Monograph* **143**, 1-27.
56
57
58
59
60

- 1
2
3 1094 Branca, S., Coltelli, M. & Groppelli, G. (2011). Geological evolution of a complex basaltic
4
5 1095 stratovolcano: Mt. Etna, Italy. *Italian Journal of Geosciences* **130**, 306-317.
6
7
8
9 1096 Branca, S., De Beni, E. & Proietti, C. (2013). The large and destructive 1669 AD eruption at Etna
10
11 1097 volcano: reconstruction of the lava flow field evolution and effusion rate trend. *Bulletin of*
12
13 1098 *Volcanology* **75**, 694.
14
15
16
17 1099 Branca, S. Azzaro, R., De Beni, E., Chester, D. & Duncan, A. (2015). Impacts of the 1669
18
19 1100 eruption and the 1693 earthquakes on the Etna Region (Eastern Sicily, Italy): An example
20
21 1101 of recovery and response of a small area to extreme events. *Journal of Volcanology and*
22
23 1102 *Geothermal Research* **303**, 25-40.
24
25
26
27 1103 Calvari, S., Coltelli, M., Neri, M., Pompilio, M. & Scribano, V. (1994). The 1991-1993 Etna
28
29 1104 eruption: chronology and lava flow-field evolution. *Acta Vulcanologica* **4**, 1-14.
30
31
32
33 1105 Carrera, P. (1636). Il Mongibello descritto in tre libri. In Catania, nel Palazzo dell'Illustrissimo
34
35 1106 Senato, per Gio. Rossi, 204 pp.
36
37
38 1107 Chester, D.K., Duncan, A.M., Guest, J.E. & Kilburn, C.R.J. (1985). *Mount Etna. The anatomy of*
39
40 1108 *a volcano*. Chapman and Hall, London.
41
42
43
44 1109 Chew, D.M., Babechuk, M.G., Cogné, N., Mark, C., O'Sullivan, G., Henrichs, I., Doepke, D. &
45
46 1110 McKenna, C.A. (2016). (LA,Q)-ICPMS trace-element analyses of Durango and McClure
47
48 1111 Mountain apatite and implications for making natural LA-ICPMS mineral standards.
49
50 1112 *Chemical Geology* **435**, 35-48.
51
52
53
54
55
56
57
58
59
60

- 1
2
3 1113 Clark, A.M. & Long, J.V.P. (1971). *The anisotropic diffusion of nickel in olivine*. In: Sherwood,
4
5 1114 J.N., Chadwick, A.V., Muir, W.M. & Swinton, F.L. (eds.) *Diffusion Processes*. Gordon and
6
7 1115 Breach, 511-521.
8
9
10
11 1116 Clocchiatti, R. & Métrich, N. (1984). La cristallisation des pyroclastes des éruptions étnéennes de
12
13 1117 1669 (Mt Rossi et 1892 (Mt Silvestri). Témoignages de contamination. *Bulletin of*
14
15 1118 *Volcanology* **47**, 908-928.
16
17
18
19 1119 Clocchiatti, R., Joron, J.L. & Treuil, M. (1988). The role of selective alkali contamination in the
20
21 1120 evolution of recent historic lavas of Mt. Etna. *Journal of Volcanology and Geothermal*
22
23 1121 *Research* **34**, 241–249.
24
25
26
27 1122 Condomines, M., Tanguy, J.C. & Michaud, V. (1995). Magma dynamics at Mount Etna:
28
29 1123 constraints from U–Th–Ra–Pb radioactive disequilibria and Sr isotopes in historical lavas.
30
31 1124 *Earth and Planetary Science Letters* **132**, 297–314.
32
33
34
35 1125 Corsaro, R.A., Métrich, N., Allard, P., Andronico, D., Miraglia, L. & Fourmentaux, C. (2009).
36
37 1126 The 1974 flank eruption of Mount Etna: An archetype for deep dike-fed eruptions at
38
39 1127 basaltic volcanoes and a milestone in Etna's recent history. *Journal of Geophysical*
40
41 1128 *Research* **114**, B07204.
42
43
44
45 1129 Corsaro, R.A., Miraglia, L. & Pompilio, M. (2007). Petrologic evidence of a complex plumbing
46
47 1130 system feeding the July-August 2001 eruption of Mt. Etna, Sicily, Italy. *Bulletin of*
48
49 1131 *Volcanology* **69**, 401–421.
50
51
52
53 1132 Corsaro, R.A., Cristofolini, R. & Patané, L. (1996). The 1669 eruption at Mount Etna:
54
55 1133 chronology, petrology and geochemistry, with inferences on the magma sources and ascent
56
57 1134 mechanisms. *Bulletin of Volcanology* **58**, 348-358.
58
59
60

- 1
2
3 1135 Costa, F. & Chakraborty, S. (2004). Decadal time gaps between mafic intrusion and silicic
4
5 1136 eruption obtained from chemical zoning patterns in olivine. *Earth and Planetary Science*
6
7 1137 *Letters* **227**, 517–530.
8
9
10
11 1138 Costa, F., Dohmen, R. & Chakraborty, S. (2008). Timescales of magmatic processes from
12
13 1139 modelling the zoning patterns of crystals. *Reviews in Mineralogy and Geochemistry* **69**,
14
15 1140 545–594.
16
17
18
19 1141 Deer, W.A., Howie, R.A. & Zussman, J. (2013). *An Introduction to the Rock-Forming Minerals.*
20
21 1142 *Mineralogical Society of Great Britain and Ireland, 510 pp.*
22
23
24
25 1143 Doglioni, C., Innocenti, F. & Mariotti, G. (2001). Why Mt. Etna? *Terra Nova* **13**, 25–31.
26
27
28 1144 Dohmen, R., Becker, H.-W. & Chakraborty, S. (2007a). Fe–Mg diffusion in olivine I:
29
30 1145 experimental determination between 700 and 1,200°C as a function of composition, crystal
31
32 1146 orientation and oxygen fugacity. *Physics and Chemistry of Melts* **34**, 389–407.
33
34
35
36 1147 Dohmen, R. & Chakraborty, S. (2007b). Fe–Mg diffusion in olivine II: point defect chemistry,
37
38 1148 change of diffusion mechanisms and a model for calculation of diffusion coefficients in
39
40 1149 natural olivine. *Physics and Chemistry of Minerals* **34**, 409–430.
41
42
43
44 1150 Ferlito, C., Viccaro, M., Nicotra, E. & Cristofolini R. (2012). Regimes of magma recharge and
45
46 1151 their control on the eruptive behaviour during the 2001-2005 period at Mt. Etna (Italy).
47
48 1152 *Bulletin of Volcanology* **74**, 533-543.
49
50
51
52 1153 Ferrara, F. (1818). *Descrizione dell’Etna con la storia delle eruzioni e il catalogo dei prodotti.*
53
54 1154 *Palermo presso Lorenzo Dato, 256 pp.*
55
56
57
58
59
60

- 1
2
3 1155 Giacomoni, P.P., Ferlito, C., Coltorti, M., Bonadiman, C. & Lanzafame, G. (2014). Plagioclase as
4
5 1156 archive of magma ascent dynamics on “open conduit” volcanoes: The 2001–2006 eruptive
6
7 1157 period at Mt. Etna. *Earth-Science Reviews* **138**, 371-393.
8
9
10
11 1158 Giacomoni, P.P., Coltorti, M., Bryce, J.G., Fahnestock, M.F. & Guitreau, M. (2016). Mt. Etna
12
13 1159 plumbing system revealed by combined textural, compositional, and thermobarometric
14
15 1160 studies in clinopyroxenes. *Contributions to Mineralogy and Petrology* **171**, 34.
16
17
18
19 1161 Ghiorso, M.S. & Sack, R.O. (1995). Chemical mass transfer in magmatic processes. IV. A
20
21 1162 revised and internally consistent thermodynamic model for the interpolation and
22
23 1163 extrapolation of liquid–solid equilibria in magmatic systems at elevated temperatures and
24
25 1164 pressures. *Contributions to Mineralogy and Petrology* **119**, 197–212.
26
27
28
29 1165 Ghiorso, M.S. & Gualda, G.A.R. (2015). An H₂O-CO₂ mixed fluid solubility model compatible
30
31 1166 with rhyolite-MELTS. *Contributions to Mineralogy and Petrology* **169**, 53.
32
33
34
35 1167 Gillot, P.Y., Kieffer, G. & Romano, R. (1994). The evolution of Mount Etna in the light of
36
37 1168 potassium-argon dating. *Acta Vulcanologica* **5**, 81-87.
38
39
40
41 1169 Gualda, G.A.R., Ghiorso, M.S., Lemons, R.V. & Carley, T.L. (2012). Rhyolite-MELTS: A
42
43 1170 modified calibration of MELTS optimized for silica-rich, fluid-bearing magmatic systems.
44
45 1171 *Journal of Petrology* **53**, 875-890.
46
47
48
49 1172 Guest, J.E. & Duncan, A.M. (1981). Internal plumbing of Mount Etna. *Nature* **290**, 584-586.
50
51
52 1173 Gvirtzman, Z. & Nur, A. (1999). The formation of Mount Etna as the consequence of slab
53
54 1174 rollback. *Nature* **401**, 782-785.
55
56
57
58
59
60

- 1
2
3 1175 Hartley, M.E., Morgan, D.J., MacLennan, J., Edmonds, M. & Thordarson, T. (2016). Tracking
4
5 1176 timescales of short-term precursors to large basaltic fissure eruptions through Fe–Mg
6
7 1177 diffusion in olivine. *Earth and Planetary Science Letters* **439**, 58–70.
8
9
10
11 1178 Hughes, J.W., Guest, J.E. & Duncan, A.M. (1990). *Changing styles of effusive eruption on Mount*
12
13 1179 *Etna since AD 1600*. In: Ryan, M.P. (ed.) *Magma transport and storage*. Wiley, New York,
14
15 1180 385– 405.
16
17
18
19 1181 Jochum, K.P., Weis, U., Stoll, B., Kuzmin, D., Yang, Q., Raczek, I., Jacob, D.E., Stracke, A.,
20
21 1182 Birbaum, K., Frick, D.A., Günther, D. & Enzweiler, J. (2011). Determination of reference
22
23 1183 values for NIST SRM 610-617 glasses following ISO guidelines. *Geostandards and*
24
25 1184 *Geoanalytical Research* **35**, 397–429.
26
27
28
29 1185 Kahl, M., Chakraborty, S., Costa, F. & Pompilio, M. (2011). Dynamic plumbing system beneath
30
31 1186 volcanoes revealed by kinetic modelling and the connection to monitoring data: an example
32
33 1187 from Mt. Etna. *Earth and Planetary Science Letters* **308**, 11–22.
34
35
36
37 1188 Kahl, M., Chakraborty, S., Costa, F., Pompilio, M., Liuzzo, M. & Viccaro, M. (2013).
38
39 1189 Compositionally zoned crystals and real-time degassing data reveal changes in magma
40
41 1190 transfer dynamics during the 2006 summit eruptive episodes of Mt. Etna. *Bulletin of*
42
43 1191 *Volcanology* **75**, 692.
44
45
46
47
48 1192 Kahl, M., Chakraborty, S., Pompilio, M. & Costa, F. (2015). Constraints on the Nature and
49
50 1193 Evolution of the Magma Plumbing System of Mt. Etna Volcano (1991–2008) from a
51
52 1194 Combined Thermodynamic and Kinetic Modelling of the Compositional Record of
53
54 1195 Minerals. *Journal of Petrology* **56**, 2025-2068.
55
56
57
58
59
60

- 1
2
3 1196 Landi, P., Francalanci, L., Pompilio, M., Rosi, M., Corsaro, R.A., Petrone, C.M., Nardini, I. &
4
5 1197 Miraglia, L. (2006). The December 2002–July 2003 effusive event at Stromboli volcano,
6
7 1198 Italy: an insight into the shallow plumbing system by petrochemical studies. *Journal of*
8
9 1199 *Volcanology and Geothermal Research* **155**, 263–284.
10
11
12
13 1200 Lanzafame, G., Neri, M., Acocella, V., Billi, A., Funicello, R. & Giordano, G. (2003). Structural
14
15 1201 features of the July–August 2001 Mount Etna eruption: evidence for a complex magma
16
17 1202 supply system. *Journal of the Geological Society of London* **160**, 531–544.
18
19
20
21 1203 Larrea, P., França, Z., Lago, M., Widom, E., Galé, C. & Ubide, T. (2013). Magmatic processes
22
23 1204 and the role of antecrysts in the genesis of Corvo Island (Azores Archipelago, Portugal).
24
25 1205 *Journal of Petrology* **54**, 769–793.
26
27
28
29 1206 Loucks, R.R. (1996). A precise olivine–augite Mg–Fe-exchange geothermometer. *Contributions*
30
31 1207 *to Mineralogy and Petrology* **125**, 140–150.
32
33
34
35 1208 Lundgren, P., Berardino, P., Coltelli, M., Fornaro, G., Lanari, R., Puglisi, G., Sansosti, E. &
36
37 1209 Tesauro, M. (2003). Coupled magma chamber inflation and sector collapse slip observed
38
39 1210 with synthetic aperture radar interferometry on Mt. Etna volcano. *Journal of Geophysical*
40
41 1211 *Research* **108**, 2247–2267.
42
43
44
45 1212 Mancino, C. (1669). *Narrativa del fuoco uscito da Mongibello il dì undici di marzo del 1669.*
46
47 1213 *Messina, Giuseppe Bisagni.*
48
49
50
51 1214 Métrich, N. & Clocchiatti, R. (1989). Melt inclusion investigation of the volatile behaviour in
52
53 1215 historic alkali basaltic magmas of Etna. *Bulletin of Volcanology* **51**, 185–198.
54
55
56
57 1216 Métrich, N. & Clocchiatti, R. (1996). Sulphur abundance and its speciation in oxidized alkaline
58
59 1217 melts. *Geochimica et Cosmochimica Acta* **60**, 4151–4160.
60

- 1
2
3 1218 Métrich, N. & Rutherford, M.J. (1998). Low pressure crystallization paths of H₂O-saturated
4
5 1219 basaltic-hawaiitic melts from Mt Etna: Implications for open-system degassing of basaltic
6
7 1220 volcanoes. *Geochimica et Cosmochimica Acta* **62**, 1195–1205.
8
9
10
11 1221 Métrich, N., Allard, P., Spilliaert, N., Andronico, D. & Burton, M. (2004). 2001 flank eruption of
12
13 1222 the alkali and volatile-rich primitive basalt responsible for Mount Etna's evolution in the
14
15 1223 last three decades. *Earth and Planetary Science Letters* **228**, 1-17.
16
17
18
19 1224 Mulas, M., Cioni, R., Andronico, D. & Mundula, F. (2016). The explosive activity of the 1669
20
21 1225 Monti Rossi eruption at Mt. Etna (Italy). *Journal of Volcanology and Geothermal Research*
22
23 1226 **328**, 115-133.
24
25
26
27 1227 Murru, M., Montuori, C., Wyss, M., Privitera, E. (1999). The locations of magma chambers at
28
29 1228 Mt. Etna, Italy, mapped by b-values. *Geophysical Research Letters* **26**, 2553–2556.
30
31
32
33 1229 Nicotra, E. & Viccaro, M. (2012). Unusual magma storage conditions at Mt. Etna (Southern
34
35 1230 Italy) as evidenced by plagioclase megacryst-bearing lavas: implications for the plumbing
36
37 1231 system geometry and summit caldera collapse. *Bulletin of Volcanology* **74**, 795–815.
38
39
40 1232 Patanè, D., De Gori, P., Chiarabba, C. & Bonaccorso, A. (2003). Magma ascent and the
41
42 1233 pressurisation of Mt. Etna's volcanic system. *Science* **299**, 2061–2063.
43
44
45
46 1234 Patanè, D., Barberi, G., Cocina, O., De Gori, P. & Chiarabba, C. (2006). Time resolved seismic
47
48 1235 tomography detects magma intrusions at Mount Etna. *Science* **313**, 821–825.
49
50
51
52 1236 Patanè, D., Aiuppa, A., Aloisi, M., Behncke, B., Cannata, A., Coltelli, M., Di Grazia, G.,
53
54 1237 Gambino, S., Gurrieri, S., Mattia, M. & Salerno, G. (2013). Insights into magma and fluid
55
56 1238 transfer at Mount Etna by a multiparametric approach: A model of the events leading to the
57
58 1239 2011 eruptive cycle. *Journal of Geophysical Research - Solid Earth* **118**, 3519–3539.
59
60

- 1
2
3 1240 Paton, C., Hellstrom, J., Paul, B., Woodhead, J. & Hergt, J. (2011). Iolite: freeware for the
4
5 1241 visualization and processing of mass spectrometric data. *Journal of Analytical Atomic*
6
7 1242 *Spectrometry* **26**, 2508–2518.
8
9
10
11 1243 Pompilio, M. & Rutherford, M. J. (2002). Pre-eruption conditions and magma dynamics of recent
12
13 1244 amphibole-bearing Etna basalt. American Geophysical Union, Fall Meeting 2002, Abstracts
14
15 1245 V61A-1354.
16
17
18
19 1246 Prior, D. J., Boyle, A. P., Brenker, F., Cheadle, M. C., Day, A., Lopez, G., Peruzzo, L., Potts, G.
20
21 1247 J., Reddy, S., Spiess, R., Timms, N. E., Trimby, P., Wheeler, J. & Zetterstrom, L. (1999).
22
23 1248 The application of electron backscatter diffraction and orientation contrast imaging in the
24
25 1249 SEM to textural problems in rocks. *American Mineralogist* **84**, 1741–1759.
26
27
28
29 1250 Rae, A.S.P., Edmonds, M., Maclennan, J., Morgan, D., Houghton, B., Hartley, M.E. & Sides, I.
30
31 1251 (2016). Time scales of magma transport and mixing at Kilauea Volcano, Hawai'i. *Geology*,
32
33 1252 **44**, 463-466.
34
35
36
37 1253 **Recupero, G. (1815). Storia naturale e generale dell'Etna. Stamperia della Regia Università degli**
38
39 1254 **Studi, Catania, doi:10.3931/e-rara-11880.**
40
41
42
43 1255 **Rittmann, A. (1965). Notizie sull'Etna. Supplemento al *Nuovo Cimento* **3**(I), 1117–1123.**
44
45
46 1256 Sakyi, P.A., Tanaka, R., Kobayashi, K. & Nakamura, E. (2012). Inherited Pb isotopic records in
47
48 1257 olivine antecryst-hosted melt inclusions from Hawaiian lavas. *Geochimica et*
49
50 1258 *Cosmochimica Acta* **95**, 169–195.
51
52
53
54 1259 Schleicher, J.M, Bergantz, G.W., Breidenthal, R.E. & Burgisser, A. (2016). Time scales of
55
56 1260 crystal mixing in magma mushes. *Geophysical Research Letters* **43**, 1543–1550.
57
58
59
60

- 1
2
3 1261 Schiano, P., Clocchiatti, R., Ottolini, L. & Busà, T. (2001). Transition of Mount Etna lavas from
4
5 1262 a mantle-plume to an island-arc magmatic source. *Nature* **412**, 900-904.
6
7
8
9 1263 Spilliaert, N., Allard, P., Métrich, N. & Sobolev, A.V. (2006). Melt inclusion record of the
10
11 1264 conditions of ascent, degassing and extrusion of volatile-rich alkali basalt during the
12
13 1265 powerful 2002 flank eruption of Mount Etna (Italy). *Journal of Geophysical Research* **111**,
14
15 1266 B04203.
16
17
18
19 1267 Stevens, N.F., Murray, J.B., Wadge, G. (1997). The volume and shape of the 1991-1993 lava
20
21 1268 flow field at Mount Etna, Sicily. *Bulletin of Volcanology* **58**, 449-454.
22
23
24
25 1269 Tanguy, J.C. (1980). L'Etna: étude pétrologique et paléomagnétique: implications
26
27 1270 volcanologiques, 618 p. PhD thesis, University of Paris.
28
29
30 1271 Tanguy, J.C. & Clocchiatti, R. (1984). The etnean lavas, 1977-83: petrology and mineralogy.
31
32 1272 *Bulletin of Volcanology* **47**, 879-894.
33
34
35
36 1273 Tanguy, J.C. & Patané, G. (1996). *L'Etna et le monde des volcans*. Diderot Editeur Paris, France.
37
38
39 1274 Tanguy, J.C., Condomines, M., Le Goffe, M., Chillemi, V., La Delfa, S. & Patané G. (2007).
40
41 1275 Mount Etna eruptions of the last 2,750 years: revised chronology and location through
42
43 1276 archeomagnetic and ^{226}Ra - ^{230}Th dating. *Bulletin of Volcanology* **70**, 55–83.
44
45
46
47 1277 Ubide, T., Arranz, E., Lago, M., Galé, C. & Larrea, P. (2012). The influence of crystal settling on
48
49 1278 the compositional zoning of a thin lamprophyre sill: a multimethod approach. *Lithos* **132** –
50
51 1279 **133**, 37-49.
52
53
54
55
56
57
58
59
60

- 1
2
3 1280 Ubide, T., Galé, C., Larrea, P., Arranz, E. & Lago, M. (2014). Antecrysts and their effect on rock
4
5 1281 compositions: the Cretaceous lamprophyre suite in the Catalonian Coastal Ranges (NE
6
7 1282 Spain). *Lithos* **206–207**, 214-233.
8
9
10
11 1283 Ubide, T., McKenna, C.A., Chew, D.M. & Kamber, B.S. (2015). High-resolution LA-ICP-MS
12
13 1284 trace element mapping of igneous minerals: In search of magma histories. *Chemical*
14
15 1285 *Geology* **409**, 157-168.
16
17
18
19 1286 Viccaro, M., Giacomoni, P.P., Ferlito, C. & Cristofolini, R. (2010). Dynamics of magma supply
20
21 1287 at Mt. Etna volcano (Southern Italy) as revealed by textural and compositional features of
22
23 1288 plagioclase phenocrysts. *Lithos* **116**, 77-91.
24
25
26
27 1289 Viccaro, M., Calcagno, R., Garozzo, I., Giuffrida, M. & Nicotra, E. (2015). Continuous magma
28
29 1290 recharge at Mt. Etna during the 2011–2013 controls the style of volcanic activity and
30
31 1291 compositions of erupted lavas. *Mineralogy and Petrology* **109**, 67–83.
32
33
34
35 1292 Viccaro, M., Zuccarello, F., Cannata, A., Palano, M. & Gresta S. (2016a). How a complex
36
37 1293 basaltic volcanic system works: constraints from integrating seismic, geodetic, and
38
39 1294 petrological data at Mount Etna volcano during the July-August 2014 eruption. *Journal of*
40
41 1295 *Geophysical Research – Solid Earth* **121**, 5659-5678.
42
43
44
45 1296 Viccaro, M., Barca, D., Bohron, W.A., D’Orlando, C., Giuffrida, M., Nicotra, E. & Pitcher, B.W.
46
47 1297 (2016b). Crystal residence times from trace element zoning in plagioclase reveal changes in
48
49 1298 magma transfer dynamics at Mt. Etna during the last 400 years. *Lithos* **248-251**, 309-323.
50
51
52
53 1299 Viccaro, M., Giuffrida, M., Nicotra, E. & Cristofolini, R. (2016c). Timescales of magma storage
54
55 1300 and migration recorded by olivine crystals in basalts of the March-April 2010 eruption at
56
57 1301 Eyjafjallajökull volcano, Iceland. *American Mineralogist* **101**, 222-230.
58
59
60

1
2
3 1302 **FIGURE CAPTIONS**
4
5

6
7 1303 **Fig. 1** (a) Location and geodynamic setting of Mt. Etna with respect to the Apennine subduction
8
9 1304 front, the Malta escarpment (dashed line) and the subduction-related Aeolian island arc to the
10
11 1305 north. (b) Digital map of the S-flank of Mt. Etna illustrating the spatial distribution of the 1669
12
13 1306 lava flow front and the progressive opening of the eruptive fissures (1-5). The different lava flow
14
15 1307 units are illustrated in distinct colours to highlight the temporal evolution of the flow field.
16
17 1308 Sample localities of the *SET1* (1-6/10) and *SET2* (2-1/5) lava flows and the *MtRs* bomb are
18
19 1309 marked with asterisks.
20
21
22
23

24 1310 **Fig. 2** Electron backscatter diffraction (EBSD) mapping of olivine. (a-b) False colour Backscatter
25
26 1311 electron (BSE) images of olivine crystals that erupted during the second half (i.e. *SET2*) of the
27
28 1312 1669 flank eruption. (c-d) Electron backscatter diffraction (EBSD) maps of the same crystals (i.e.
29
30 1313 1669 *SET2* 2-1 Ol-6 and 2-4 Ol-6). Different colours in the corresponding EBSD maps refer to
31
32 1314 different orientations of the three measured Euler angles indicating different orientations of the
33
34 1315 crystallographic a-, b- and c-axis in the olivines. Note that the application of EBSD mapping
35
36 1316 makes it possible to distinguish individual crystals. Individual step sizes used for the EBSD
37
38 1317 orientation maps are: 22.56 μm for 2-1 Ol-6 and 20.88 μm for 2-4 Ol-6.
39
40
41
42
43

44 1318 **Fig. 3** (a) Total alkali vs. silica diagram (wt.%) of 1669 samples studied by Corsaro *et al.* (1996)
45
46 1319 and from this study (*SET1*: filled diamond; *SET2*: triangle; *MtRs*: circle). (b-l) Major element
47
48 1320 concentrations of whole rocks of *SET1*, *SET2* and *MtRs* samples of this study and of Corsaro *et*
49
50 1321 *al.* (1996).
51
52
53

54 1322 **Fig. 4** Illustration of the most common zoning types identified in the 1669 olivine crystals.
55
56 1323 Columns: Rim to core and rim to rim zoning profiles; Arrows in BSE images display direction of
57
58
59
60

1
2
3 1324 electron microprobe traverse. Rows: Zoning types as functions of eruption phases: *SET1*, *SET2*
4
5 1325 and *MtRs*. Bottom row: Displays complexities of the different zoning types as identified in 1991-
6
7 1326 93 samples (Kahl *et al.*, 2015). Fo: Forsterite; $Fo=100*(Mg/[Mg+Fe])$. (a) Type IV, normally
8
9 1327 zoned crystals with cores at Fo_{75-78} and rims at $\sim Fo_{55}$ (*SET1*) or $\sim Fo_{70}$ (*SET2* and *MtRs*). (b) Type
10
11 1328 VII, normal zoning with core at Fo_{73-75} and variable rims. Placeholders indicate that a particular
12
13 1329 zoning type could not be identified in the corresponding eruption product(s).
14
15
16
17

18 1330 **Fig. 5** (a-b) Frequency histograms of core and rim compositions of 202 olivine crystals erupted
19
20 1331 during the 1669 flank eruption. (c-d) MnO versus Forsterite content of olivine cores and rims. (e-
21
22 1332 f) CaO versus Forsterite content of olivine cores and rims. (g-h) MnO versus CaO plots of core
23
24 1333 and rim compositions. Coloured areas: Compositional range of the 5 different olivine populations
25
26 1334 identified in the 1991-2008 eruption products (Kahl *et al.*, 2015). Fo: Forsterite,
27
28 1335 $Fo=100*(Mg/[Mg+Fe])$.
29
30
31
32

33 1336 **Fig. 6** LA-ICP-MS element maps for Ni, Mn, Sc and P on representative olivine crystals from
34
35 1337 *SET1*, *SET2* and *MtRs* samples. Mapped areas are marked with white rectangles on false colour
36
37 1338 BSE images (black arrows indicate the direction of the electron microprobe traverses). LA-ICP-
38
39 1339 MS maps are constructed with the Iolite module 'Images from integrations' using 'Cold Warm'
40
41 1340 colour scales.
42
43
44
45

46 1341 **Fig. 7** Individual Systems Analysis diagrams of zoning patterns recorded in a total of 188 olivine
47
48 1342 crystals contained in the *SET1* (a), *SET2* (b) and *MtRs* (c) samples of the 1669 eruption. The
49
50 1343 number of olivine zoning patterns depicted in the Systems Analysis plots is smaller than the total
51
52 1344 number of crystals investigated ($n=202$). Minor connection lines recorded by only one crystal
53
54 1345 have been removed to improve visibility. Each coloured box represents a different Magmatic
55
56 1346 Environment (ME) as identified based on the six different olivine core and rim populations.
57
58
59
60

1
2
3 1347 Connection lines between these MEs represent zoning patterns recorded in populations of olivine
4
5 1348 crystals. The variable thickness of the connection lines refers to the number of crystals tracking
6
7
8 1349 certain connectivities. The corresponding numbers are given next to each connection line. The
9
10 1350 arrows indicate the direction of the zoning patterns as recorded in the olivine crystals (arrow
11
12
13 1351 heads point in the direction of olivine rims).

14
15
16 1352 **Fig. 8** Olivine compositions (Fo mol%) obtained from fractional crystallization (FC) simulations
17
18 1353 using *rhyolite-MELTS* (Gualda *et al.*, 2012; Ghiorso and Gualda, 2015). The simulations were
19
20 1354 performed using the bulk rock compositions shown in Table 3 at the quartz–fayalite–magnetite
21
22 1355 (QFM) and the Ni–NiO (NNO) oxygen buffers, and variable water contents (dry to 1.5 wt%
23
24 1356 water). Vertical axis: crystallization temperature in degrees Celsius; horizontal axis: forsterite
25
26 1357 content. Filled squares: olivine compositions obtained for a given isobaric cooling path. M₁, M₃
27
28 1358 and M₅: compositional range of olivine core and rim populations characterizing the dominant
29
30 1359 ‘core’ [i.e. M₁ (= Fo_{75–78})] and ‘rim forming’ [i.e. M₃ (= Fo_{65–69}) and M₅ (= Fo_{51–59})]
31
32 1360 environments.

33
34
35
36
37
38 1361 **Fig. 9** Diffusion model fits. (a-d) False colour BSE images of representative olivine crystals.
39
40 1362 Black lines: Directions of EMP traverses. (e-h) Core to rim concentration profiles of olivine
41
42 1363 crystals erupted during the 1669 flank eruption of Mt. Etna. Blue circles: EMP traverses showing
43
44 1364 concentration profiles for Forsterite [100*Mg/ (Mg+Fe), in mol%]. **Black stippled lines: Initial**
45
46 1365 **conditions**; Red lines: Best fit diffusion models for the observed zoning profiles. **Numbers in days**
47
48 1366 **indicate diffusive timescales obtained from best fit model solutions.** M₁, M₃, M₄ and M₅ indicate
49
50 1367 core and rim formation within distinct Magmatic Environments. (i-l) Stereographic lower
51
52 1368 hemisphere plots depicting the angular relations between the major crystallographic directions (a-
53
54
55
56
57
58
59
60

1
2
3 1369 , b- and c-axis) in olivine and the directions of the analytical traverses. Olivine orientation data
4
5
6 1370 were obtained using EBSD technique (see *Methods* section for full details).
7

8
9 1371 **Fig. 10** Comprehensive timescale record obtained from modelling the diffusive modification of
10
11 1372 Fe-Mg concentration profiles preserved in a total of 150 olivine crystals that fulfilled the
12
13 1373 robustness criteria described in Kahl *et al.* (2011) and Costa *et al.* (2008). (a) Frequency
14
15 1374 distribution of timescales for *SET1* (gray) and *SET2* (green) olivine crystals. Bin size: 20 days.
16
17 1375 (b) Compilation of calculated timescales as a function of crystal number including 1σ
18
19 1376 uncertainties arising from geothermometry. Coloured symbols refer to mixing timescales
20
21 1377 obtained from modelling individual *SET1* (gray diamonds) and *SET2* (green triangles) olivines.
22
23 1378 Modelling parameters: $T=1070\pm 20^\circ\text{C}$ and $f\text{O}_2=\text{QFM}$. Diffusion models performed in this study
24
25 1379 used the Fe-Mg inter-diffusion coefficients provided by Dohmen *et al.* (2007a, b). No diffusion
26
27 1380 timescales for *MtRs* olivines were obtained, as EMP profiles did not fulfil robustness criteria.
28
29
30
31
32

33 1381 **Fig. 11** Calculated timescales of intrusive events into Etna's shallow plumbing system along
34
35 1382 different transport routes. Coloured symbols refer to individual intrusion times along different
36
37 1383 transport pathways calculated by subtracting the mixing timescales from the eruption dates of
38
39 1384 *SET1* (i.e. March 19, 1669) and *SET2* (i.e. April 04, 1669) samples. Black symbols refer to
40
41 1385 intrusion times related to rarely connected MEs such as $M_0\text{-}M_5$; $M_0\text{-}M_2$ and $M_2\text{-}M_3$ [M_0 ($=\text{FO}_{79\text{-}}$
42
43 1386 83), not displayed in Figure 7]. Red dashed line (E) marks the overall eruption onset (i.e. March
44
45 1387 11, 1669); Shaded area indicates the approximate range of seismic activity preceding the onset of
46
47 1388 the 1669 eruption. Contemporary records report that vigorous seismicity preceded the eruption by
48
49 1389 approximately two weeks and that earthquake intensity increased in the days (starting on March
50
51 1390 8, 1669) prior to the eruption onset (e.g. Mulas *et al.*, 2016 and references therein).
52
53
54
55
56
57
58
59
60

1
2
3 1391 **Fig. 12** (a) Schematic illustration depicting the approximate depth of the reservoir M_1 and the
4
5 1392 dyke-like environments M_5 and M_3 in which the *SET1* (M_5) and the *SET2-MtRs* (M_3) olivine rims
6
7 1393 formed. Inserts list the physical conditions of the three environments obtained by thermodynamic
8
9 1394 modelling using *rhyolite-MELTS*. For comparison the depths contours of the high Vp velocity
10
11 1395 body (HVB; [8] Aloisi et al., 2002; [9-10] Patanè et al., 2003 & 2006) and the consensus main
12
13 1396 magma pathway (grey arrow) (e.g. [11] Patanè et al., 2013) are shown. (b) Schematic
14
15 1397 reconstruction of Etna's vertical feeding system (from Giacomoni et al., 2014, 2016) from
16
17 1398 plagioclase and clinopyroxene crystallisation depths ([1] Giacomoni et al., 2014; [2] Giacomoni
18
19 1399 et al., 2016; [3] Armienti et al., 2013). Vertical bars represent the depth range of low-velocity
20
21 1400 zones detected by [4] Bonaccorso et al. (2011), [5] Lundgren et al. (2003) and [6] Murru et al.
22
23 1401 (1999). For comparison the major stratigraphic units (AFM: Apennine Maghrebian folds; HB:
24
25 1402 Hyblean Platform; UC: Upper Crust) underlying Mt. Etna are shown. (c-e) Schematic
26
27 1403 reconstruction of the sequence and chronology of magmatic events in the internal plumbing of
28
29 1404 Mt. Etna before and during the 1669 flank eruption. (c) Dyke intrusions of M_5 -type magma into
30
31 1405 the major reservoir M_1 (=F₀₇₅₋₇₈) commenced 1.5 years prior to the eruption onset. Since October
32
33 1406 1668 repeated dyke injections of M_5 into M_1 resulting in the formation of the *SET1* olivine rims.
34
35 1407 (d) Starting in November 1668, a new batch of magma (M_3 -type) intruded the reservoir M_1 as
36
37 1408 recorded in the chemical stratigraphy of the *SET2* olivines. Intrusions of M_3 -type magma into M_1
38
39 1409 resulted in the formation of the *SET2* olivines rims. In the months and weeks prior to the
40
41 1410 eruption, simultaneous injections of M_5 - and M_3 -type magma into the M_1 reservoir occurred and
42
43 1411 continued until the eruption onset. A branched feeder system with two dominant but diverging
44
45 1412 magma transport routes M_1 - M_5 and M_1 - M_3 developed. (e) Change of magma transport dynamics
46
47 1413 shortly after the beginning of the 1669 flank eruption resulting in the disruption of the pathway
48
49 1414 M_1 - M_5 and the stabilisation of the transport route M_1 - M_3 , that facilitated syn-eruptive magma
50
51
52
53
54
55
56
57
58
59
60

1
2
3 1415 recharge and magma mixing in the weeks following the eruption onset. See main text for more
4
5
6 1416 details.

7
8
9 1417 **TABLE CAPTIONS**

10
11
12 1418 **Table 1** Summary of 17th century flank activity

13
14
15
16 1419 **Table 2** Sample locations

17
18
19 1420 **Table 3** Bulk rock compositions of *SET1*, *SET2* and *MtRs* eruption products

20
21
22 1421 **Table 4** Comprehensive timescale record of *SET1* and *SET2* olivines

23
24
25 1422
26
27
28
29
30
31
32
33
34
35
36
37
38
39
40
41
42
43
44
45
46
47
48
49
50
51
52
53
54
55
56
57
58
59
60

1
2
3
4
5
6
7
8
9
10
11
12
13
14
15
16
17
18
19
20
21
22
23
24
25
26
27
28
29
30
31
32
33
34
35
36
37
38
39
40
41
42
43
44
45
46
47
48
49
50
51
52
53
54
55
56
57
58
59
60

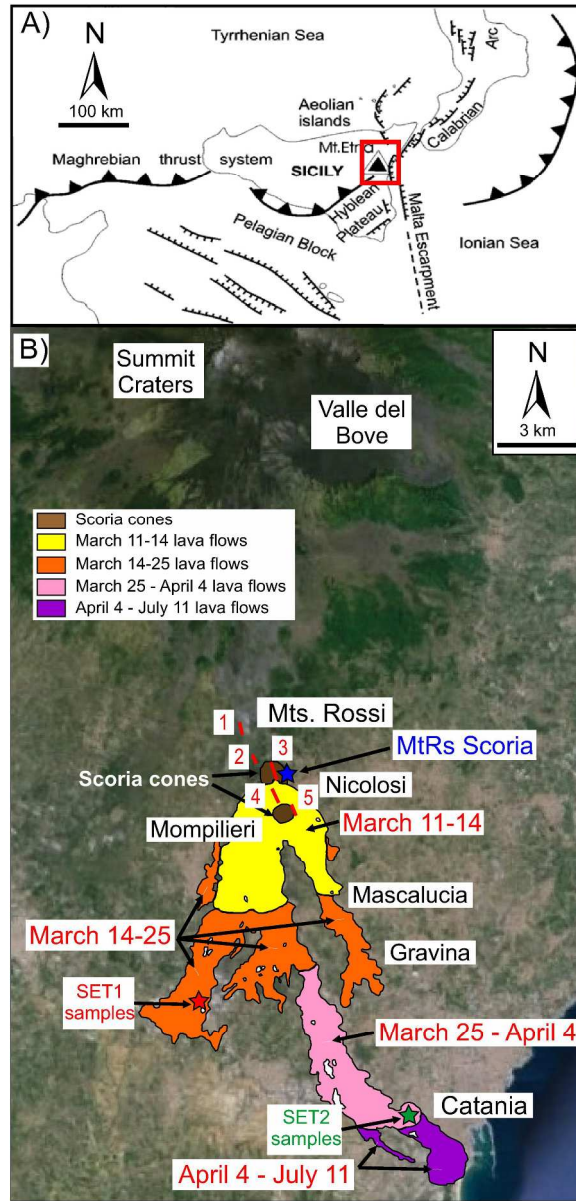


Figure 1

201x418mm (300 x 300 DPI)

1
2
3
4
5
6
7
8
9
10
11
12
13
14
15
16
17
18
19
20
21
22
23
24
25
26
27
28
29
30
31
32
33
34
35
36
37
38
39
40
41
42
43
44
45
46
47
48
49
50
51
52
53
54
55
56
57
58
59
60

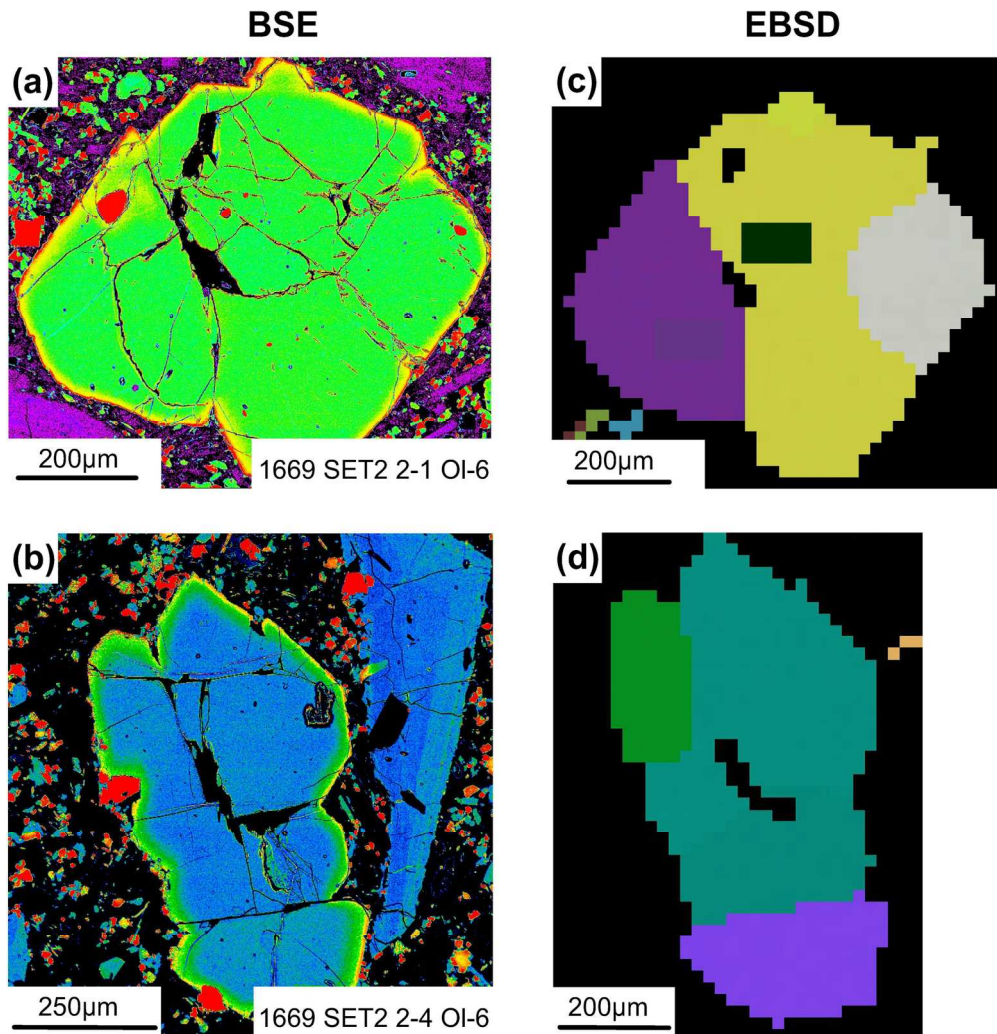


Figure 2

166x171mm (300 x 300 DPI)

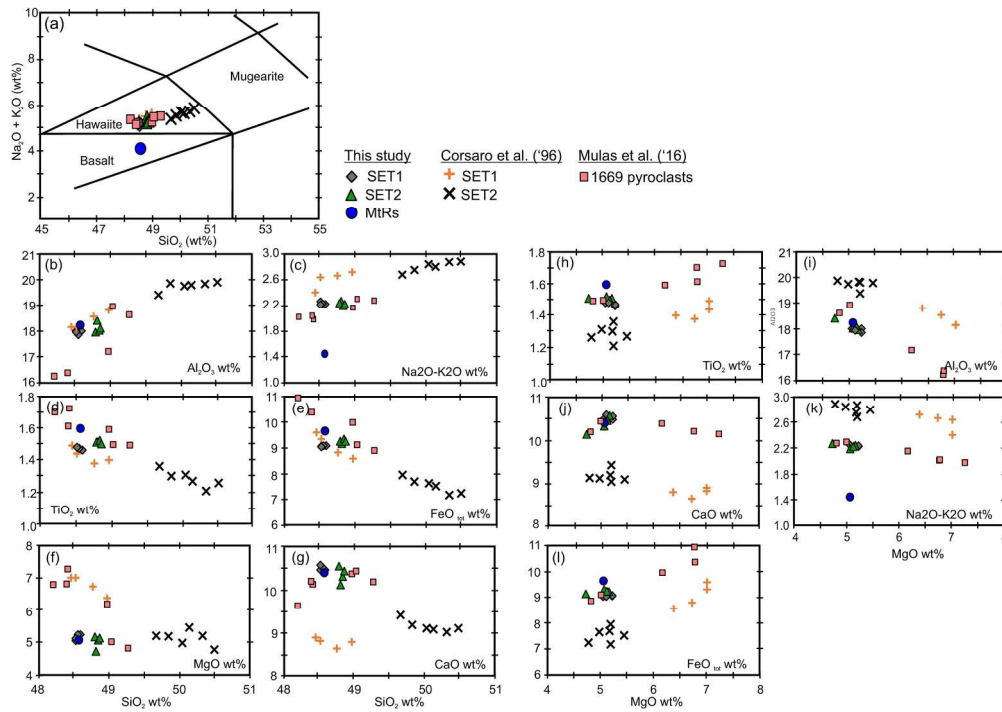


Figure 3

203x142mm (300 x 300 DPI)

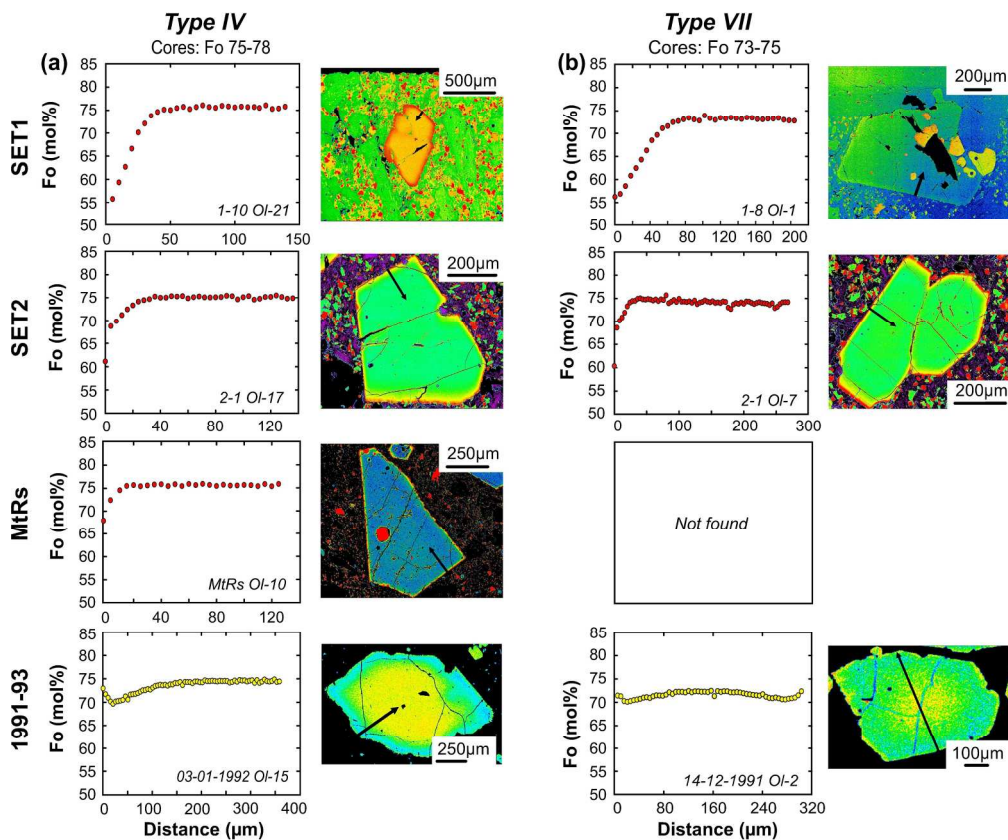


Figure 4

206x170mm (300 x 300 DPI)

view

1
2
3
4
5
6
7
8
9
10
11
12
13
14
15
16
17
18
19
20
21
22
23
24
25
26
27
28
29
30
31
32
33
34
35
36
37
38
39
40
41
42
43
44
45
46
47
48
49
50
51
52
53
54
55
56
57
58
59
60

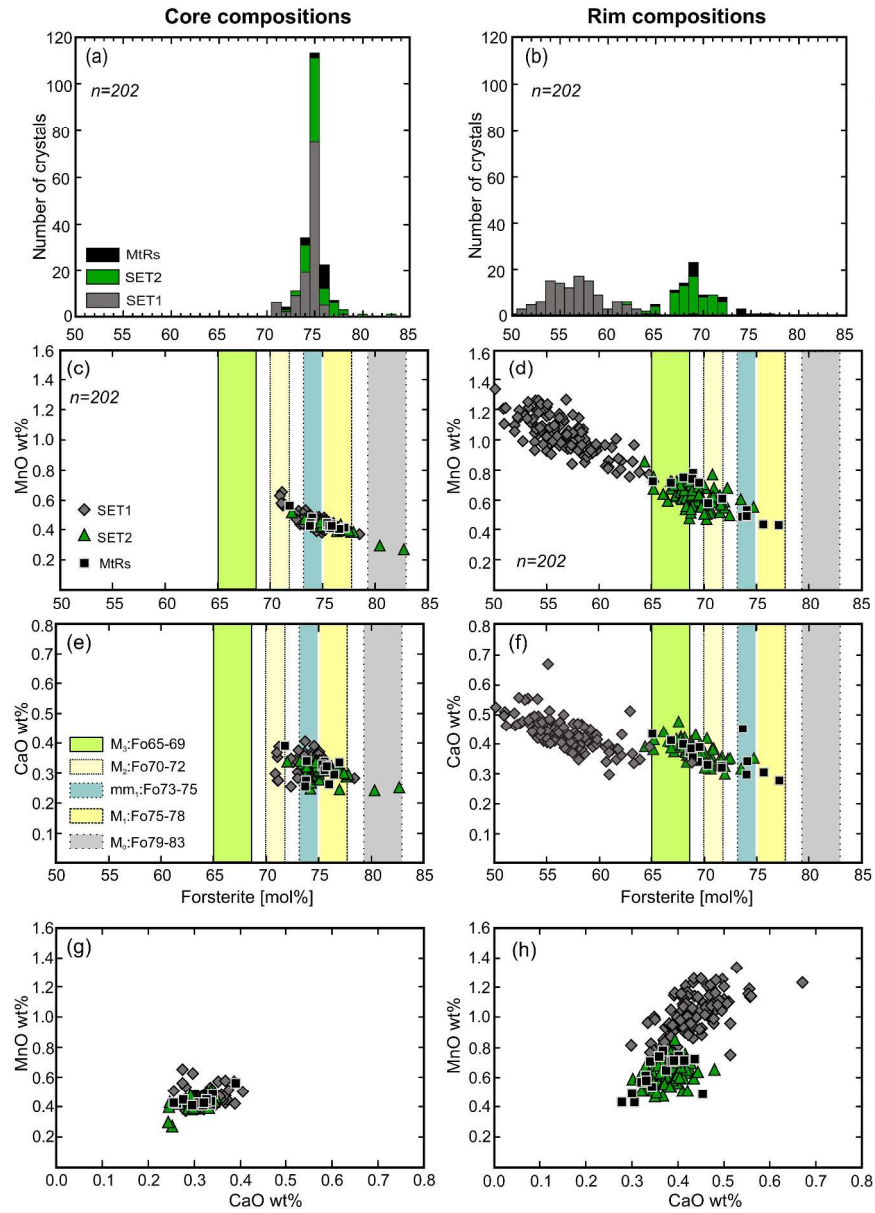


Figure 5

289x403mm (300 x 300 DPI)

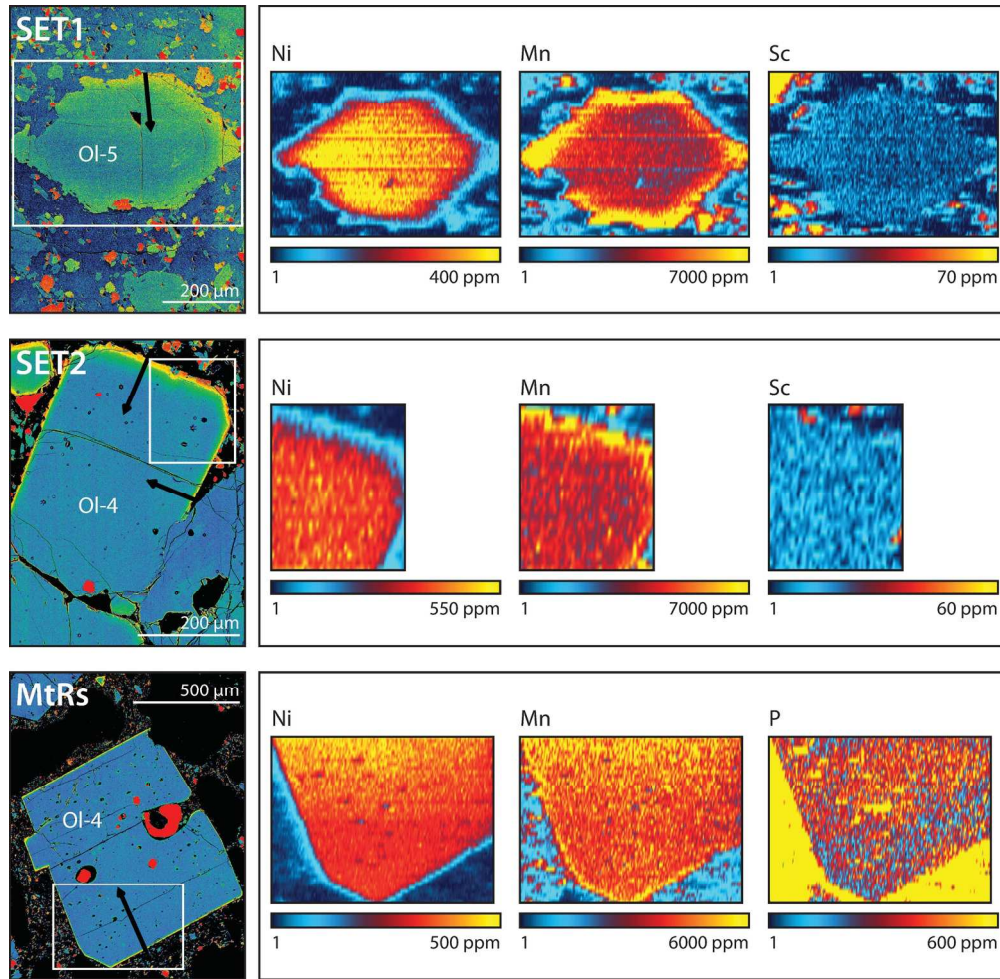


Figure 6

180x176mm (300 x 300 DPI)



1
2
3
4
5
6
7
8
9
10
11
12
13
14
15
16
17
18
19
20
21
22
23
24
25
26
27
28
29
30
31
32
33
34
35
36
37
38
39
40
41
42
43
44
45
46
47
48
49
50
51
52
53
54
55
56
57
58
59
60

(a) 1669 SET 1

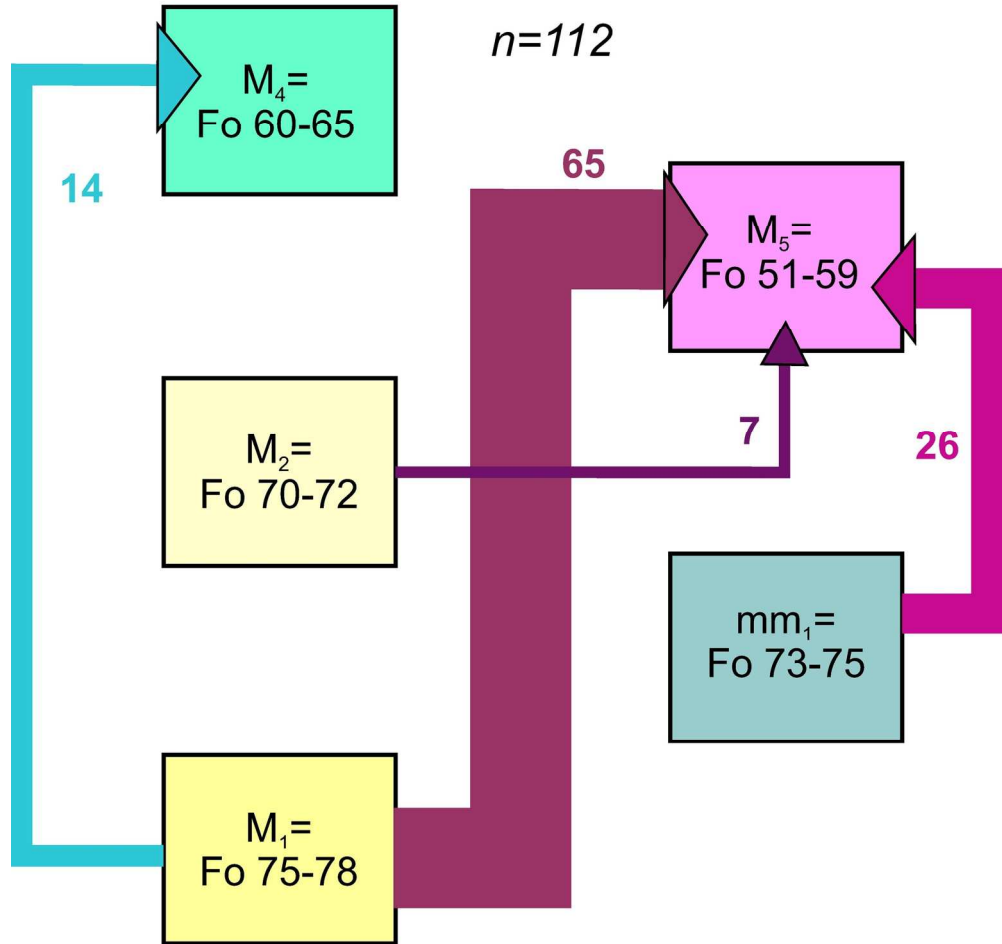


Figure 7a

163x168mm (300 x 300 DPI)

(b) 1669 SET 2

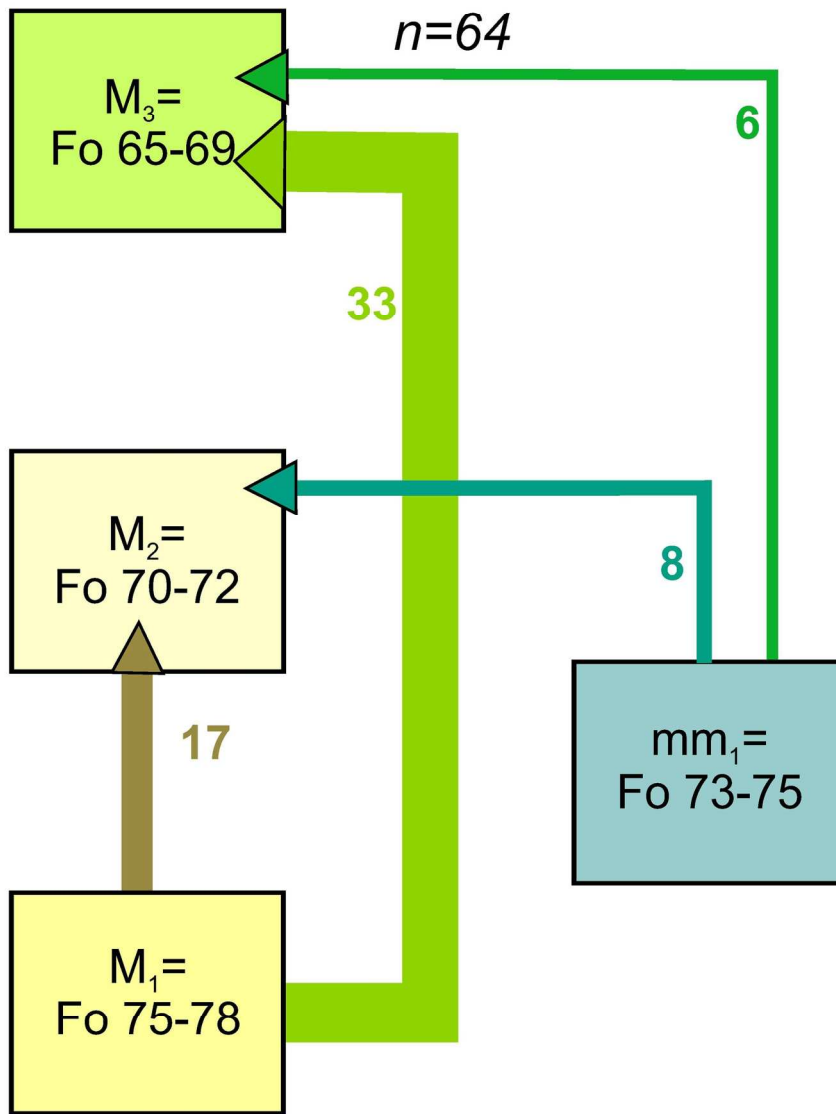


Figure 7b

163x197mm (300 x 300 DPI)

1
2
3
4
5
6
7
8
9
10
11
12
13
14
15
16
17
18
19
20
21
22
23
24
25
26
27
28
29
30
31
32
33
34
35
36
37
38
39
40
41
42
43
44
45
46
47
48
49
50
51
52
53
54
55
56
57
58
59
60

(c) 1669 MtRsSc

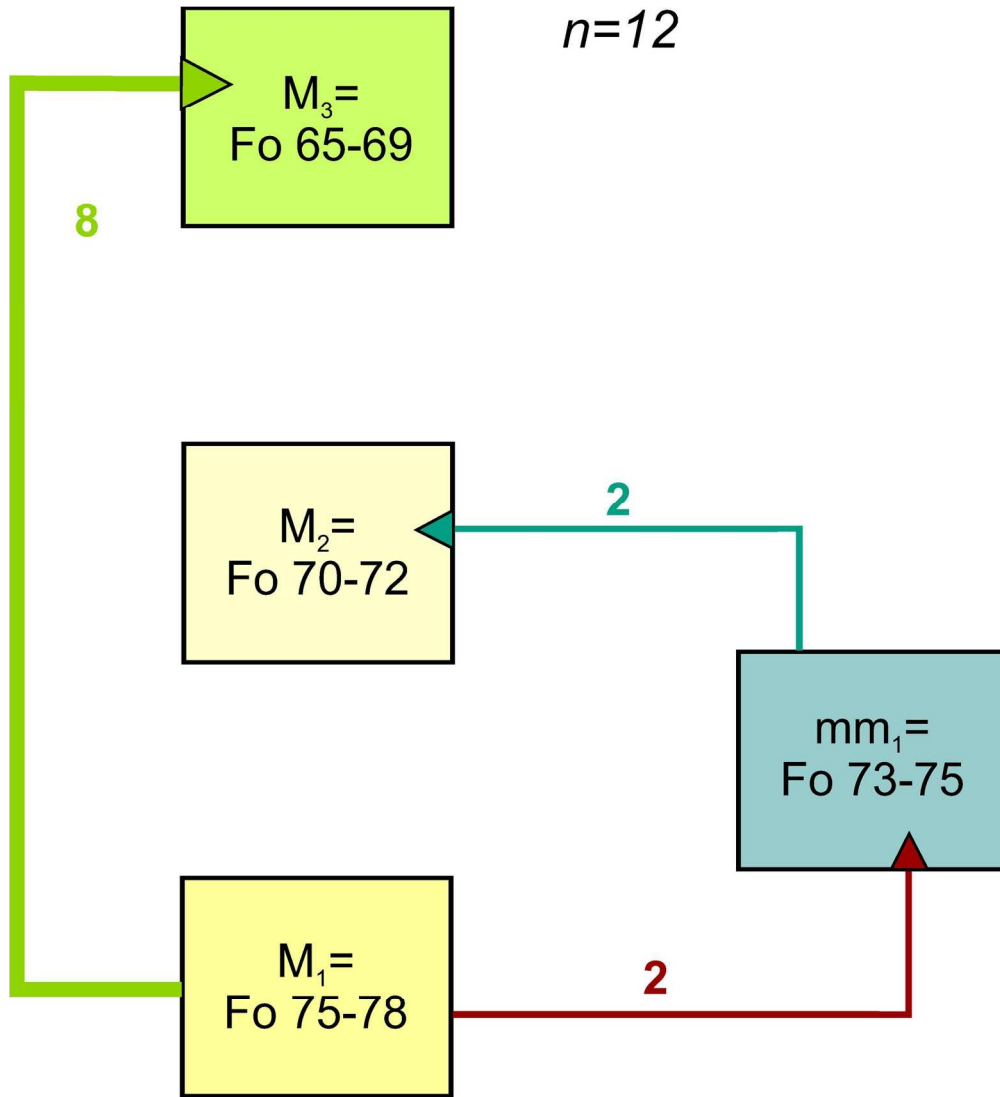


Figure 7c

163x195mm (300 x 300 DPI)

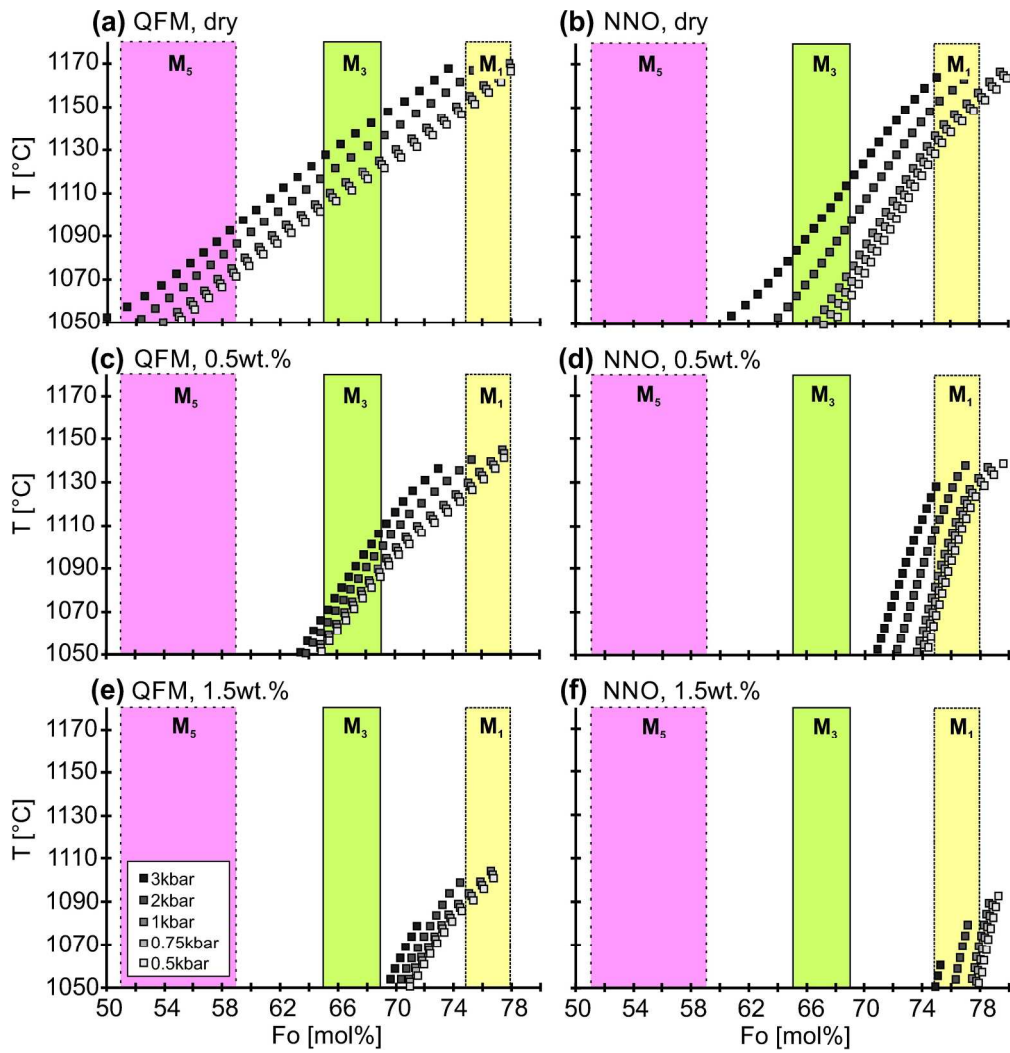


Figure 8

208x216mm (300 x 300 DPI)

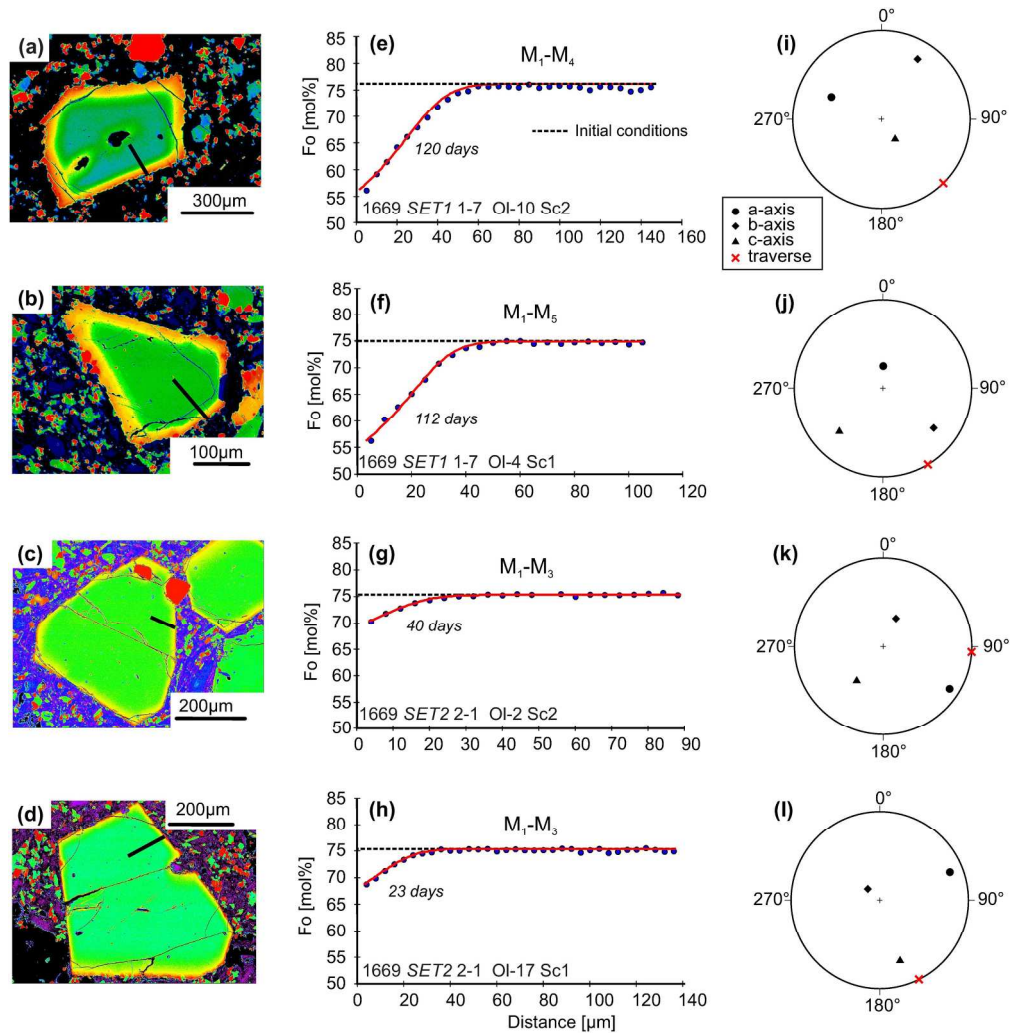


Figure 9

205x210mm (300 x 300 DPI)

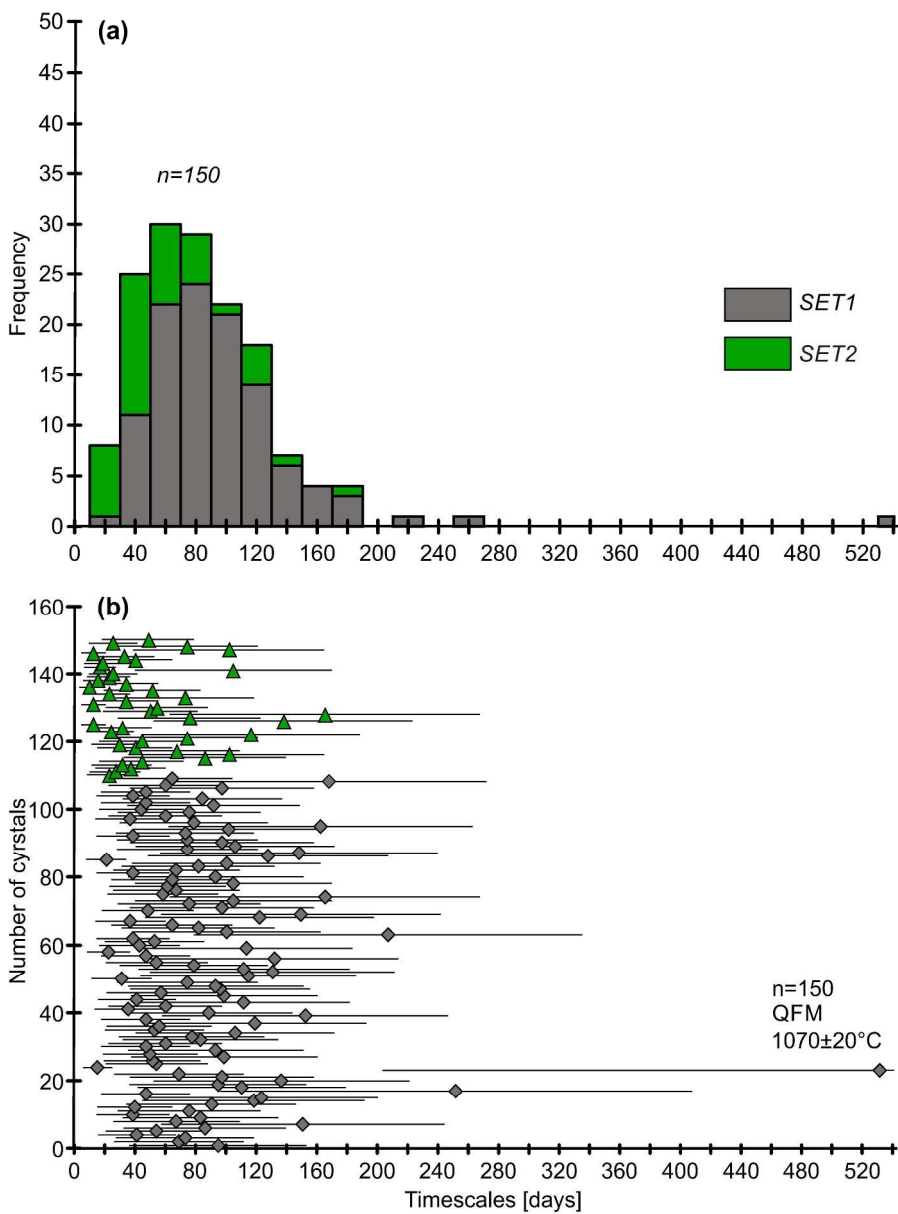


Figure 10

265x356mm (300 x 300 DPI)

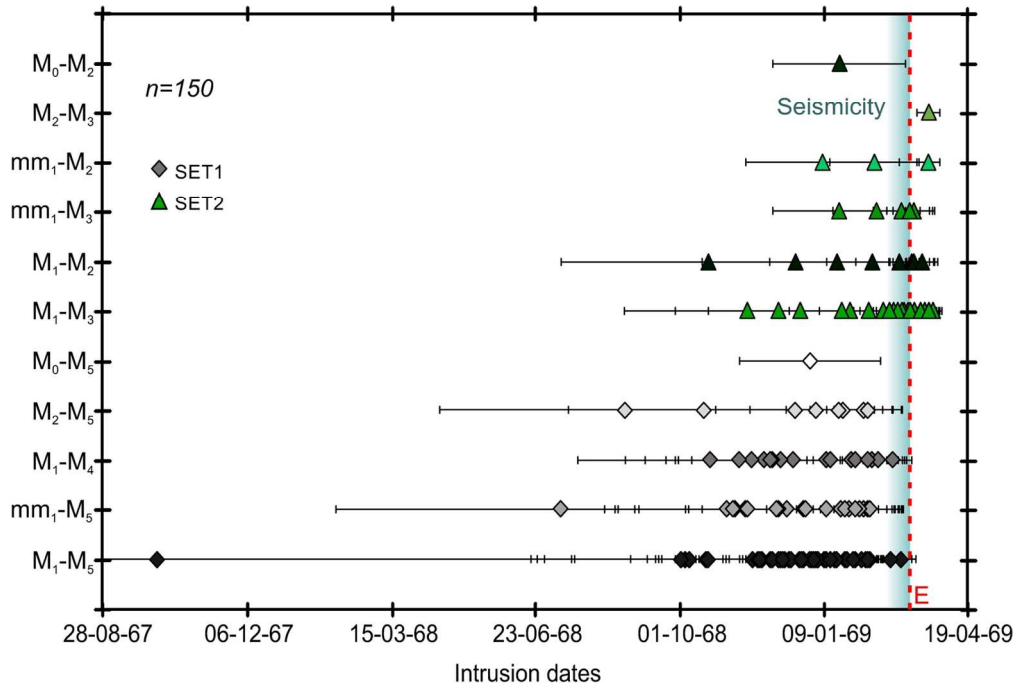


Figure 11

137x93mm (300 x 300 DPI)

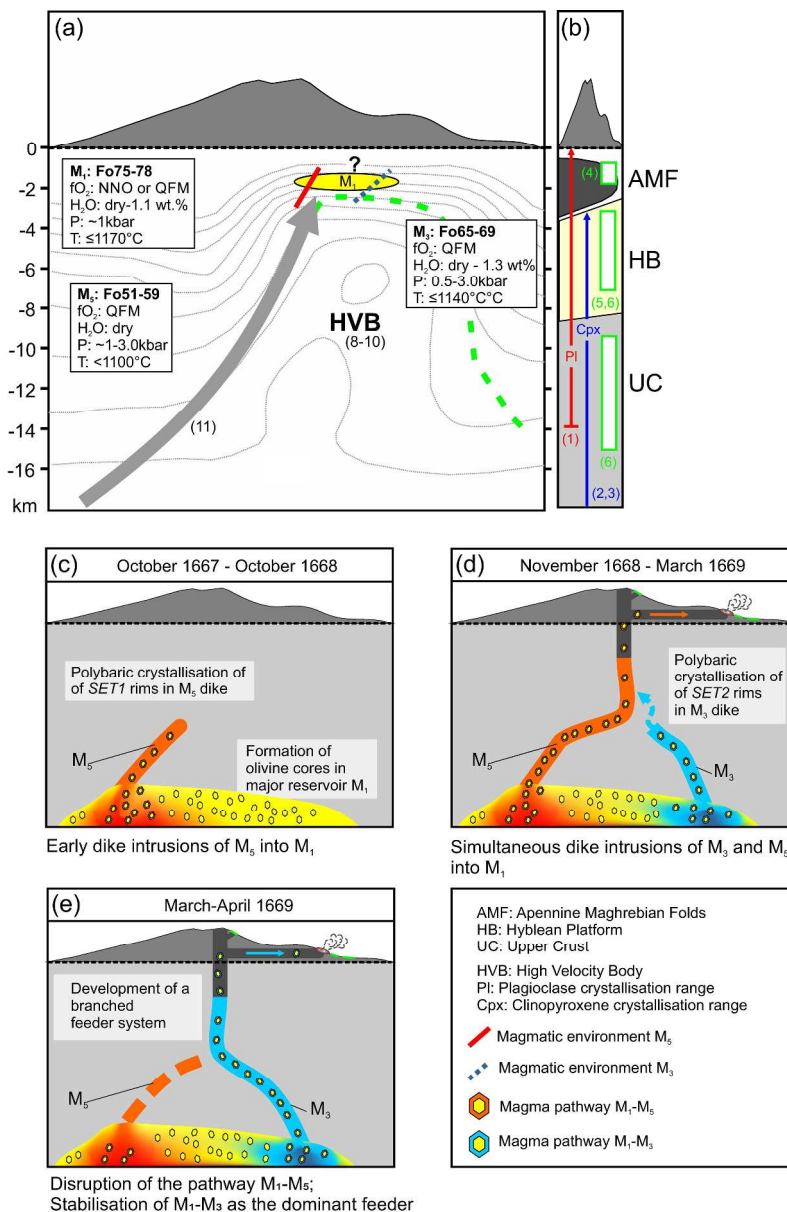


Figure 12

279x423mm (300 x 300 DPI)

Table 1 Summary of 17th century flank activity

Flank eruption	Location and notes	Volume and length	References
1607 (June 28 - ?)	NW flank (2500-1500 m?); fissure above Monte Spagnolo cinder cone	Volume n.d.; lava flow of ~5 km	[1-3]
1610 (1 st phase February 6 – May 3; 2 nd phase May 3 – August 15)	1 st phase: SSW flank (2800-2200 m); Grotta degli Archi craters; 2 nd phase: SW flank (2300-1700 m); Large lava flows near Adrano	Total volume of lava flows: 120×10 ⁶ m ³ (1 st phase 30×10 ⁶ m ³ ; 2 nd phase 90×10 ⁶ m ³); Total volume of pyroclastic material: <4×10 ⁶ m ³ (1 st phase 3×10 ⁶ m ³ ; 2 nd phase <1×10 ⁶ m ³); Total length of lava flow field: 11 km	[1-4]
1614 (July 1) – 1624 (?)	N flank (~2500 m); most of the eruptive fissure is buried under younger lavas, but two larger cones (Due Pizzi) remain visible	Total volume of lava flows: ~1 km ³ ; Total volume of pyroclastic material: 2×10 ⁶ m ³ ; Complex lava flow field up to ~9 km in length	[1-3]
~1630	NW flank from a fissure at 2250 m elevation, emitting "Val di Cannizzola" lava flow Another small lava flow located higher upslope was erupted from a fissure just below Punta Lucia.	n.d.	
1634 (December 18) – 1636 (June)	SE flank (2090-1975 m); short fissure forming a row of hornitos and lava flows causing damages in the area above Zafferana and threatens the village of Fleri	Total volume of lava flows: 180×10 ⁶ m ³ ; Total volume of pyroclastic material: 1×10 ⁶ m ³ ; Length lava flow field: ~9 km, divided into two branches	[4]; [1]; [2]; [3]
1643 (February)	NE flank (2000-1700-1380-1350-1250 m); this is probably one of the smallest flank eruptions of Etna characterized by a NE-SW and NNE-SSW fracture system that produced small lava flows	Total volume of lava flows: ~1×10 ⁶ m ³ ?; Length of lava flows: up to ~5 km	[1-2]
1646 (November 20) – 1647 (January 17)	NNE flank (1950 m); intense Strombolian activity formed the Mt. Nero scoria cone, and lava flows causing damages to cultivated areas	Total volume of lava flows: 160×10 ⁶ m ³ ; total volume of pyroclastic material: 7×10 ⁶ m ³ ; lava flow up to ~7 km long	[1-3]; [5]
1651 (January 17) – 1653 (?)	W flank (2500-2120 m); lava flows partially destroys Bronte and causes damage. The lava flow-field has many areas of ropy pahoehoe, a	Total volume of lava flows (only western flank): 500×10 ⁶ m ³ ; lava flow field	[6]; [2]; [3]

rather rare lava type on Etna. An eruption is also reported to have occurred in 1651 on the eastern flank (Macchia di Giarre) and was covered by the 1689 lava

up to ~14 km long

1669 (March 11 – July 11) S Flank (850-700 m); development of a NNW-SSE-oriented fracture system 14-km-long (from Mt. Frumento Supino, 2800 m to Mompilieri, 600 m). Vigorous Strombolian activity formed the Mts. Rossi scoria cones. Lava effusions divided into three main branches that destroyed La Guardia, Belpasso, Mompilieri, Camporotondo, S. Pietro Clarenza, Massa Annunziata, S. Giovanni Galermo, Misterbianco and the western part of Catania

Total volume of lava flows: $>600 \times 10^6 \text{ m}^3$; total volume of pyroclastic material: from 80 to $250 \times 10^6 \text{ m}^3$; lava flow field up to ~17 km long covering an area of 40 km^2

n.d.: not determined; [1] Recupero (1815); [2] Branca & Del Carlo (2004); [3] Tanguy *et al.* (2007); [4] Carrera (1636); [5] Ferrara (1818); [6] Mancino (1669); [7] Borelli (1670); [8] Branca *et al.* (2015); [9] Mulas *et al.* (2016)

Table 2 Sample locations

	Sample	Latitude (N)	Longitude (E)	Location	Notes
SET1	1-6	37.550439°	14.986601°	Piano Tavola	samples of lava emitted on March 19, 1669
	1-7	37.550313°	14.988188°	Piano Tavola	samples of lava emitted on March 19, 1669
	1-8	37.549912°	14.988487°	Piano Tavola	samples of lava emitted on March 19, 1669
	1-9	37.549524°	14.987525°	Piano Tavola	samples of lava emitted on March 19, 1669
	1-10	37.549245°	14.986397°	Piano Tavola	samples of lava emitted on March 19, 1669
SET2	2-1	37.515367°	15.041863°	Catania San Nullo	samples of lava emitted after March 29 (possibly April 04) 1669
	2-2	37.516550°	15.041239°	Catania San Nullo	samples of lava emitted after March 29 (possibly April 04) 1669
	2-3	37.515609°	15.043251°	Catania San Nullo	samples of lava emitted after March 29 (possibly April 04) 1669
	2-4	37.514929°	15.043315°	Catania San Nullo	samples of lava emitted after March 29 (possibly April 04) 1669
	2-5	37.514670°	15.042788°	Catania San Nullo	samples of lava emitted after March 20 (possibly April 04) 1669
	MtRs	37.61924°	15.01103°	Monte Rossi scoria cone	Monte Rossi scoria cone bomb erupted after March 20 (possibly March 25) 1669

Table 3 Bulk rock compositions of SET1 and SET2 eruption products

Oxide (wt%)	SET1				SET2				MtRs
	1-6	1-7	1-8	1-9	2-1	2-2	2-3	2-4	MtRs
SiO ₂	48.59	48.52	48.55	48.52	48.81	48.79	48.84	48.86	48.57
TiO ₂	1.46	1.48	1.47	1.48	1.51	1.51	1.52	1.50	1.60
Al ₂ O ₃	18.02	18.01	17.87	17.96	18.43	17.98	18.03	18.13	18.25
Fe ₂ O ₃	10.09	10.06	10.07	10.04	10.17	10.27	10.37	10.28	10.72
FeO	9.08	9.05	9.06	9.03	9.15	9.24	9.33	9.25	9.65
CaO	10.47	10.47	10.54	10.58	10.12	10.56	10.32	10.44	10.40
MgO	5.23	5.05	5.23	5.11	4.73	5.17	5.07	5.13	5.06
MnO	0.17	0.17	0.17	0.17	0.17	0.17	0.17	0.17	0.19
K ₂ O	1.45	1.46	1.41	1.47	1.57	1.46	1.52	1.49	1.32
Na ₂ O	3.67	3.72	3.64	3.68	3.84	3.70	3.71	3.71	2.77
P ₂ O ₅	0.50	0.51	0.50	0.51	0.54	0.52	0.53	0.52	0.51
Total	99.59	99.36	99.53	99.42	100.48	99.53	100.34	100.44	100.66
LOI	-0.29	-0.32	-0.15	-0.33	-0.32	0.12	0.03	-0.03	1.27
Rb (ppm)	36	35	30	33	34	33	32	36	27
Ba (ppm)	768	773	701	712	737	782	713	780	764
Th (ppm)	33	33	27	27	28	34	29	34	39
U (ppm)	<20	<20	<20	<20	<20	<20	<20	<20	<20
Nb (ppm)	50	53	47	46	49	53	51	54	59
La (ppm)	75	87	87	66	79	81	80	86	80
Ce (ppm)	135	123	118	132	126	131	133	131	138
Pb (ppm)	30	22	19	17	20	20	21	20	18
Sr (ppm)	1171	1183	1161	1169	1205	1166	1172	1178	1251
Nd (ppm)	44	53	49	47	50	47	47	51	49
Zr (ppm)	211	216	215	215	225	220	223	219	241
Y (ppm)	27	27	25	23	25	28	25	28	31
Ni (ppm)	31	33	32	30	30	31	34	47	34
Cr (ppm)	52	48	57	47	40	47	44	67	43
V (ppm)	253	259	245	227	238	260	252	261	292
Co (ppm)	31	31	28	27	28	32	28	31	34
Cu (ppm)	127	134	94	107	115	120	112	132	140
Zn (ppm)	91	94	84	80	84	99	94	97	110

Notes: LOI: Loss on ignition; Note that the MtRs sample has a high LOI, which is not untypical for scoria.

Table 4 Comprehensive timescale record of *SET1* and *SET2* olivines

Sample	Olivine	Timescale [days]	1 σ	Sequence of reservoirs
1-6	OI-1	95	59	mm1-M5
	OI-3	69	43	M1-M5
	OI-4	73	45	M1-M5
	OI-19	42	26	mm1-M5
	OI-16	55	34	M1-M5
	OI-11	86	53	M1-M5
	OI-13	151	93	M1-M5
	OI-12b	68	42	M1-M4
	OI-14	84	52	mm1-M5
	OI-28	39	24	mm1-M5
	OI-27	76	47	M1-M5
	OI-24	40	25	M1-M5
	OI-30	91	56	M1-M4
	OI-6	119	73	M1-M5
	OI-8	124	76	mm1-M5
	OI-9	48	29	M1-M5
	OI-5	252	156	mm1-M5
	OI-29	111	68	M1-M4
	OI-22	95	59	mm1-M5
	1-7	OI-23	137	84
OI-25		98	60	M1-M5
OI-31		69	43	M1-M5
OI-7		531	328	M1-M5
OI-23		16	10	M1-M5
OI-22		55	34	M1-M5
OI-21		52	32	mm1-M5
OI-20		99	61	M1-M4
OI-19		50	31	M1-M4
OI-18		94	58	M1-M5
OI-16		48	29	M1-M4
OI-17		60	37	M1-M5
OI-15b		84	52	M1-M5
OI-14		78	48	M1-M5
OI-13		107	66	M1-M5
OI-12		53	33	M1-M5
OI-11		56	35	M2-M5
OI-10	120	74	M1-M4	
OI-9a	48	29	M1-M5	
OI-8b	153	94	M2-M5	
OI-8a	89	55	M2-M5	

Table 4 cont.

Sample	Olivine	Timescale [days]	1 σ	Sequence of reservoirs
1-7	OI-7	36	22	M1-M4
	OI-6	60	37	M1-M5
	OI-4	112	69	M1-M5
	OI-3	42	26	M2-M5
	OI-2a	99	61	M1-M5
	OI-1	58	36	mm1-M5
	OI-24	96	60	M1-M5
	OI-25	94	58	M1-M5
	OI-2c	75	46	M1-M5
	OI-2d	32	20	M1-M4
1-8	OI-19	115	71	M1-M5
	OI-18	131	81	mm1-M5
	OI-17	112	69	M1-M5
	OI-16	79	49	M0-M5
	OI-15	55	34	mm1-M5
	OI-14	132	82	mm1-M5
	OI-13	48	29	M1-M5
	OI-11	23	14	M1-M5
	OI-12	114	70	M1-M5
	OI-10	43	27	M1-M5
	OI-9	53	33	M1-M5
	OI-7	39	24	M2-M5
	OI-6	207	128	M2-M5
	OI-5	101	62	M1-M5
	OI-4	82	51	mm1-M5
	OI-3	65	40	M1-M5
	OI-2	37	23	mm1-M5
	OI-1	122	76	mm1-M5
1-9	OI-1	150	92	M1-M5
	OI-22	49	30	M1-M5
	OI-18	98	60	M1-M5
	OI-14	76	47	M1-M5
	OI-21	105	65	M1-M5
	OI-20	166	102	M1-M5
	OI-24	59	36	M2-M5
	OI-19	68	42	mm1-M5
	OI-17	62	38	M1-M5
	OI-8	105	65	M1-M4
	OI-12	65	40	M1-M4
OI-7a	94	58	M1-M5	

Table 4 cont.

Sample	Olivine	Timescale [days]	1 σ	Sequence of reservoirs
1-9 cont.	OI-7b	39	39	M1-M4
	OI-4	68	68	M1-M5
	OI-6	82	82	mm1-M5
	OI-2	101	101	mm1-M5
	OI-10	22	22	M1-M4
	OI-11	128	128	M1-M4
	OI-16	148	148	M1-M4
	OI-5	75	75	M2-M5
	OI-7c	107	107	M1-M4
1-10	OI-21b	98	60	M1-M5
	OI-20a	75	46	M1-M5
	OI-20b	39	24	M1-M5
	OI-18	73	45	M1-M5
	OI-17	102	63	mm1-M5
	OI-15	163	100	M1-M5
	OI-14	79	49	M1-M5
	OI-13	37	23	M1-M5
	OI-11	60	37	M1-M5
	OI-10	76	47	M1-M5
	OI-9a	45	28	mm1-M5
	OI-8	92	57	M1-M5
	OI-6	48	29	mm1-M5
	OI-5a	85	52	M1-M5
	OI-4	39	24	M1-M5
	OI-2	48	29	mm1-M5
	OI-1a	98	60	M1-M5
	OI-1b	60	37	M1-M5
	OI-12	168	104	M1-M5
	OI-22	65	40	M1-M5
2-1	OI-17	23	14	M1-M3
	OI-15	27	17	M1-M3
	OI-8	37	23	M1-M3
	OI-7	32	20	mm1-M3
	OI-6a	45	28	M1-M3
	OI-5	86	53	mm1-M2
	OI-4	102	63	M1-M3
	OI-3	68	42	M1-M3
	OI-2	40	25	M1-M3
OI-1	30	19	M1-M3	

2-2	OI-15	45	28	M1-M3
	OI-12	75	46	mm1-M3
	OI-11	117	72	M1-M3
	OI-10	24	15	M1-M2
	OI-7	32	20	M1-M3
	OI-5	13	8	mm1-M2
	OI-14	138	85	M1-M3
2-3	OI-2a	76	47	M1-M2
	OI-2b	166	102	M1-M2
	OI-3	50	31	mm1-M2
	OI-5	55	34	M1-M3
	OI-6	13	8	M2-M3
2-4	OI-23	35	21	M1-M3
	OI-20	73	45	M1-M3
	OI-19	23	14	M1-M2
	OI-18	52	32	M1-M2
	OI-17	10	6	M1-M3
	OI-14	35	21	M1-M3
	OI-9	16	10	M1-M3
	OI-8	23	14	mm1-M3
	OI-7	26	16	M1-M3
	OI-6b	105	65	M1-M2
	OI-6a	17	11	M1-M2
	OI-4	19	12	M1-M3
	OI-2	40	25	M1-M3
	OI-1	33	20	M1-M2
2-5	OI-3	13	8	M1-M3
	OI-12	102	63	M1-M3
	OI-11	75	46	M0-M2
	OI-7	26	16	mm1-M3
	OI-5	49	30	mm1-M3